[redacted]

SECURITY CLASSIFICATION OF THIS PAGE *(When Data Entered)*

REPORT DOCUMENTATION PAGE		READ INSTRUCTIONS BEFORE COMPLETING FORM
1. REPORT NUMBER AFFDL-TR-73-112	2. GOVT ACCESSION NO.	3. RECIPIENT'S CATALOG NUMBER
4. TITLE *(and Subtitle)* Fighter Technology Demonstrator Precursor Analysis and Test-Volume II, An Experimental Investigation of the Aerodynamic Characteristics of a Fighter Technology Demonstrator Jet Flap Development Model at Low Subsonic Mach Numbers		5. TYPE OF REPORT & PERIOD COVERED Final 5/73 - 10/73 6. PERFORMING ORG. REPORT NUMBER
7. AUTHOR(s) G. N. Panageas		8. CONTRACT OR GRANT NUMBER(s) F33615-73-C-3135
9. PERFORMING ORGANIZATION NAME AND ADDRESS Rockwell International Corp, L.A. Aircraft Div Los Angeles International Airport Los Angeles, California 90009		10. PROGRAM ELEMENT, PROJECT, TASK AREA & WORK UNIT NUMBERS Project 1207
11. CONTROLLING OFFICE NAME AND ADDRESS Air Force Flight Dynamics Laboratory Air Force Systems Command Wright-Patterson Air Force Base, Ohio		12. REPORT DATE November 1973 13. NUMBER OF PAGES 109
14. MONITORING AGENCY NAME & ADDRESS *(if different from Controlling Office)*		15. SECURITY CLASS. *(of this report)* Unclassified 15a. DECLASSIFICATION/DOWNGRADING SCHEDULE

16. DISTRIBUTION STATEMENT *(of this Report)*

Approved for public release; distributed unlimited.

17. DISTRIBUTION STATEMENT *(of the abstract entered in Block 20, if different from Report)*

18. SUPPLEMENTARY NOTES

None

19. KEY WORDS *(Continue on reverse side if necessary and identify by block number)*

Jet flap, direct lift/direct ride force, close coupled canard, canard, vectored thrust, flow surveys, downwash, longitudinal stability, directional stability

20. ABSTRACT *(Continue on reverse side if necessary and identify by block number)*

A subsonic wind tunnel test of a small-scale fighter technology demonstrator development model was conducted to obtain data instructive in refining and developing the configuration. Tests were performed at mach 0.23 through high angles of attack and at angles of sideslip for various geometric alterations to the configuration to evaluate their impact on the design aerodynamics. Flow surveys were conducted to evaluate flow fields at potential inlet locations

DD FORM 1 JAN 73 1473 EDITION OF 1 NOV 65 IS OBSOLETE

SECURITY CLASSIFICATION OF THIS PAGE *(When Data Entered)*

20. ABSTRACT (CONTINUED)

Additional tests were conducted, with a secondary air source providing thrust, for a jet flap arrangement at the wing trailing edge. This jet flap configuration incorporates the features of an aerodynamic flap and jet flap in that the turning action of the conventional mechanical flap also directs the jet efflux. Deflection angles of the jet were 0, 10, 20, and 30 degrees for two flap spans.

The results indicate that the effectiveness of the canard was sensitive in level to various planform and relative geometric separations from the wing, but in its low forward location continued to show an unfavorable angle-of-attack variation. Lift slope for this configuration demonstrates a continuation through 28 degrees pitch without stall. However, the longitudinal stability indicates some nonlinearity through this pitch range. Directional stability indicates a positive level through 28 degrees alpha primarily due to the canard input which becomes increasingly stabilizing above 10 degrees. Placement of the canard in a high closely coupled arrangement produced a decrease in canard effectiveness, but a much more desirable angle-of-attack variation.

Direct and induced thrust results indicate an increase in lift and a negative shift in moment, increasing with deflection, for the two flap spans tested. The increased in geometric jet flap span produced an increased in induced thrust effects slightly below the estimated values over the angle-of-attack range.

Flow surveys indicated the wake of the canard passes under the wing for this configuration causing high gradients through the maximum angle tested of 15 degrees. However, downwash and velocity ratios indicate relatively moderate increments above the wing plane due to canard input and deflection leading to the conclusion that a high inlet position above the wing is much more feasible than below the wing.

FOREWORD

This report describes the subsonic wind tunnel investigation to refine and develop the Rockwell fighter technology demonstrator. This effort was performed by the Los Angeles Aircraft Division (LAAD), of Rockwell Internation Corporation under Air Force contract F33615-73-C-1335, project 1207, at Los Angeles, California. The contract, entitled "Fighter Technology Demonstrator Precursor Analysis," was under the direction of the Air Force Flight Dynamics Laboratory, Wright-Patterson AFB, with Major D. Seger (AFFDL/PTC) as contract monitor. Program Manager for Rockwell International was A. Ley.

Volume II covers the work undertaken in task III of the noted contract and performed during the period 1 May 1973 to 10 August 1973. This volume was submitted by the authors on 17 August 1973.

The author acknowledges the contributions made by the following members of Rockwell International: Mr. M. Cohen, Mr. J. Benson, and Mr. W. Garrett of the Wind Tunnel Test Group and Mr. A. Sharon, and Mr. P. Divan III of the Aerodynamics Group for their efforts in conducting the wind tunnel test and analyzing the data results. Report No. NA-73-588 has been assigned for internal control.

This technical report has been reviewed and is approved.

TABLE OF CONTENTS

LIST OF ILLUSTRATIONS

SECTION I

INTRODUCTION

Maneuvering aircraft performance places increased emphasis on providing minimum induced drag through controlled flow at high load factors. To this end, several emerging aerodynamic design technologies are being investigated. Among those receiving attention from designers are multiple surfaces for the control configuration vehicle, blended wing body, variable camber wing design, and jet flap. The jet flap device incorporates separation control with effective increased camber to increase lift and thereby permit a vehicle to operate at reduced pitch angles where drag producing flow separation is minimized. One method of producing the desired combination of wing variable trailing edge camber and jet flap was suggested by Reference 1, and many others are documented in Reference 2.

The objective of this test program was to provide design guidance in developing and refining the fighter technology demonstrator (FTD) baseline configuration. Several areas lend themselves to experimental aerodynamics in the low-speed regime where significant trends can be observed. Primary among these is the interaction of lifting surfaces, their associated downwash characteristics, and flow separation phenomena as incidence angle is varied. In addition, experimental results provide confidence in analytical procedures for basepoint aerodynamic description.

The 0.07075-scale development model, reflecting FTD aerodynamic design features, was tested in the LAAD low-speed wind tunnel on a sting mount with an internal six-component balance. The low-speed facility (NAAL) is a closed-circuit continuous flow ($M = 0 \rightarrow .3$) atmospheric wind tunnel. Being a development model and including jet flaps, the inlets are faired over and the wing-body blending is not incorporated. Fore-and-aft control surfaces are removable and deflectable.

The test program was structured to obtain design data on inlet-wing-canard location, canard planform and location effectiveness, and effects of wing modifications. The trailing edge jet flap utilized a nitrogen gas supply to provide the desired thrust effects, and the span of these flaps was varied at constant exit area.

Tabulated data from this test can be found in Reference 3, and plotted data can be found in Reference 4. Previous test results of this model can be found in References 5 and 6.

SECTION II

MODEL DESCRIPTION

A 0.07075-scale development model of a Rockwell International jet flap fighter technology demonstrator (FTD) was used for this test. (See Figure 1.) The FTD major features are (1) inboard flaps, which have the engine exhaust nozzles as their trailing edges; (2) forward tails (canards); and (3) butterfly, aft tails. The various configuration changes implemented are shown in Figures 1 through 3. The model has provisions for deflecting control surfaces to preselected deflections and removing components. The various control surface and reference geometries are summarized in Table 1. Seven canards, two flaps (hereinafter called jet flaps), and one horizontal tail arrangement at 45 degrees dihedral were tested. Model installation photographs are shown in Figure 5.

Secondary air was brought to the model from an exterior nitrogen supply. A bellows arrangement was used to transfer the nitrogen from the model sting to the model, allowing the jet flap to be metric for this test arrangement. Articulation of the flap is directly associated with the deflection of the secondary air, and the zero reference for flap articulation was the centerline of the flap system. The effects of flap span to wing semispan were studied using two flaps, F_1 and F_3, respectively. The flap span ratio investigated is shown in Table 1.

The basic canard planform for this test (C_5) was placed in various positions on the forebody to test the effectiveness of different canard-to-wing locations, generating canard nonemclature C_5 through C_{10} (Figure 2). A canard of the same planform, but with 33.8 percent less exposed surface area, canard C_6 was used to study surface area variations on canard effectiveness. In addition, canard C_1 of a different planform was tested as a departure point for previous test results. Geometric features of the various canards are summarized in Table 1 and Figure 3.

The wing (W) was tested at two water plane locations (Figure 3, configuration d) and with a reduced wing hood (W_2) in the fuselage reference plane (FRP) location (Figure 2). Rolling the model and sting in the tunnel mount 180 degrees, when the wing was in the high location, represented a low wing variation of wing (W_6) called (W_7). The effects of low wing, high canard were studies with W_7 (Figure 3, configuration f).

To eliminate unporting of the canards and the fuselage at canard deflections and to analyze these effects, the nose of the model was made elliptical in shape (Figure 4), allowing canard deflections through 15 degrees without leading and trailing edge discontinuities.

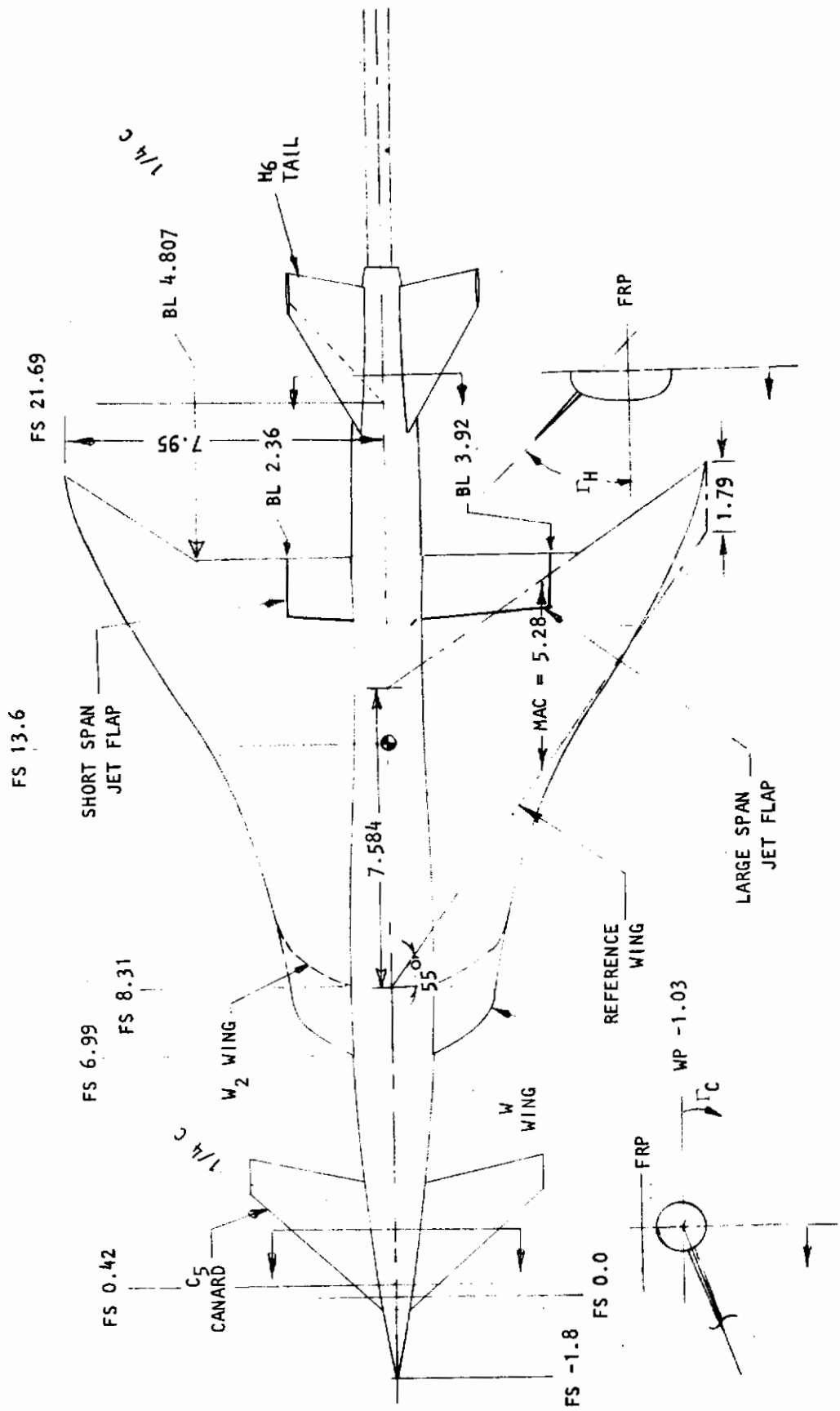

Figure 1. Model planform.

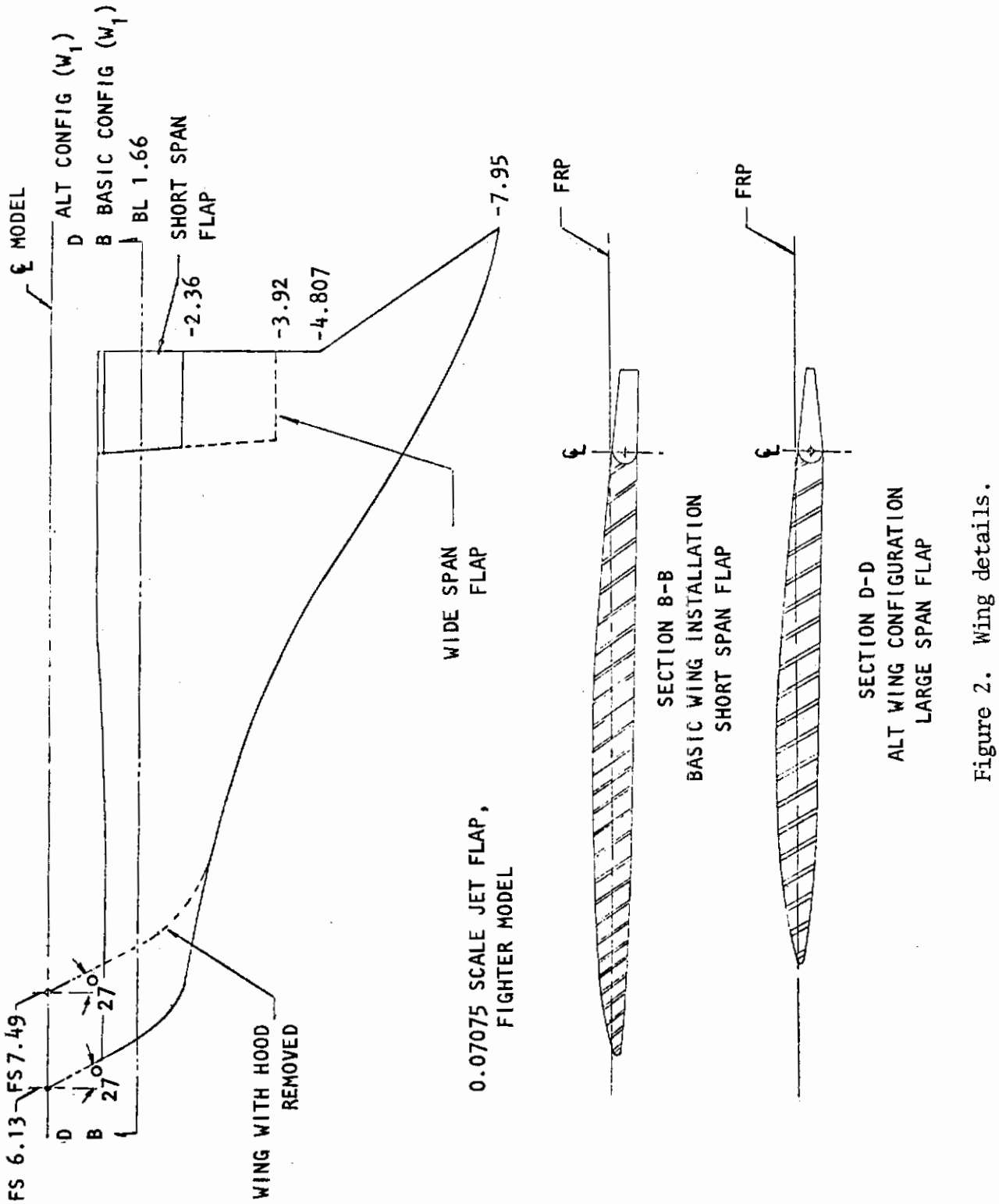

Figure 2. Wing details.

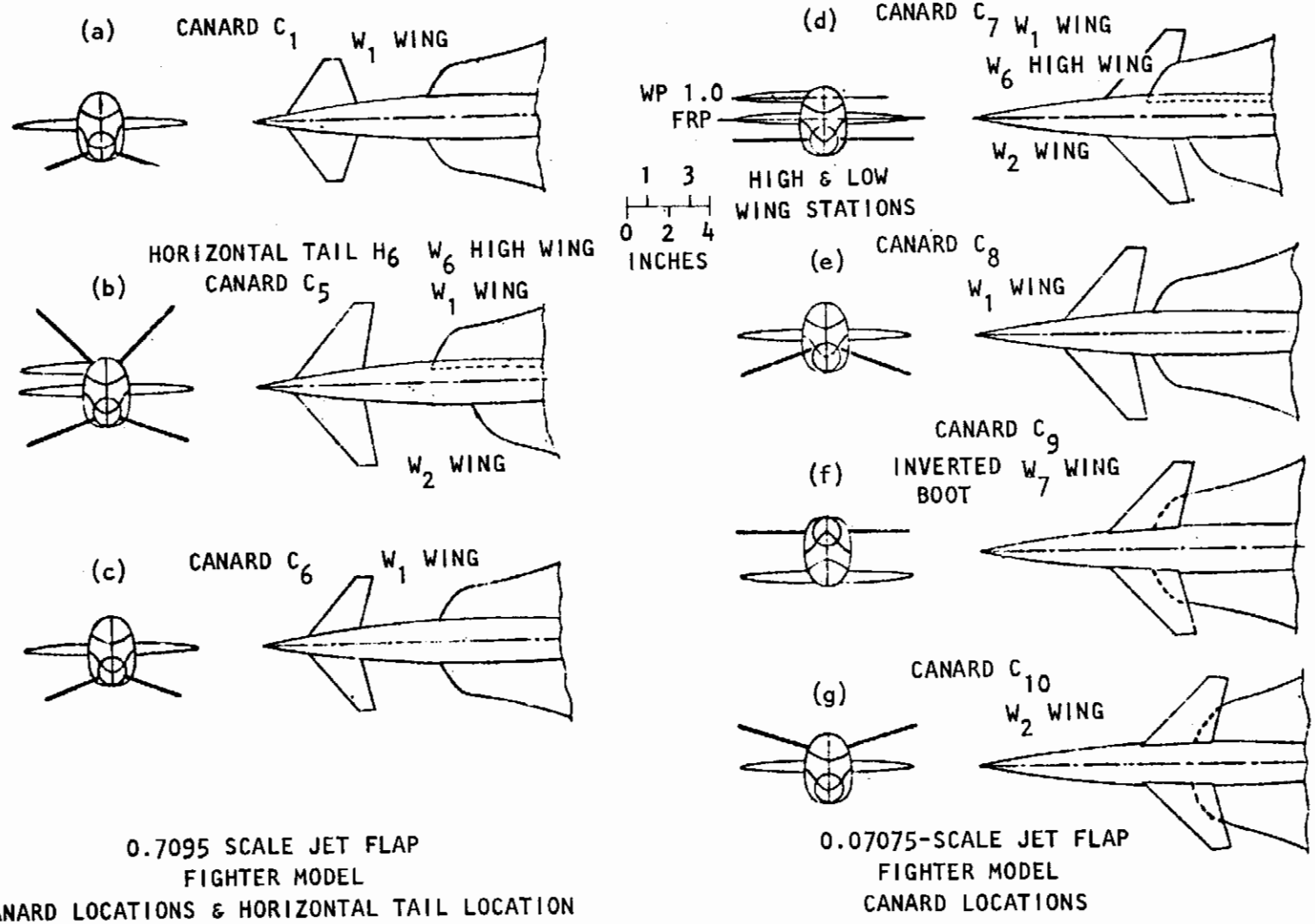

Figure 3. Canard locations and horizontal tail location.

TABLE 1. MODEL GEOMETRY

W_1, W_2, W_6 Wing*	Jet Flap			H_6 Aft Tails (True)	
	Parameters	F_1	F_3		
S_{REF} = 72 in.^{2} (0.5 ft^2)	S, in.^{2}/side	2.21	4.95	S_{exp}	17.528 in.^{2}
b = 15.90 in.	b_j, in.	1.34	3.00	$b/2_{exp}$	3.62 in.^{2}
AR = 3.5	c, in.	1.65	1.65	AR_{exp}	2.99
λ = 0.236	Exit area, in.^{2}/side	0.2625	0.2266	λ_{exp}	0.200
MAC = 5.28	$b_j/(bw/2)_{exp}$	0.193	0.432	Λ_{LE}	45 deg
Λ_{LE} = 55 deg	$b_j/(bw/2)$	0.1688	0.378	Γ	45 deg
B_1, B_2, B_3 fuselage				ℓt	9.59 in.
L = 27.7 in.				V_{Hexp}	0.3126
*Reference Wing Values Based on Trapezoidal Area (Figure 1).				V_{Vexp}	0.1032

Forward Tail (Canard) (True)							
Parameters	C_1	C_5	C_6	C_7	C_8	C_9	C_{10}
S_{exp}, in.^{2}	7.998	13.191	8.728	13.191	13.191	13.191	13.191
$(b/2)_{exp}$	2.03	3.397	2.763	3.397	3.397	3.397	3.397
AR_{exp}	2.061	3.49	3.49	3.49	3.49	3.49	3.49
λ_{exp}	0.239	0.30	0.30	0.30	0.30	0.30	0.30
Λ_{LE} deg	35	40	40	40	40	40	40
Γ deg	-20	-20	-20	0	-20	0	+17
ℓc in.	11.675	11.675	11.675	7.425	9.255	7.425	5.925
V_{Hexp}	0.2308	0.3780	0.25188	0.2576	0.3018	0.2576	0.1966
V_{Vexp}	0.02789	0.04569	0.03044	0.0000	0.03647	0.0000	0.01996

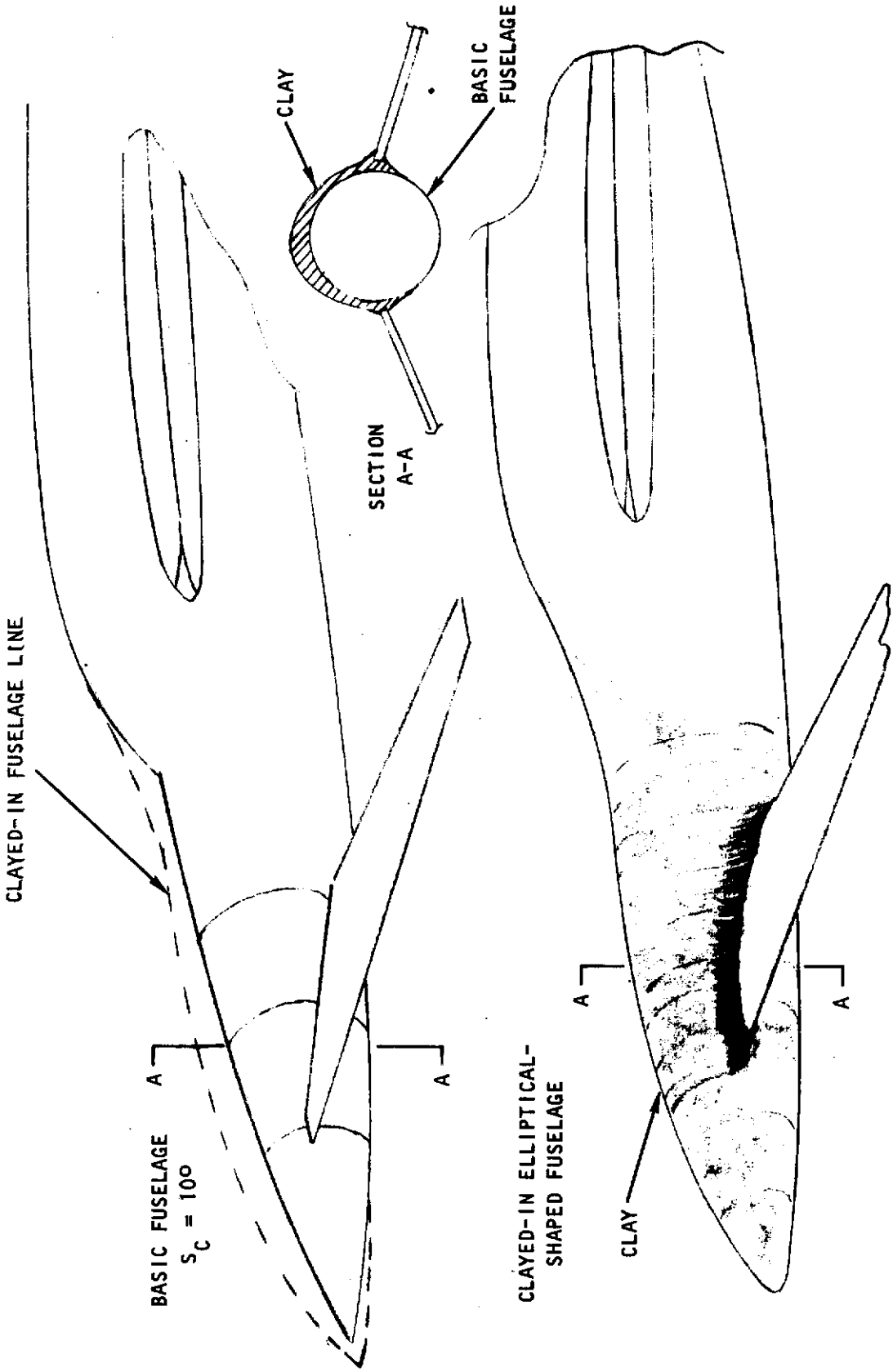

Figure 4. Fuselage change to prevent porting of canard.

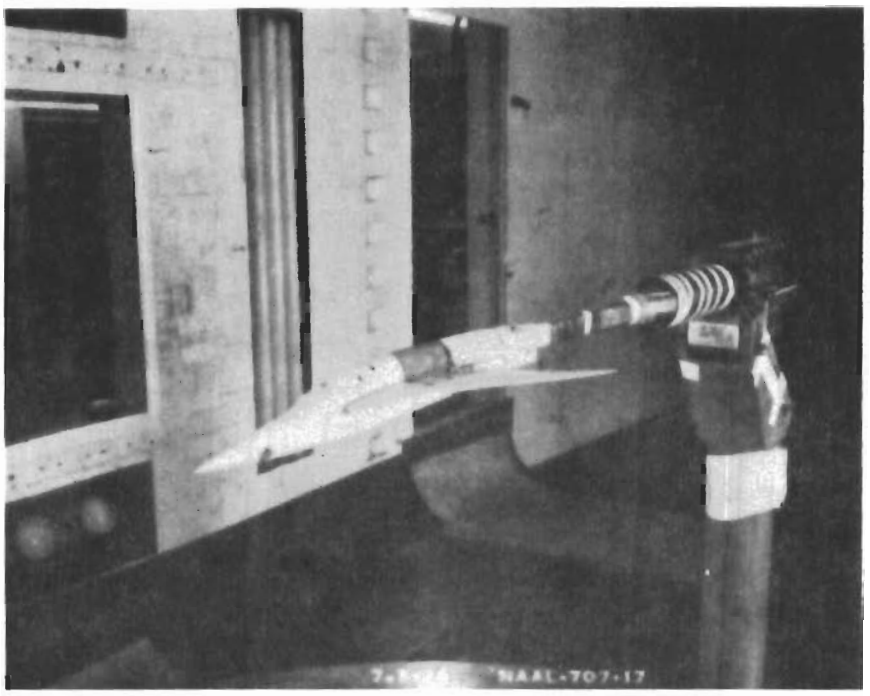

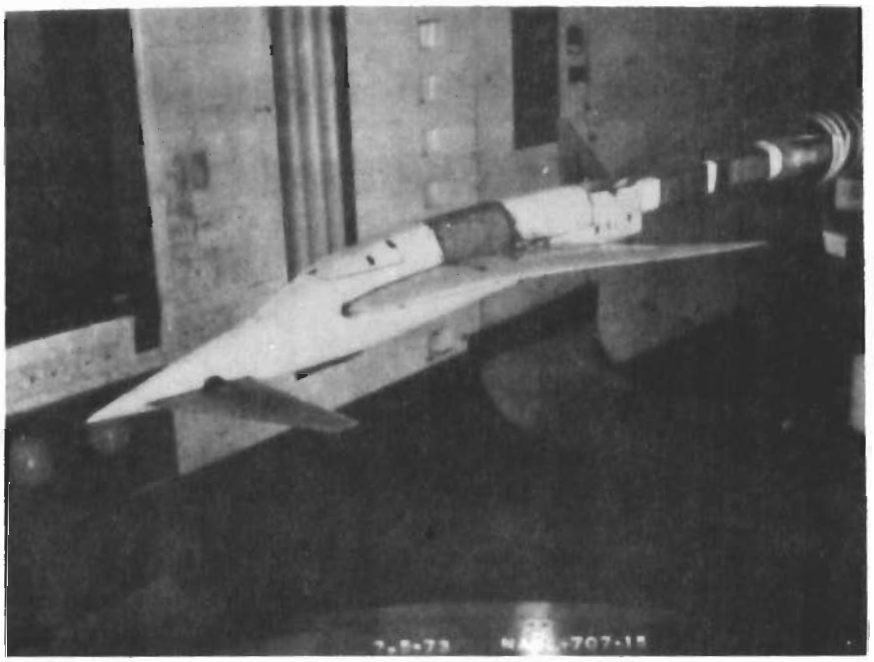

Figure 5. Model installation photographs.

To measure the flow angles and velocity profiles about the wing leading edge, total and static pressure probes and goniometers were placed in vertical proximity to the wing in four chosen positions. Two fuselage stations were tested (FS 4.89 and 5.89) at each of two buttock plane locations (BP 1.55 and 2.30). (See Figure 6.) Vertical stations are also shown in this figure. Eleven total probes and goniometers were stationed and five static probes located in alternate vertical stations as shown. Each set of probes was tested separately at several angles of attack. Model installation photographs are shown in Figure 7.

The model does not reflect the blended wing-body arrangement of FTD designs, and it incorporates a faired-over inlet arrangement. This base-point configuration for model design had the inlet capture area at the wing root leading edge.

Model exit areas for secondary air were designed with a constant exit area as the jet flap span increased. Measurements of the model indicate the hardware was not constructed to the design specification. Exit areas measured are 0.003646 square foot for F and 0.0031471 square foot for the larger span, F_3.

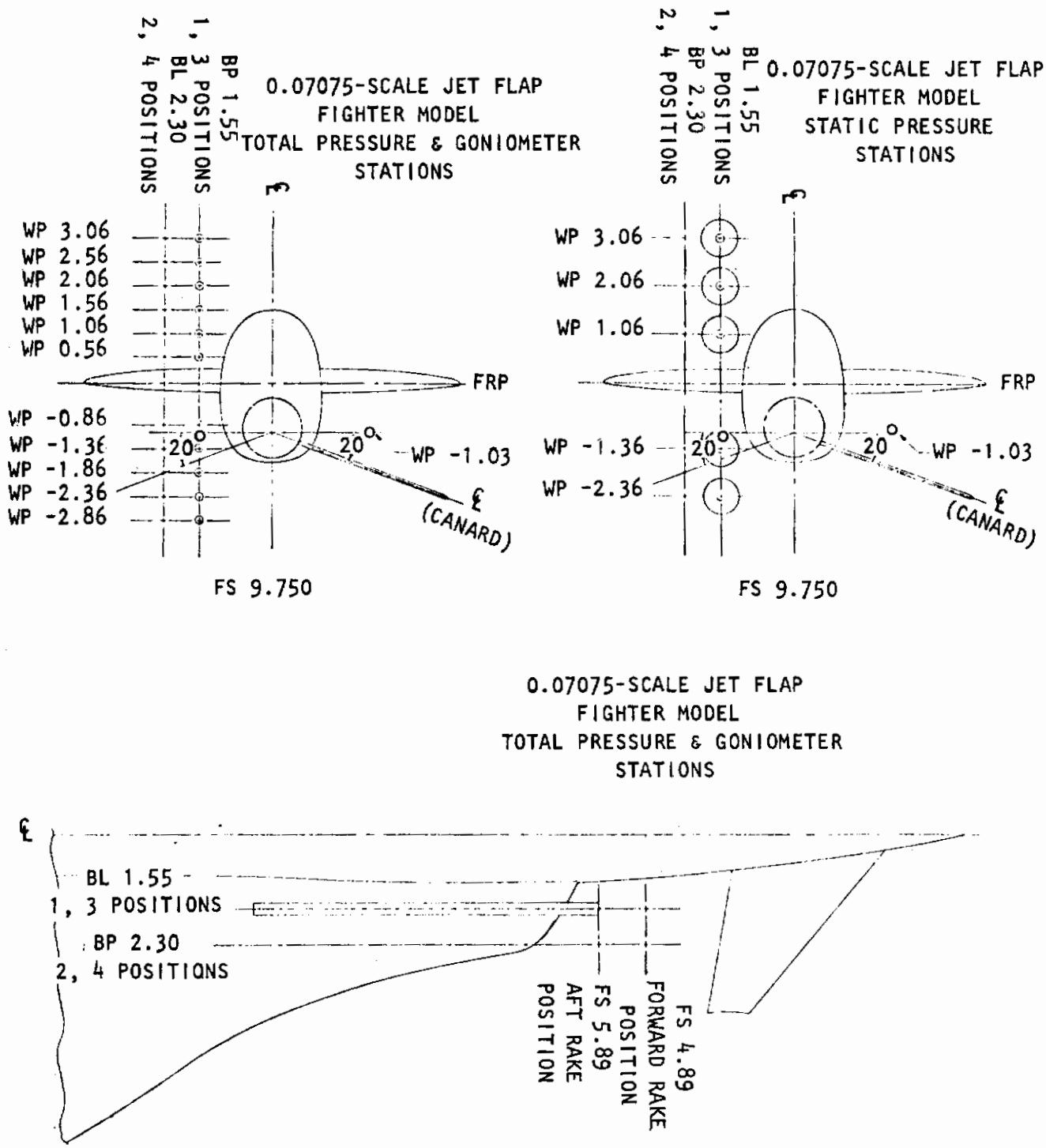

Figure 6. Flow survey instrumentation locations.

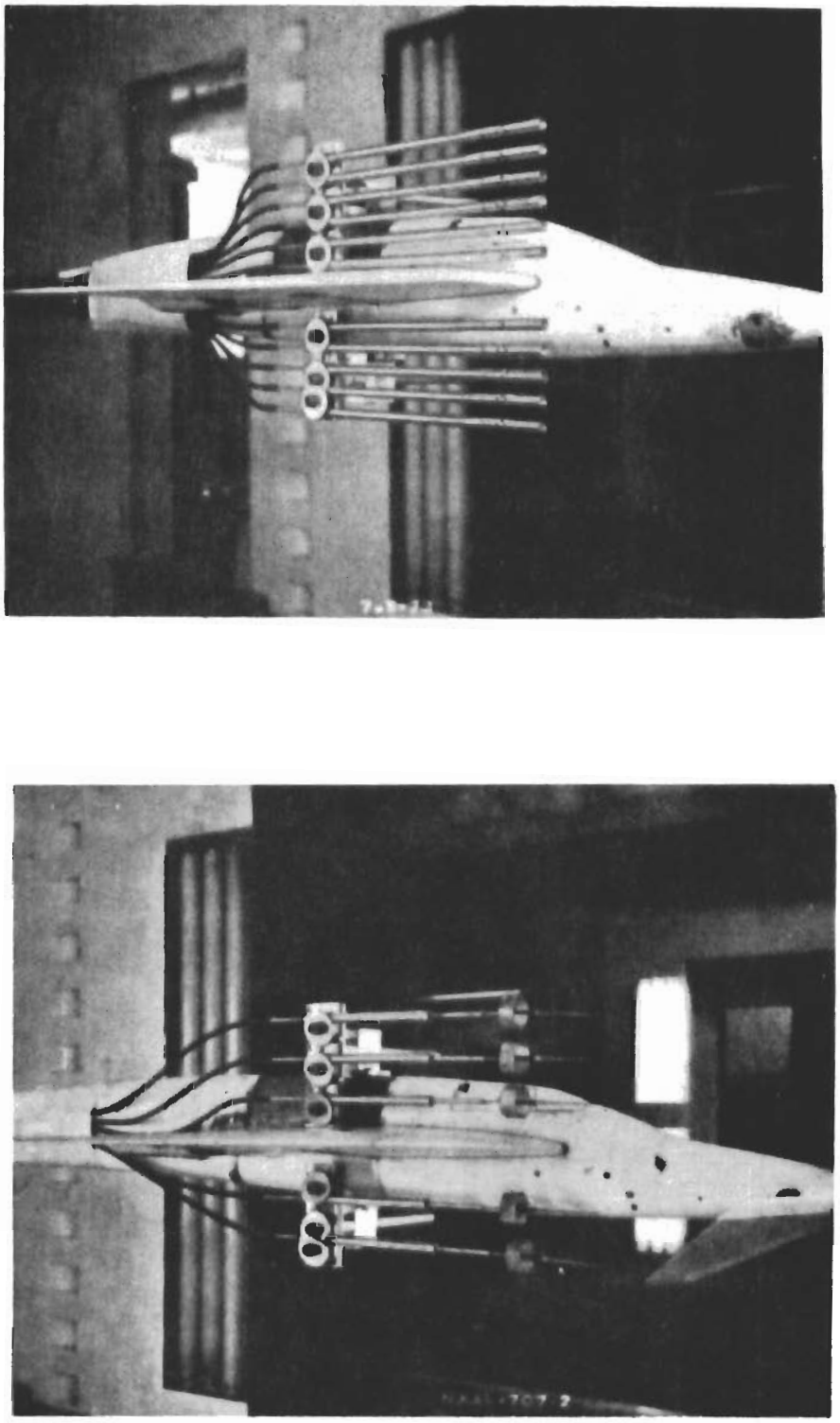

Figure 7. Model installation photographs - flow survey instrumentation.

SECTION III

TEST PROCEDURES

TEST CONDITIONS

Test conditions for the sting-mounted, 0.07075-scale model of the jet flap aero demonstrator development model in the Rockwell International NAAL atmospheric wind tunnel are M = 0.23 and Reynolds number per foot of 1.59 x 10^{-6}. Secondary air, from a nitrogen supply, was the source of thrust for the jet flap phase of this test. The model secondary airflow was set in the tunnel as a function of the static pressure downstream of the drop plates. These static pressures were calibrated versus exit total pressure and weight, such that gross thrust coefficient was calculated based on exit total pressure. Actual data reduction techniques are found in Reference 7, with selected equations found in the list of symbols.

TEST PROCEDURES AND DATA CORRECTIONS

Basic force measurements on the sting-mounted model were made by an internal, six-component strain gage type balance. Standard wind tunnel data reduction techniques, noted in Reference 7, converted the balance outputs to coefficient form in both the body axis and stability axis systems. The axil force measured was corrected for the effect of pressure inside the sting cavity, and model angle of attack was corrected for sting and balance deflection under load. Additional corrections to force measurements which were applied during blowing flap portion of this test are discussed later.

FLOW SURVEY TESTS

Flow survey rakes were mounted on the model in the locations shown in Figure 6. Three types of probes were used interchangeably in the basic rake mounting: shielded total pressure probes, self-alining static pressure probes, and goniometer or flow angularity probes. The static pressure probes were equipped with swivelling tips which were kept alined with the flow direction by attached vanes. The goniometer probes each contained four pressure tubes with their tips cut off at a 45-degree angle, so that a pyramid was formed, oriented with one pair of faces in the pitch plane, and one pair in the yaw plane. The total and static pressure measurements, with free-stream total temperature, were used to calculate local velocity and dynamic pressure, q. The goniometer probes each had an individual calibration of vertical flow angle and horizontal flow angle versus pressure differential in each plane.

Jet exhaust flow from the flaps was simulated by high-pressure nitrogen gas. Since all flap forces were to be measured by the internal balance, it was necessary to bridge the boundary between the nonmetric sting and the metric portion of the model with the nitrogen supply line. A bellows was, therefore, incorporated in the line to permit relative movement between the nonmetric and metric regions, so that the balance was free to measure forces on the metric region only. A series of special calibrations was required to determine corrections to apply to the force data to remove the effects of the gas supply system from the measured forces. These effects included:

1. The bellows adding some stiffness to the balance, decreasing its effective sensitivity

2. Gas pressure inside the bellows increasing its stiffness

3. Gas pressure expanding the bellows, thus exerting a direct force on the balance

4. A force exerted on the balance as a result of the momentum of the in-flowing gas

An additional calibration, not related to the force corrections, was necessary before testing. A total pressure rake was installed at the flap exit nozzle and gas discharged through the system at various flow rates. The primary purposes for this calibration were to determine the exit total pressure ratio in terms of static pressures measured inside the jet flaps.

During the course of the test, it was noted that the discharge coefficient of the jet flaps was being calculated at a questionably high value, resulting in a calculation of thrust that was proportionally high due to the A* term in the gross thrust expression. By the time the cause of this error was found, the test had been completed. Close inspection of pressure instrumentation indicated that a pressure instrumentation tube began leaking after the calibration, causing the apparent discrepancy between the weight flow at the venturi meter and the flap exits. The thrust calculation was resolved by setting discharge coefficient equal to unity. Previous experience with this flap arrangement produced discharge coefficients between 0.98 and 1.05, indicating a possible thrust calculation error within 5 percent. Posttest, the entire jet flap flow arrangement was set up in the flow calibration area to evaluate the leakage effect. Here it was found that small leaks had developed in the bellows as well as in the pressure instrumentation tube. Both leaks were corrected, and a posttest flow calibration was conducted to obtain pressure variations upstream and downstream of the venturi meter, as a function of flap F_1 and F_3 flow areas, to be used in place

of the leaking pressure instrumentation. With these values, the test data were reduced based on the pretest in-tunnel balance calibrations with the secondary air arrangement operational.

Data reduced by this procedure is presented and discussed in this report. Additionally, it was determined from the calibrations that the accuracy of chord force is hampered by having the bellows expansion in line with the balance. A typical result of the balance chord force with 5.7 pounds of thrust reads -33.7 pounds at 80 psf test dynamic pressure. The corrections based on the calibrations is +27.8 pounds resulting in a net chord force of -5.9 pounds. Further, it will be noted that 0.1 pound in chord results in 0.0025 drag coefficient. Normal force on the other hand, perpendicular to the axis of the bellows, has a correction less than 8 percent due to calibration.

SECTION IV

DISCUSSION OF RESULTS

JET THRUST EFFECTS

LIFT AND MOMENT

The effects of exiting cold nitrogen gas at various pressure ratios from the wing trailing edge jet flap are presented in Figures 8 through 17. Included in this data presentation are the effects of gross thrust coefficient, angle of attack, flap deflection, and the configuration influences of increasing jet flap span and tails. Primary effects upon the vehicle aerodynamics are an increase in lift, a negative moment increment, and a reduction in drag proportional to the thrust level.

The increments presented include the direct and induced effects of the flap blowing. That is

$$\Delta C_L = \left[C_T \, \mathrm{SIN}(\alpha + \delta) + C_{L_\Gamma}\right]_{\alpha,\,\delta = \text{CONSTANT}}$$

$$\Delta C_m = \left[C_T \, d/\bar{c}_w + C_{m_\Gamma}\right]_{\alpha,\,\delta = \text{CONSTANT}}$$

and, when taken at a constant flap deflection, do not include the unblown aerodynamic flap increment. The lift and moment values obtained at a constant angle of attack provide a measure of the thrust forces and the induced aerodynamic influences of this propulsion-airframe integration. The geometric angle for this type of jet flap is known because the flow is turned inside the flap at the hinge line and exits perpendicular to the physical trailing edge. The assumption here is that the flow field of the wing does not alter the jet efflux angle in the near field, that is $\theta_j = \delta_F$.

Incremental lift, at constant flap deflection for several angles of attack, is presented in Figure 8 for the 19.3-percent exposed span (F_1) and, in Figure 9, for the 43.2-percent exposed span (F_3) flap. Indicated on these figures is the magnitude of the direct lift component C_T SIN $(\alpha + \delta)$. The difference between the direct lift and the total increment (ΔC_L) is the induced lift (C_{L_Γ}).

Inspection of these figures indicates that the effects of pitch angle are greater than the direct lift geometric increase which results in an increase in airplane lift curve slope at this mach number. This effect is due to circulation, which reduces flow separation and improves the flow

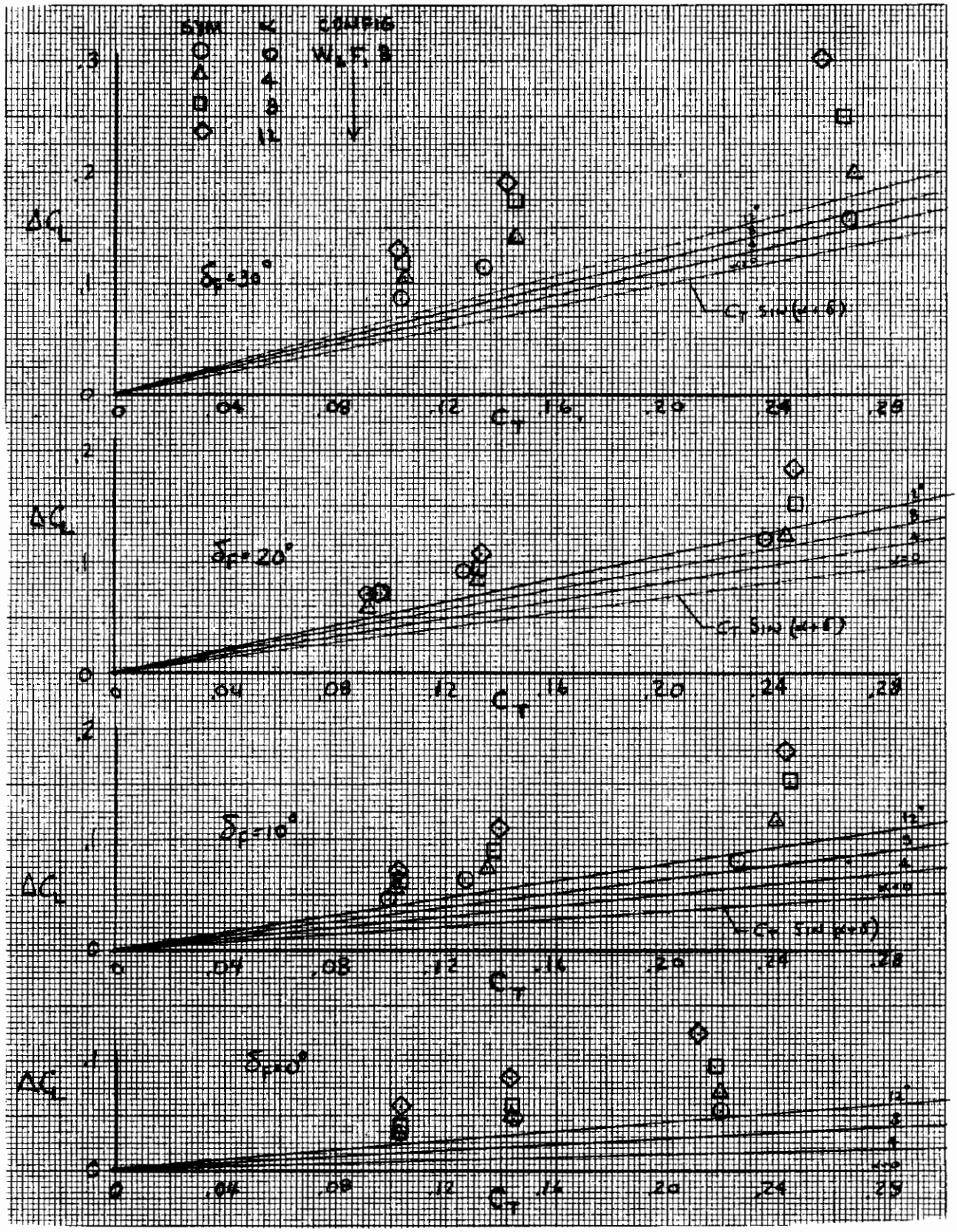

Figure 8. Effect of angle of attack (F_1).

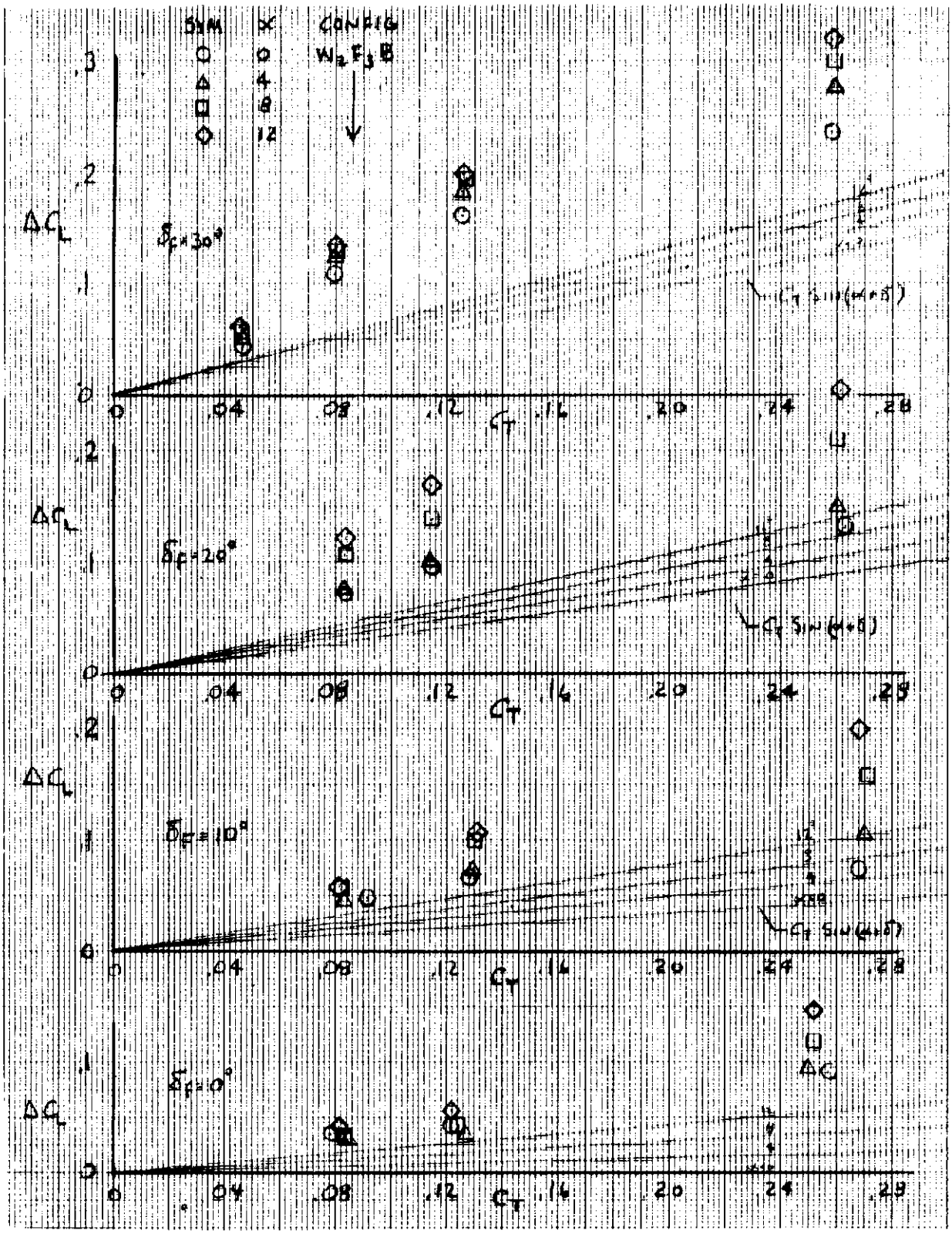

Figure 9. Effect of angle of attack (F_3).

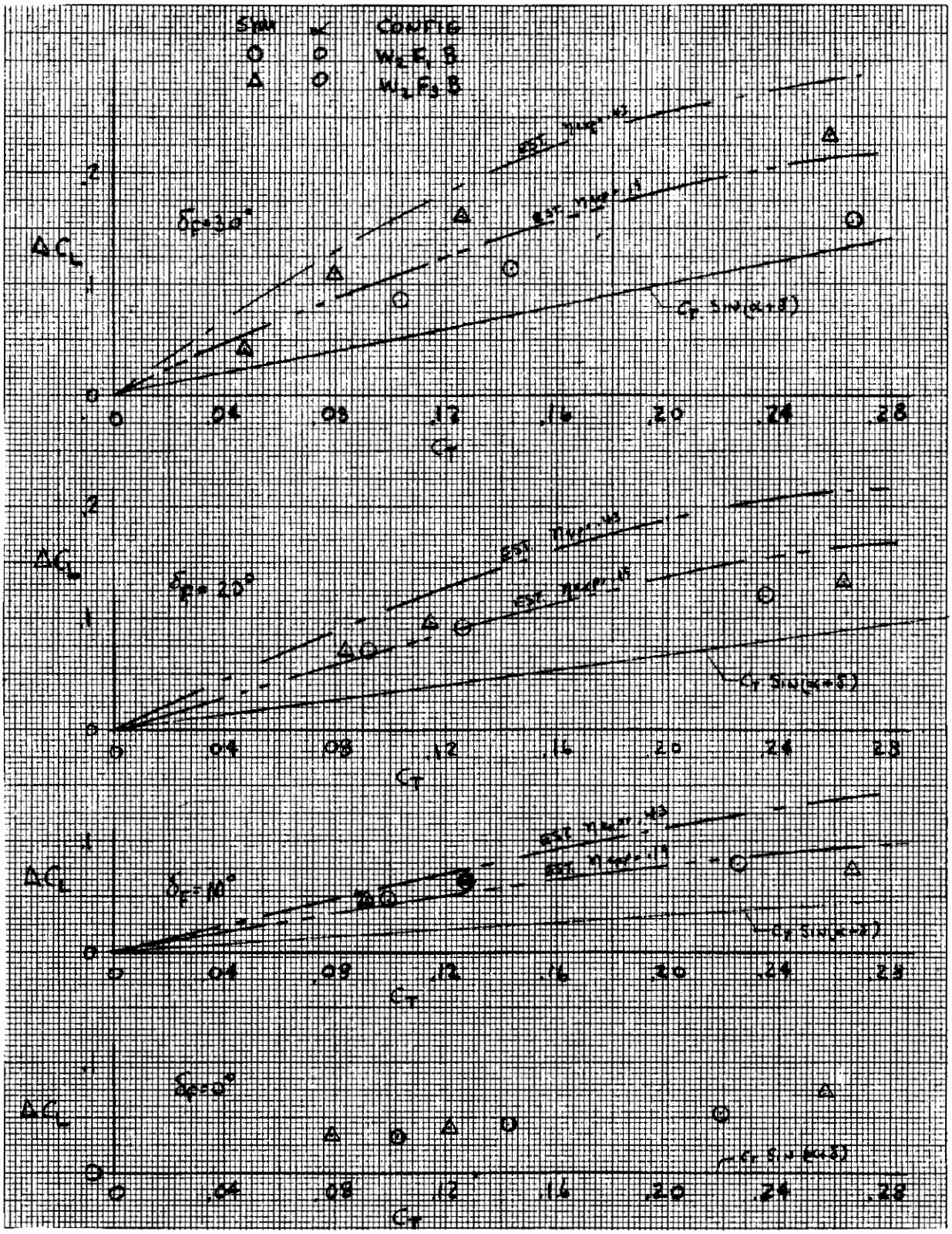

Figure 10. Effect of flap span on lift increment.

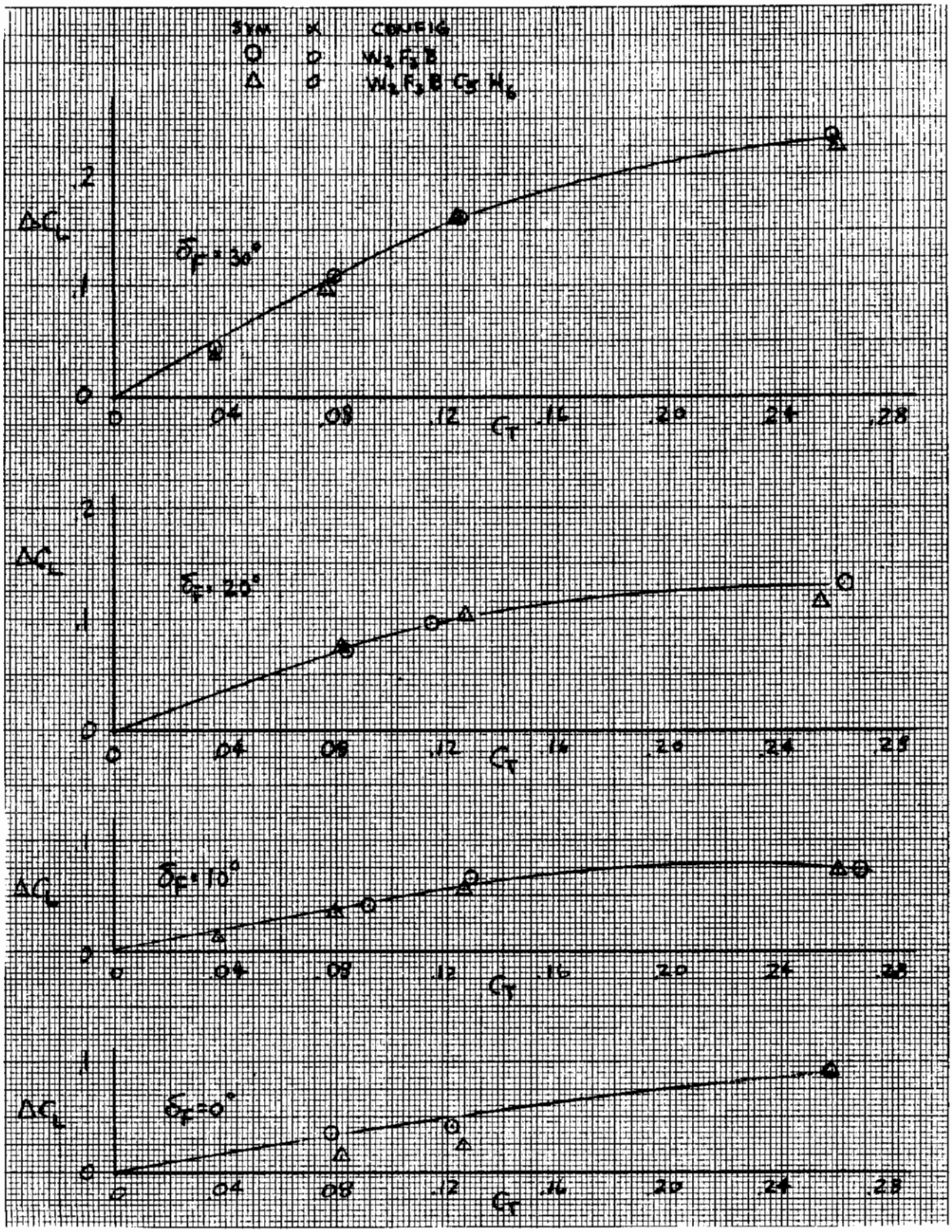

Figure 11. Effect of tails on lift increment.

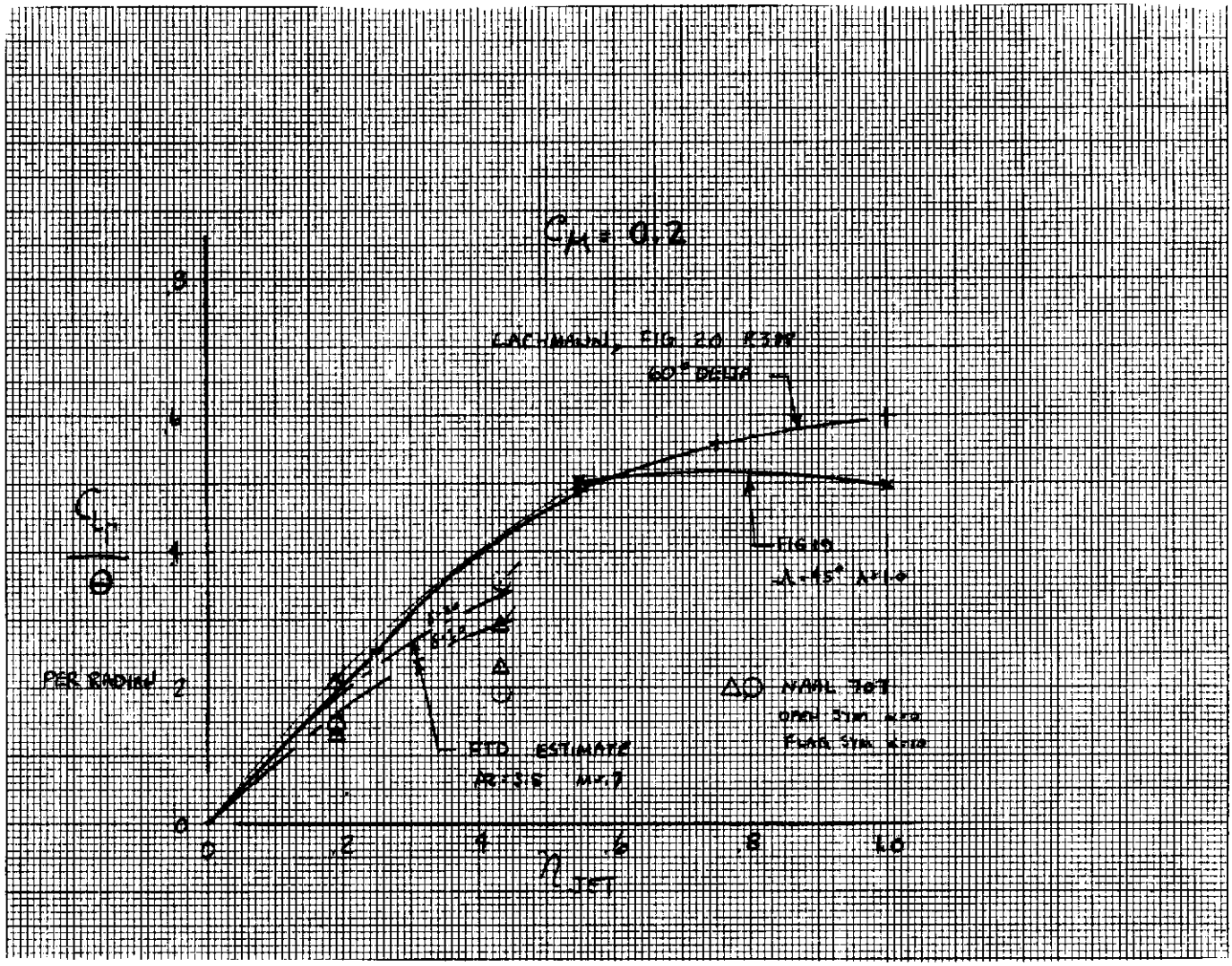

Figure 12. Comparison of flap span effects on induced lift.

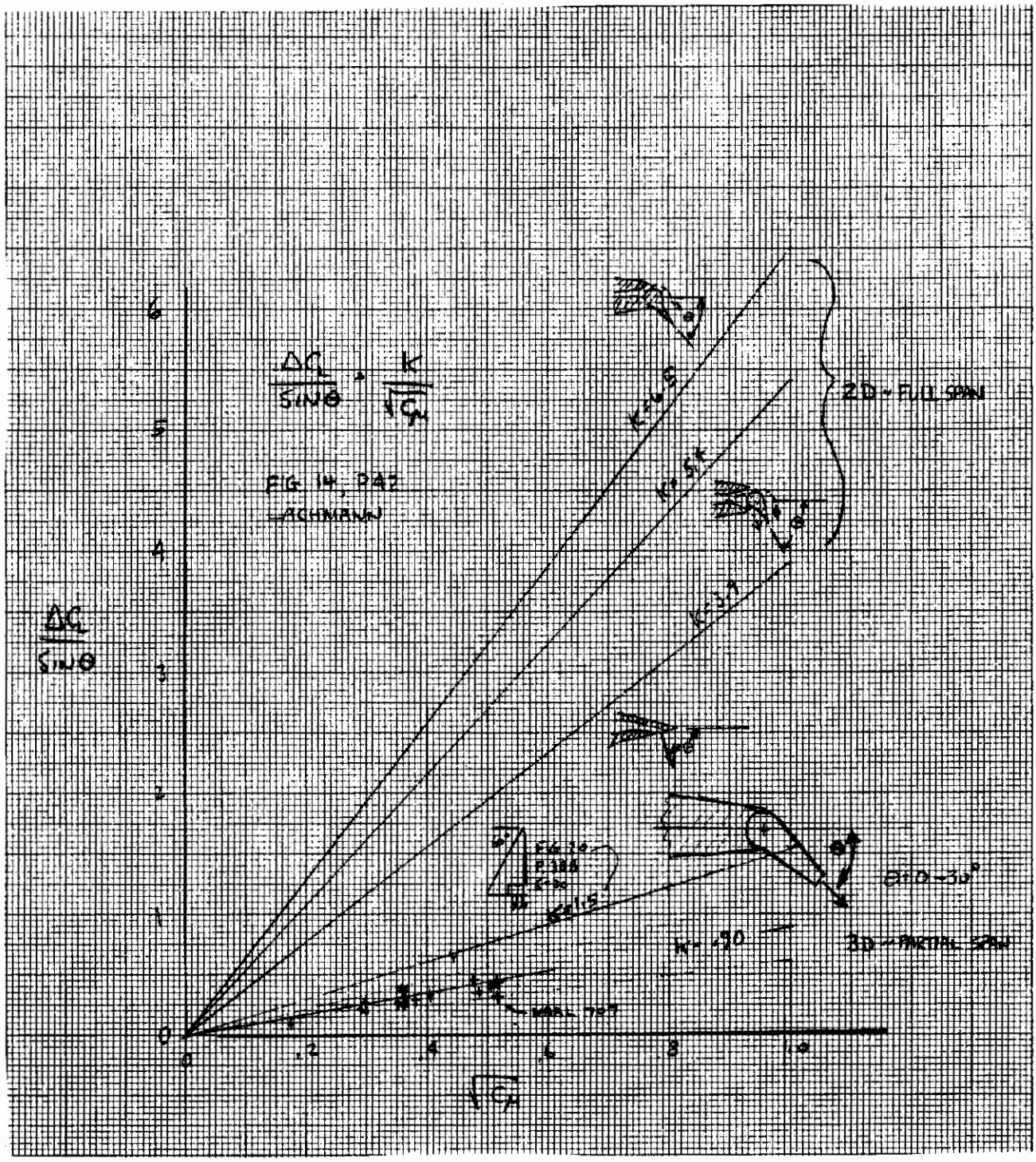

Figure 13. Comparison of lift increments.

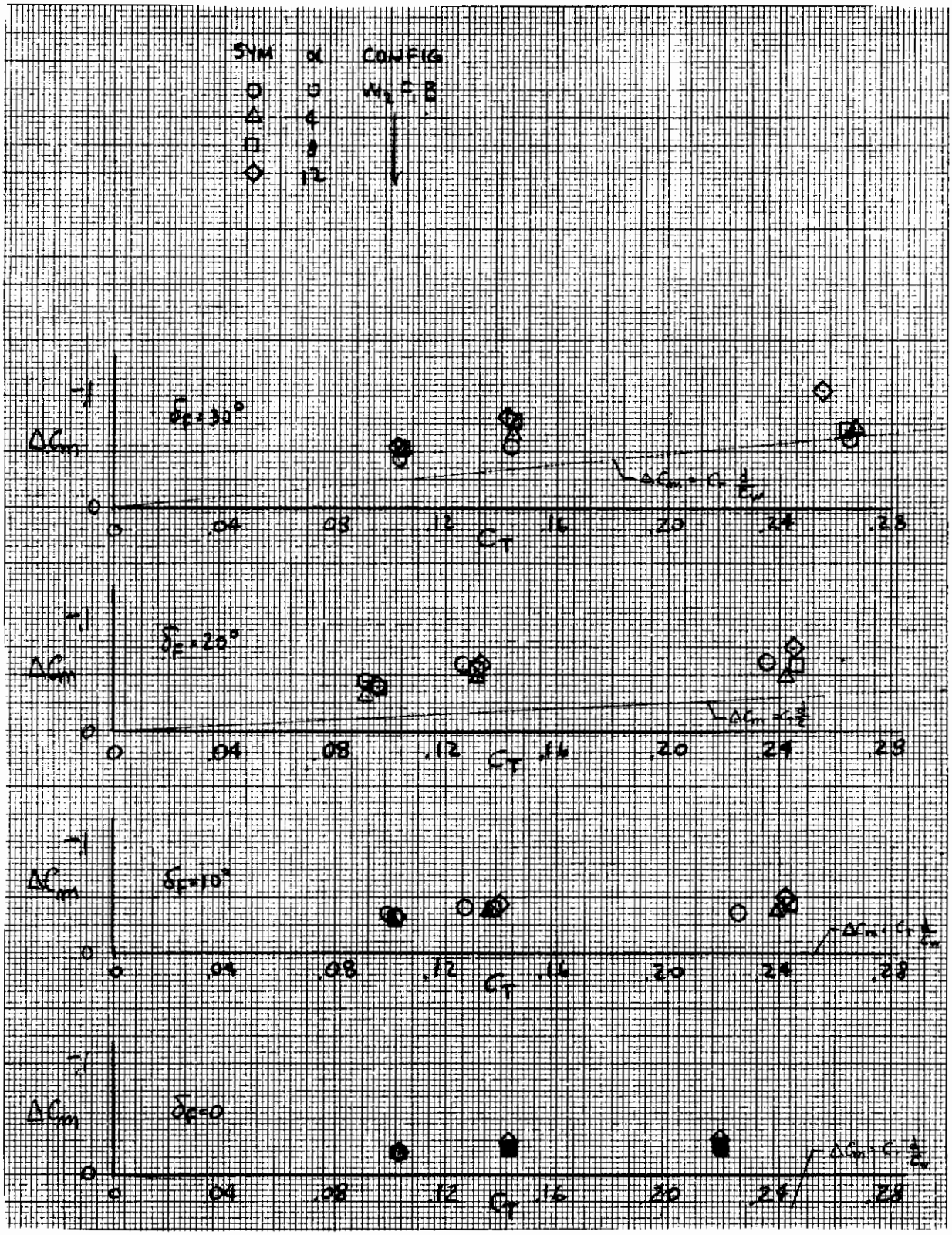

Figure 14. Effect of angle of attack (F_1).

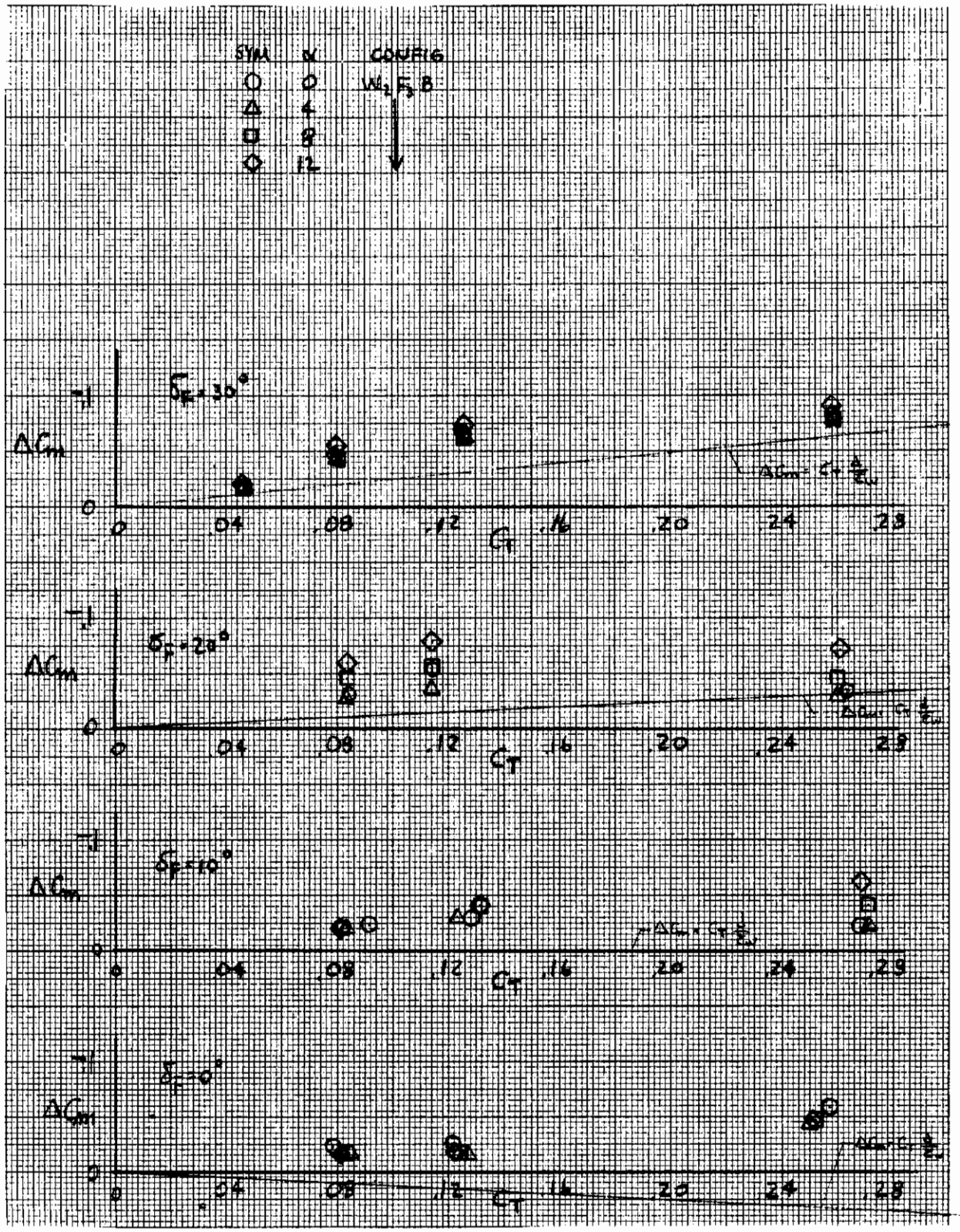

Figure 15. Effect of angle of attack (F_3).

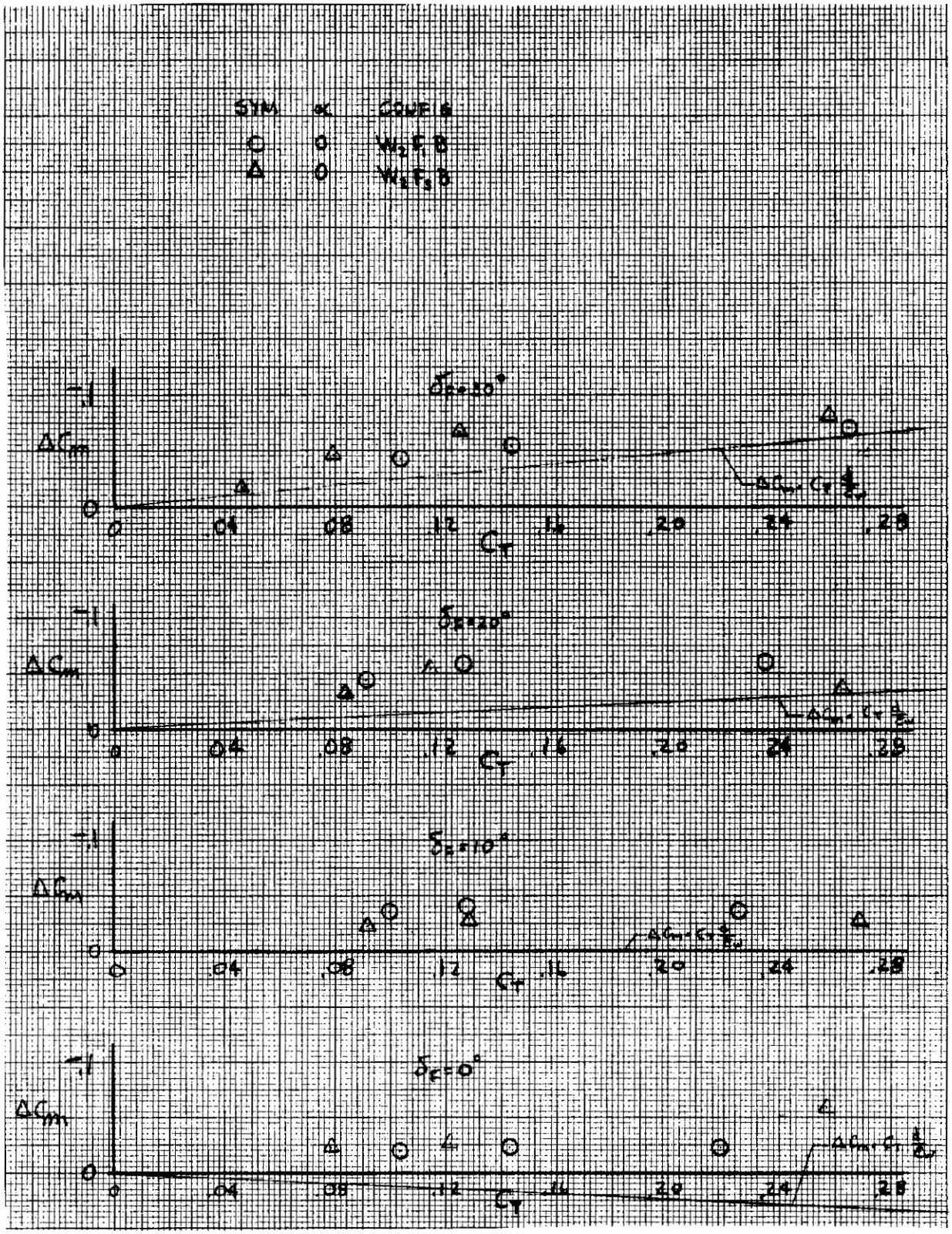

Figure 16. Effect of flap span on moment increment.

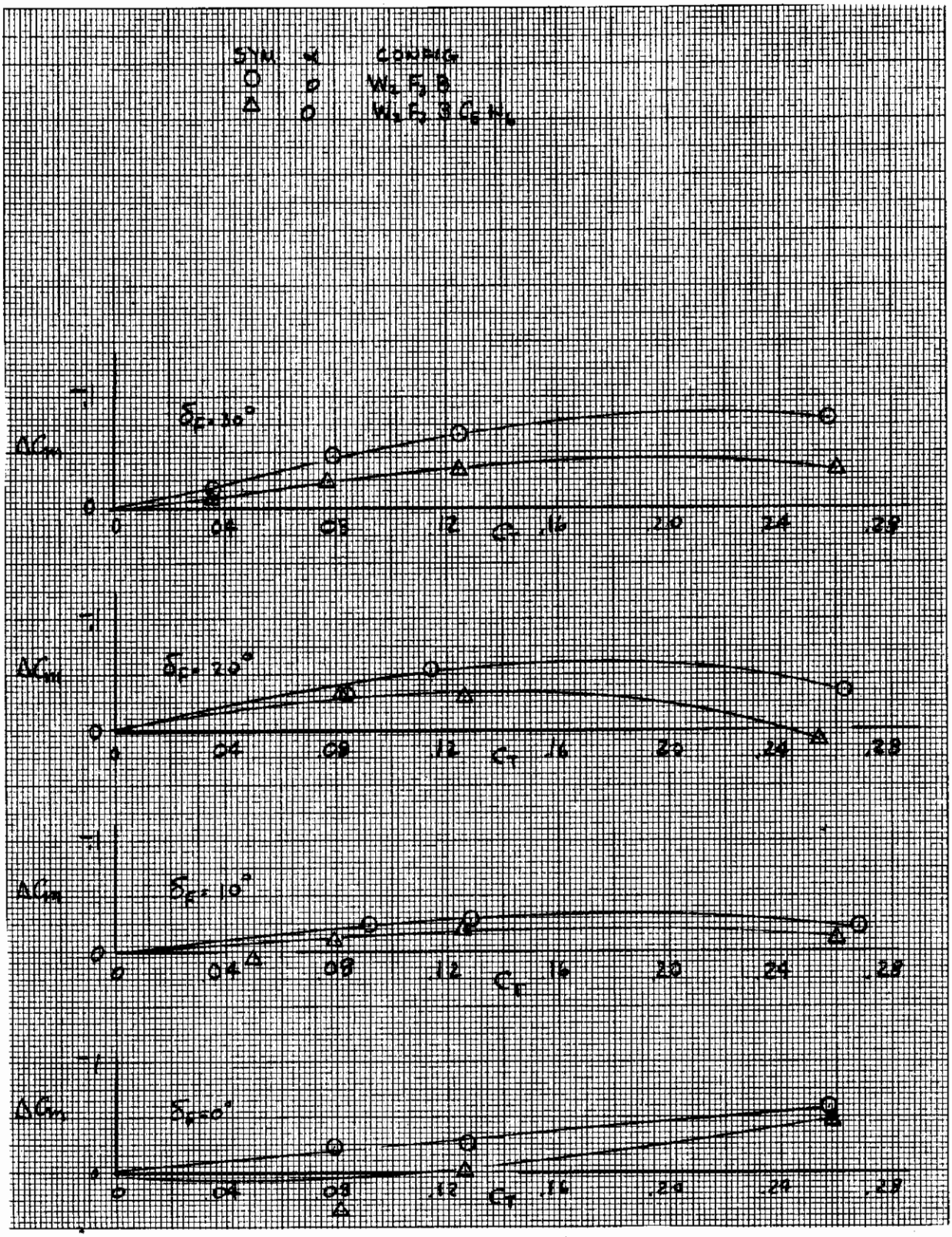

Figure 17. Effect of tails on moment increment.

about the wing in the vicinity of the blowing flaps. This effect is evident at zero geometric flap deflection as noted in these figures. A direct comparison of the two span flaps is shown in Figure 10 for the zero angle-of-attack condition. Of interest is the increase in circulation lift as a function of the flap span blowing. Also included on this figure is an estimate for the incompressible (M = 0.7) case used in the vehicle design trades. Fair agreement is evident for this comparison. Another approach to presenting the effects of span is the variation of Figure 12 where the current data results are compared to the 0.7 mach estimate and the theoretical data of Figures 19 and 20, of Reference 2. The ordinate of this figure is induced lift per radian of jet deflection versus span ratio of the jet. Three things are shown here, all for a momentum coefficient of 0.2: (1) the theoretical variation of Reference 6, (2) the design data base for the FTD, and (3) the results of the current test. The NAAL 707 results agree favorably with the FTD data base when the increase in induced lift with angle of attack is included, but remain below the levels of the theoretical 60-degree delta. It will also be noted that the theoretical results from Reference 2 assume flow turning at the trailing edge for this case, while the current test data exits the flow parallel to the deflected flap chord. This difference in the method of flow turning will reduce the induced lift expected for a given flap span and deflection.

Reference 2, in bringing forward the long history of research in boundary layer and circulation control, continues to be a source for timely comparisons. From this reference, the data of Figure 13 is derived with the purpose of comparing the current experimental results and determining the differences in level between the two-dimensional full span and three-dimensional partial span flap circulation. As evident, the current data are significantly lower than the two-dimensional results and present a scatter in K between 0.6 and 1.15. A mean of 0.90 represents the results. Reference 2 reports that the increase in lift is proportional to the sine angle of the flow deflection and the square root of the exit momentum, as expressed by

$$\Delta C_L = K \, \text{SIN} \, \delta \sqrt{C_\mu}$$

and the efficiency of lift production

as $$E = \frac{\Delta C_L}{C_\mu \, \text{SIN} \, \delta} = \frac{K}{\sqrt{C_\mu}}$$

where K is the slope of the variations on Figure 13. For this system, the current NAAL 707 data produces an efficiency (E) equal to 1.8 at C_T = 0.25 and 2.85 at C_T = 0.10 which reflects the expression for a constant K; i.e., the efficiency increases with decreasing thrust coefficient. Also included on this figure is a theoretical result (Figure 20 of Reference 2) for a low AR 60-degree delta, and restated for a partial span flap equal to 43-precent span, which corresponds to the exposed span ratio of the NAAL 707 data. The theoretical results indicate a K = 1.5 for the three-dimensional case, the point here being that the two-dimensional results are several times greater than the three-dimensional levels.

The effects of adding the canard and horizontal tail arrangement are shown in Figure 11. The significance of this presentation is the concern that the canard flow will disturb the circulation effects of the jet flap or that the downwash field created by the jet efflux will alter the horizontal tail input. The results of this jet flap arrangement do not indicate any reduction in lift increment due to adding these components.

Increments in pitching moment due to direct and induced thrust (ΔC_m) are shown in Figures 14 and 15 for the 19.3- and 43.2-percent span, respectively. Clear from these figures, and the comparison of Figure 16, is the negative increment associated with the induced moment. The direct moment is shown in the same fashion as noted previously for lift, but the moment being only a function of the gross thrust and the perpendicular distance from the thrust vector to the reference moment center does not include a term related to pitch angle. The negative value is a result of the jet circulation improving the net loading over the inboard section of the wing producing an effective camber of the wing section by the jet efflux and thus a rearward movement of the center of pressure. In most cases, the moment increment follows directly the trends of the lift increments. Effects of adding canards and the horizontal tail arrangement are shown in Figure 17. This figure indicates a departure from the lift increment result in that the complete configuration exhibits a lower induced moment increment than the wing body. This effect was noticed in the transonic test and is related to the downwash increment in the horizontal tail input.

The impact of this level of moment increment on airplane trim with the horizontal tail arrangement results in an additional surface deflection. The effectiveness of the tail ($C_{m\delta H}$ = 0.021) indicates that, for the wind tunnel model, 5 degrees of deflection will compensate for the largest direct and induced moment (ΔC_m) found. Of course, if the moment required to trim is negative, as may be the case for a relaxed static margin vehicle, the direct and induced moments will reduce the amount of surface deflection to trim.

DRAG

Jet thrust effects on drag are shown in Figures 18 through 25, for two flap span ratios, in drag polar form at various gross thrust coefficients. Data presented in this form are the basis for constructing analysis plots and, with constant angle-of-attack lines indicated, provide a measure of direct and induced thrust effects. For example, the greater the slope of the constant alpha line, the greater the induced lift effects, and possibly a more favorable drag polar shape for a given thrust level. In the final analysis, the reduction in drag achievable for a given lift coefficient and thrust level is of primary importance.

Variations of effective thrust recovery are shown in Figures 26 through 31. The term "effective" is employed because the increment in drag applied is from the thrust coefficient zero (power off) level, which has viscous effects and possibly includes flow separation. The powered increment will consequently include boundary layer control effects. This will result in higher levels of thrust recovery. These figures indicate the 100-percent recovery level ($- C_D = C_T$). Inspection of these variations indicates two things:

1. The effective recovery is greater than 100 percent for most cases.

2. There is a consistent increase in recovery with increasing lift coefficient for both flap configurations.

Effective thrust recoveries are also shown for constant angles of attack (Figures 32 and 33) with the larger span flap F_3. This presentation is useful in resolving the geometric gross thrust component [C_T COS ($\alpha + \delta$)], shown at three angles of attack. Although these variations reflect the drag results in more reasonable recoveries, airplane drag analysis must be resolved at a given lift rather than angle of attack.

Recoveries greater than 100 percent tend to make one suspicious and recall the discussion of Section III in relation to the accuracies found for this model installation in chord force. Here it was noted that the correction to the balance reading with thrust on was 83 percent, in effect the difference between two large numbers to produce a corrected level. This corrected level is then compared to the thrust value, which itself could be in error 5 percent. Restating the actual values, a balance reading of -33.7 pounds, a correction of 27.8 pounds results in a net -5.9 pounds compared to a 5.7 pounds calculated thrust level. Also noted in Section III is the sensitivity to chord load of 0.0025 drag coefficient per 0.1 pound axial force.

Because of these calibration difficulties, it is recommended that the drag levels be evaluated in terms of trends rather than absolute levels.

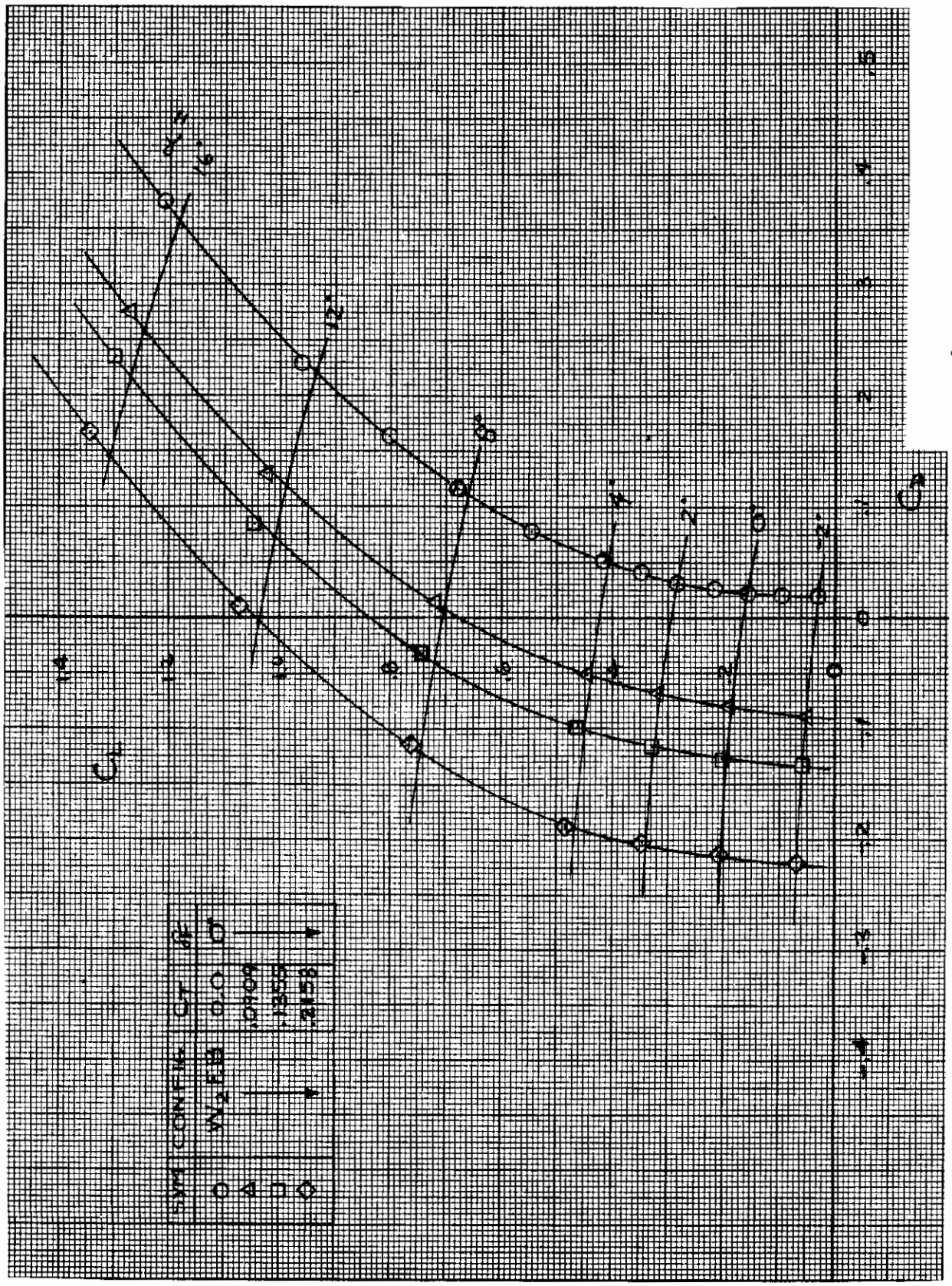

Figure 18. Drag polar at various C_T - W_2F_1B δ_F = 0°.

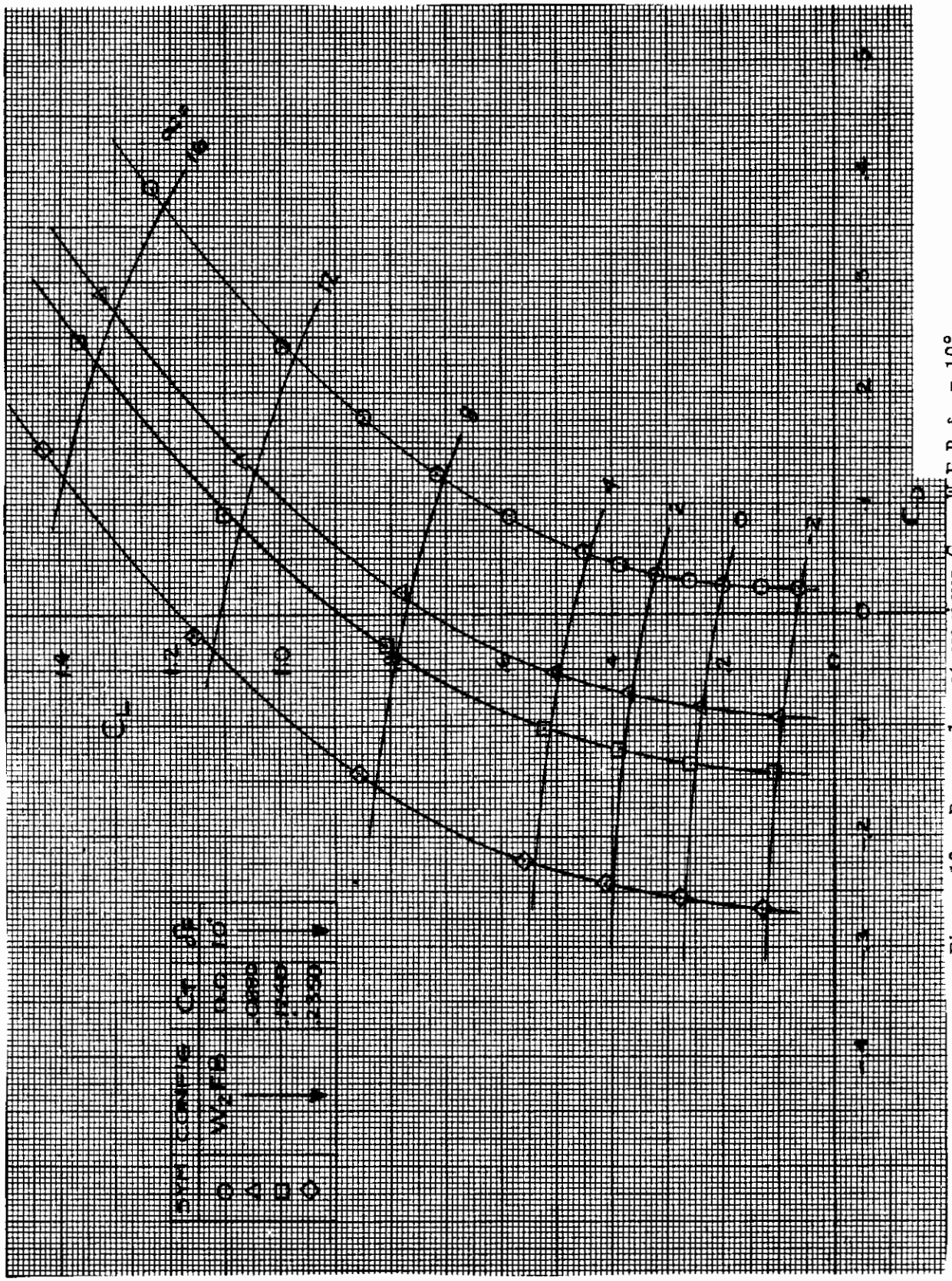

Figure 19. Drag polar at various $C_T - W_2F_1B\ \delta_F = 10°$

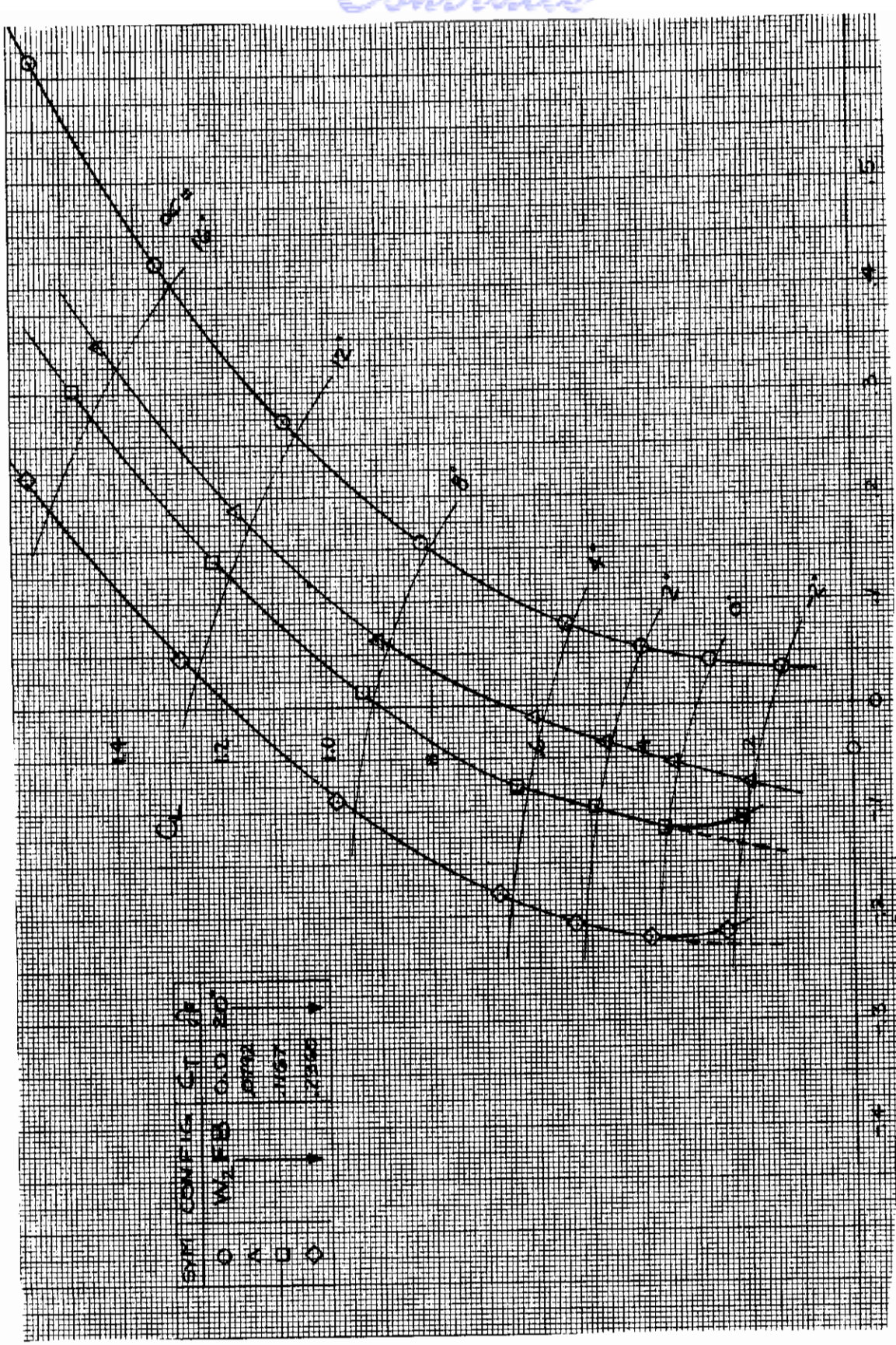

Figure 20. Drag polar at Various C_T - W_2F_1B δ_F = 20°.

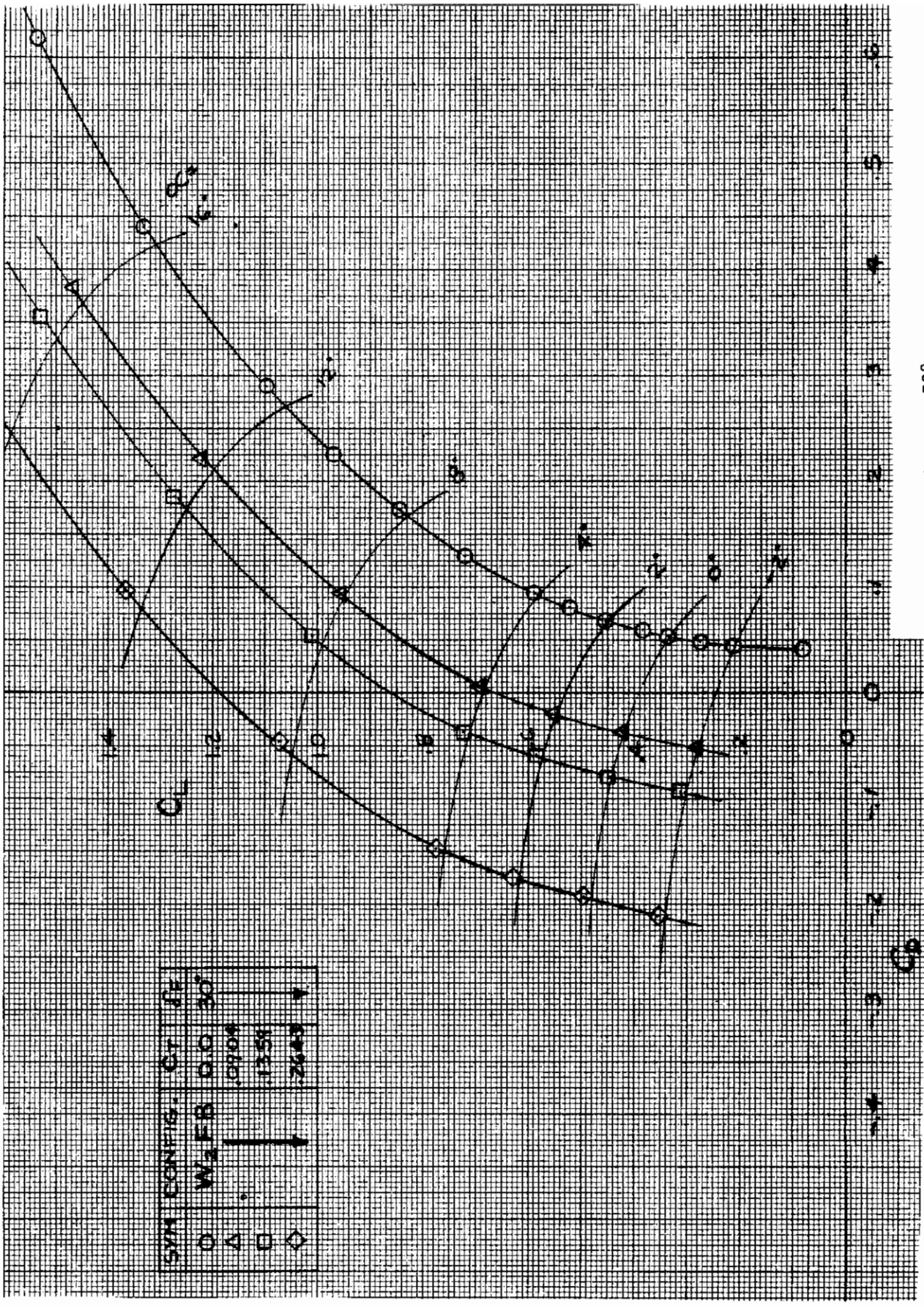

Figure 21. Drag polar at various C_T - W_2F_1B δ_F = 30°.

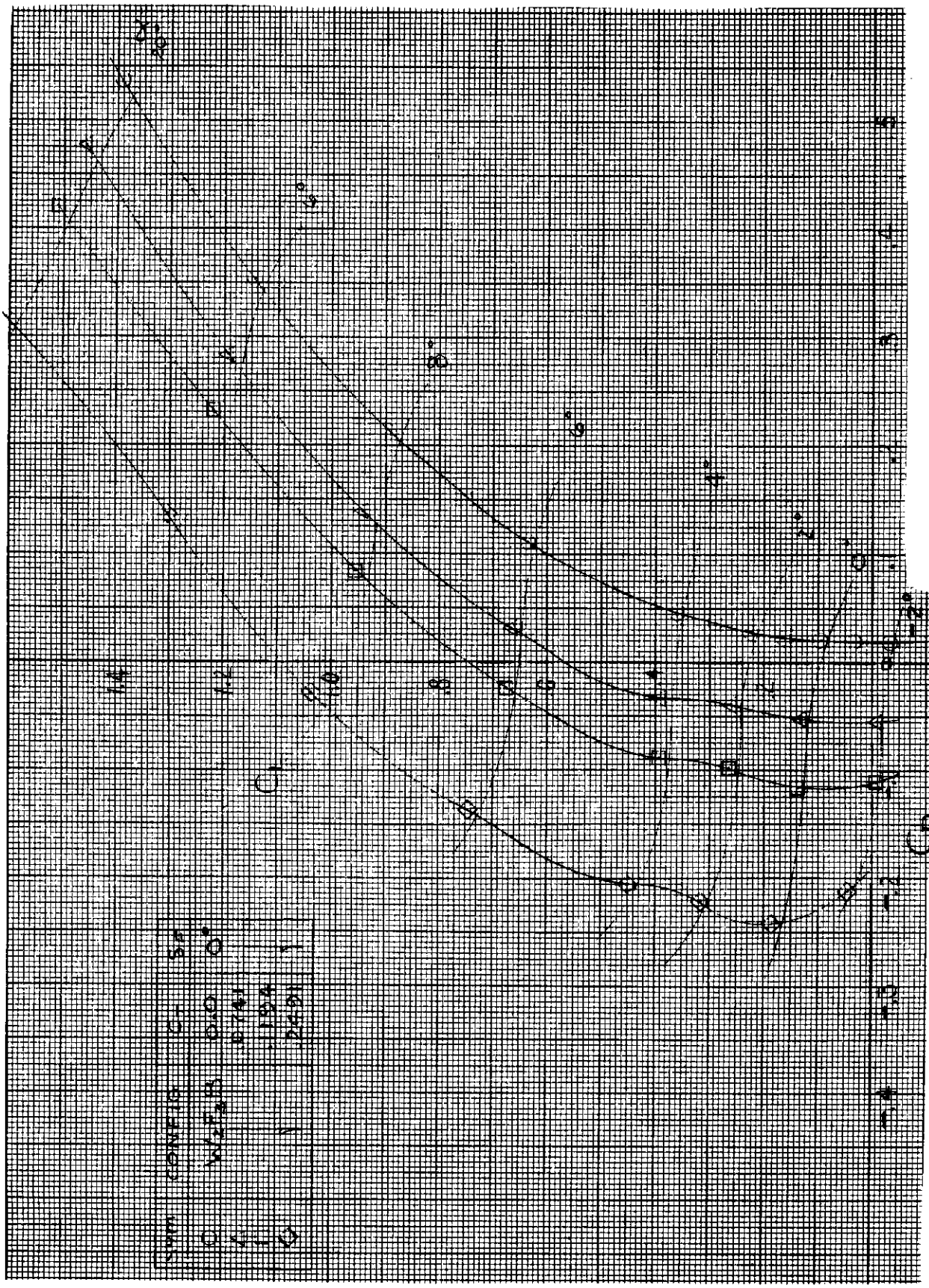

Figure 22. Drag polar at various C_T - W_2F_3B δ_L = 0.

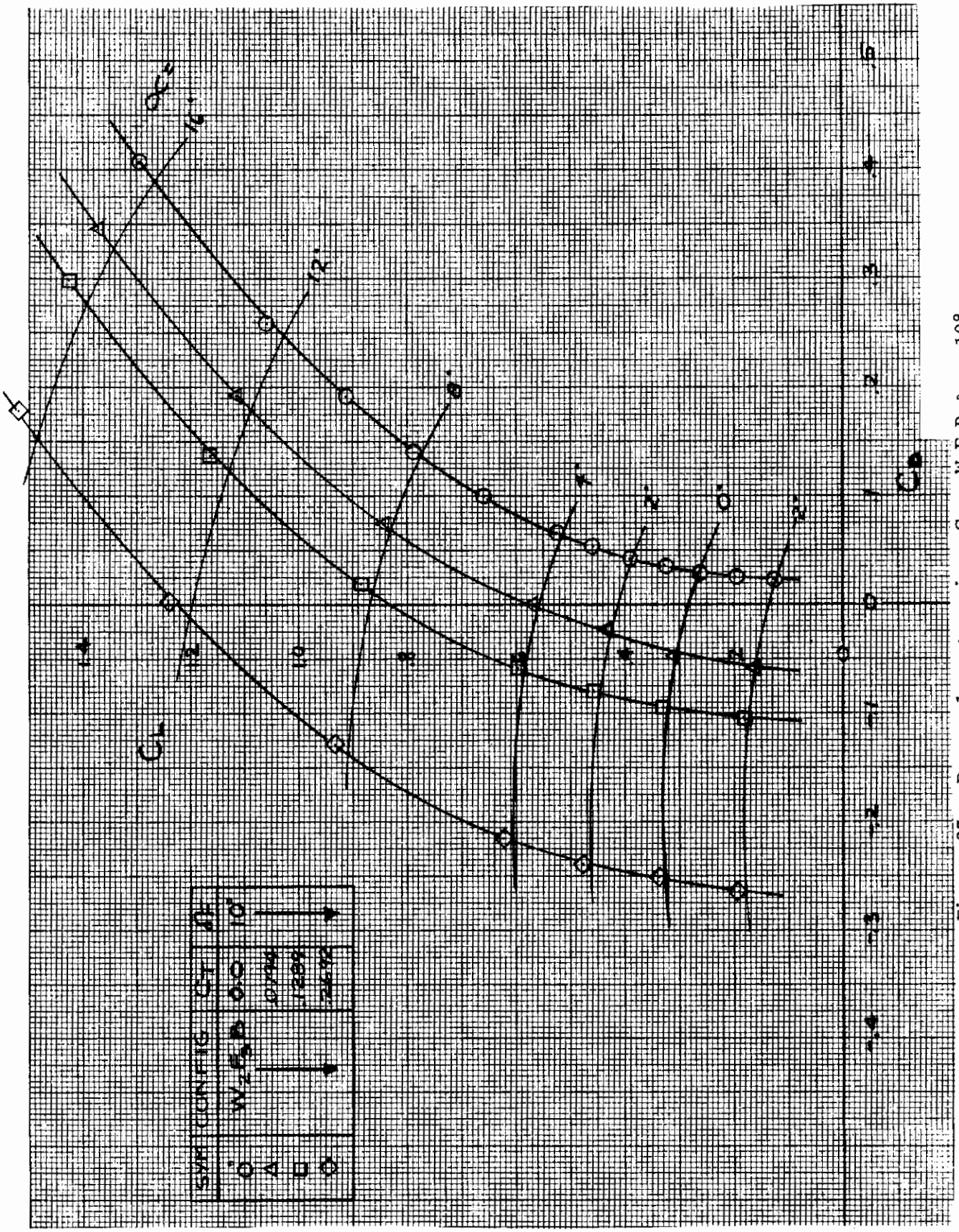

Figure 23. Drag polar at various C_T - W_2F_3B δ_F = 10°.

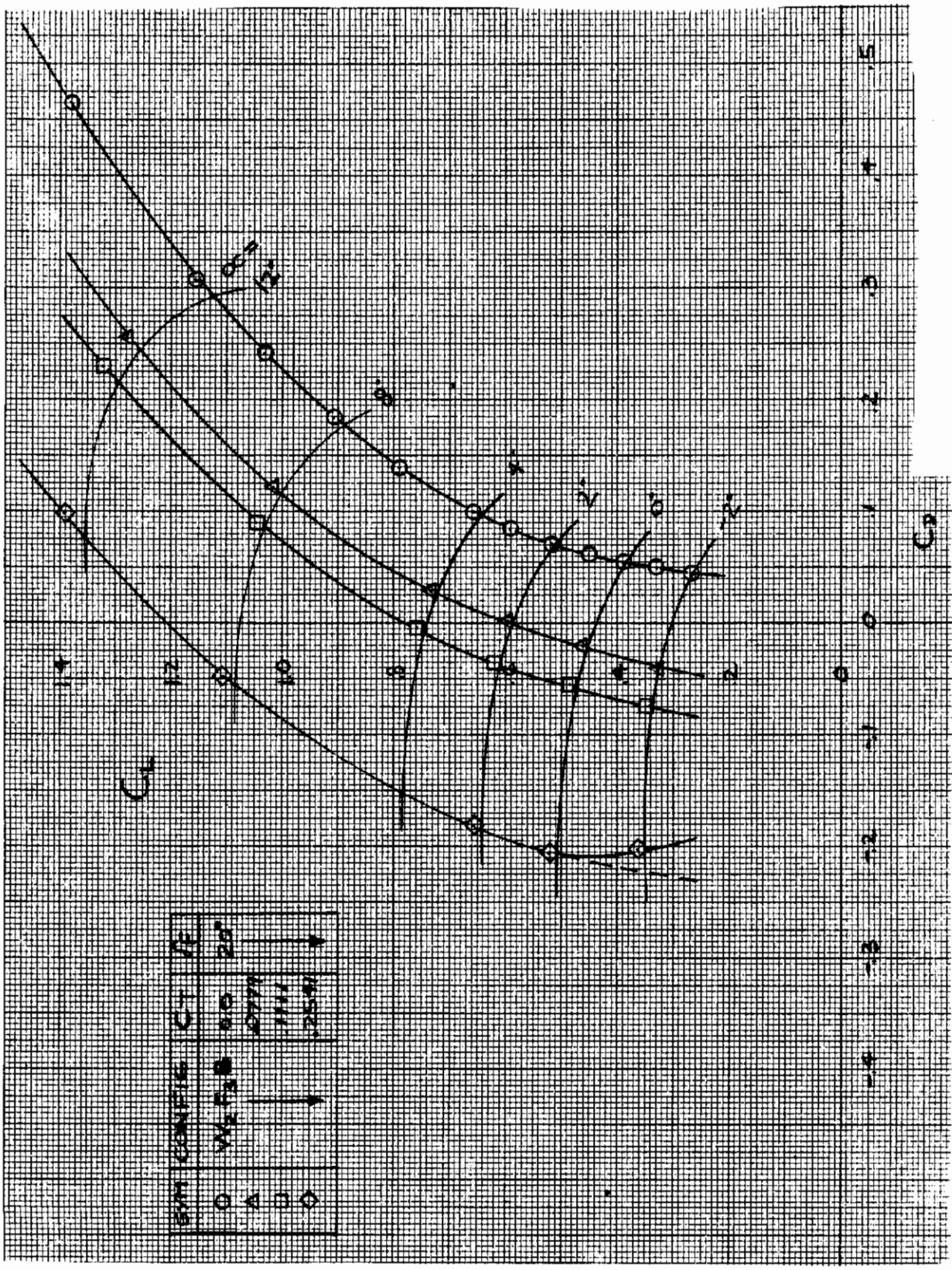

Figure 24. Drag polar at various C_T - W_2F_3B δ_F = 20°.

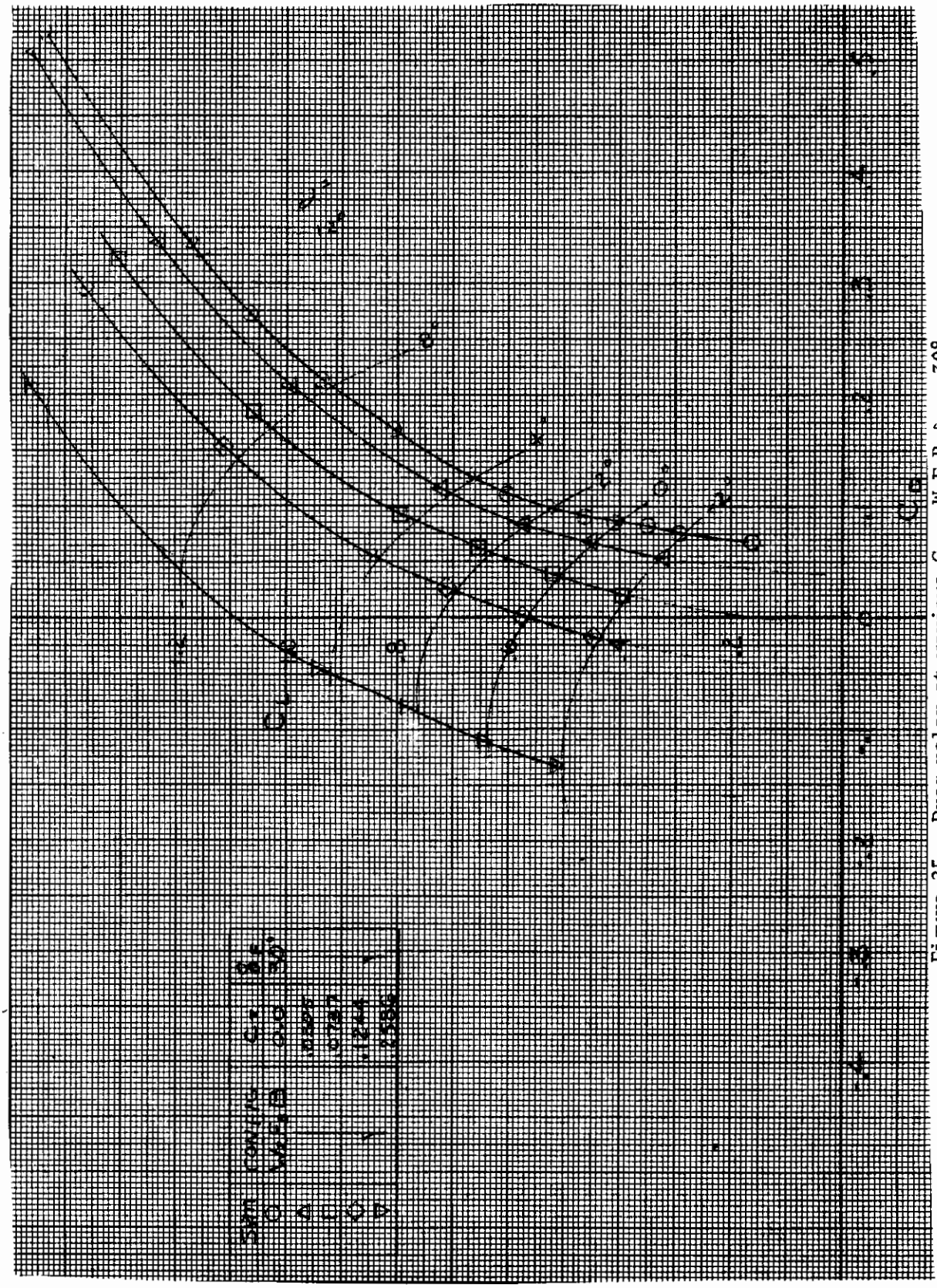

Figure 25. Drag polar at various C_T - W_2F_3B δ_F = 30°.

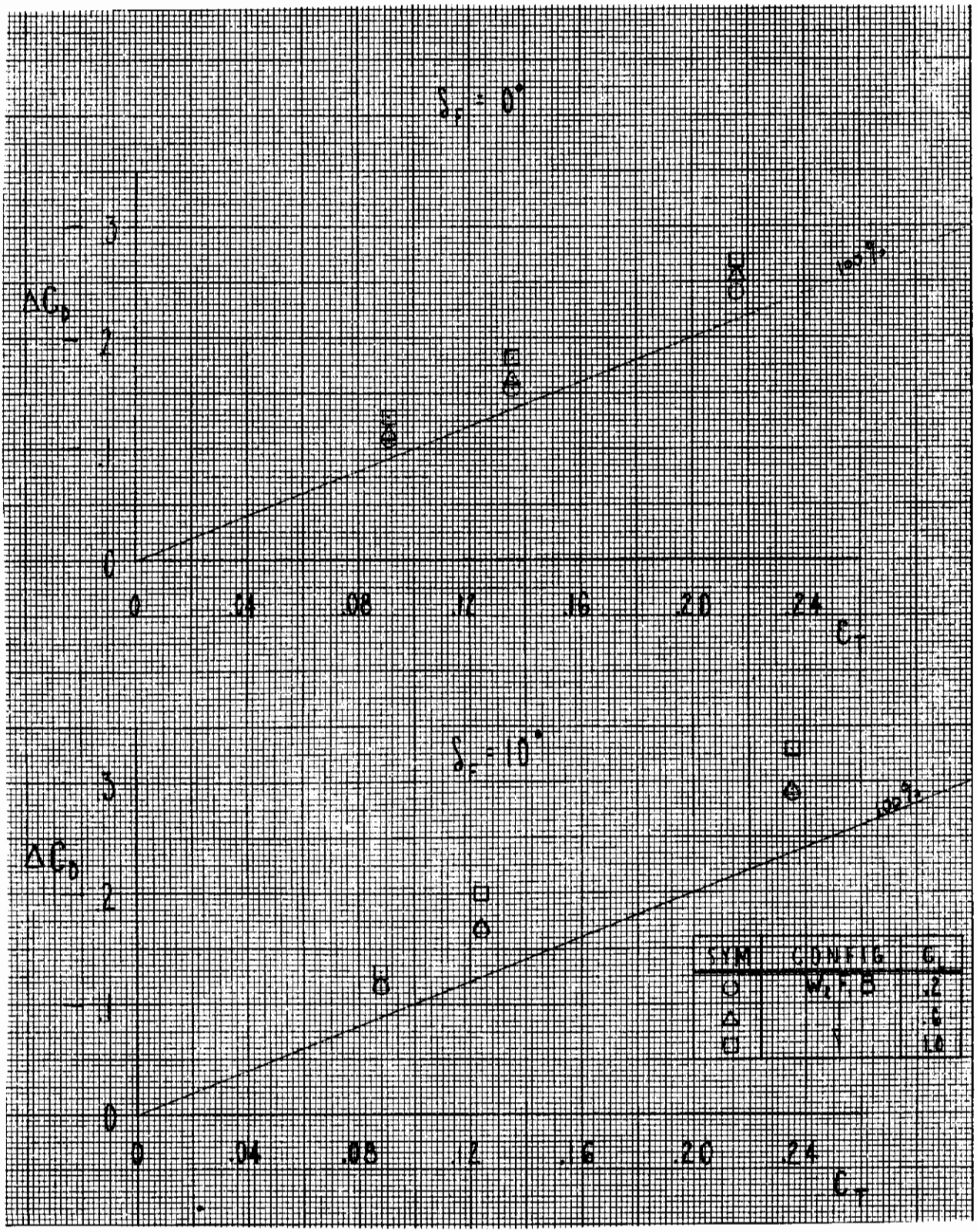

Figure 26. Effective thrust recovery (F_1).

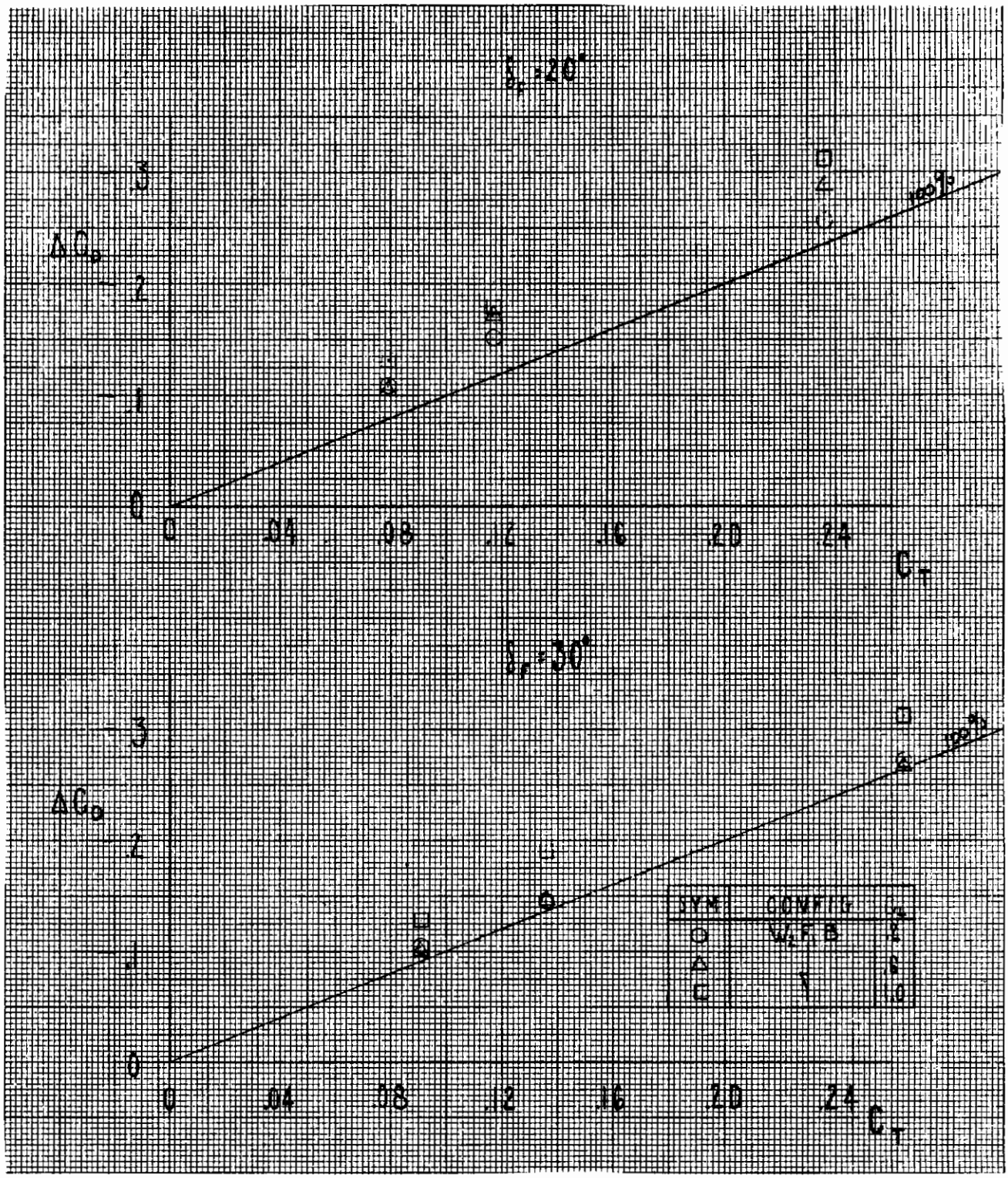

Figure 27. Effective thrust recovery (F_1).

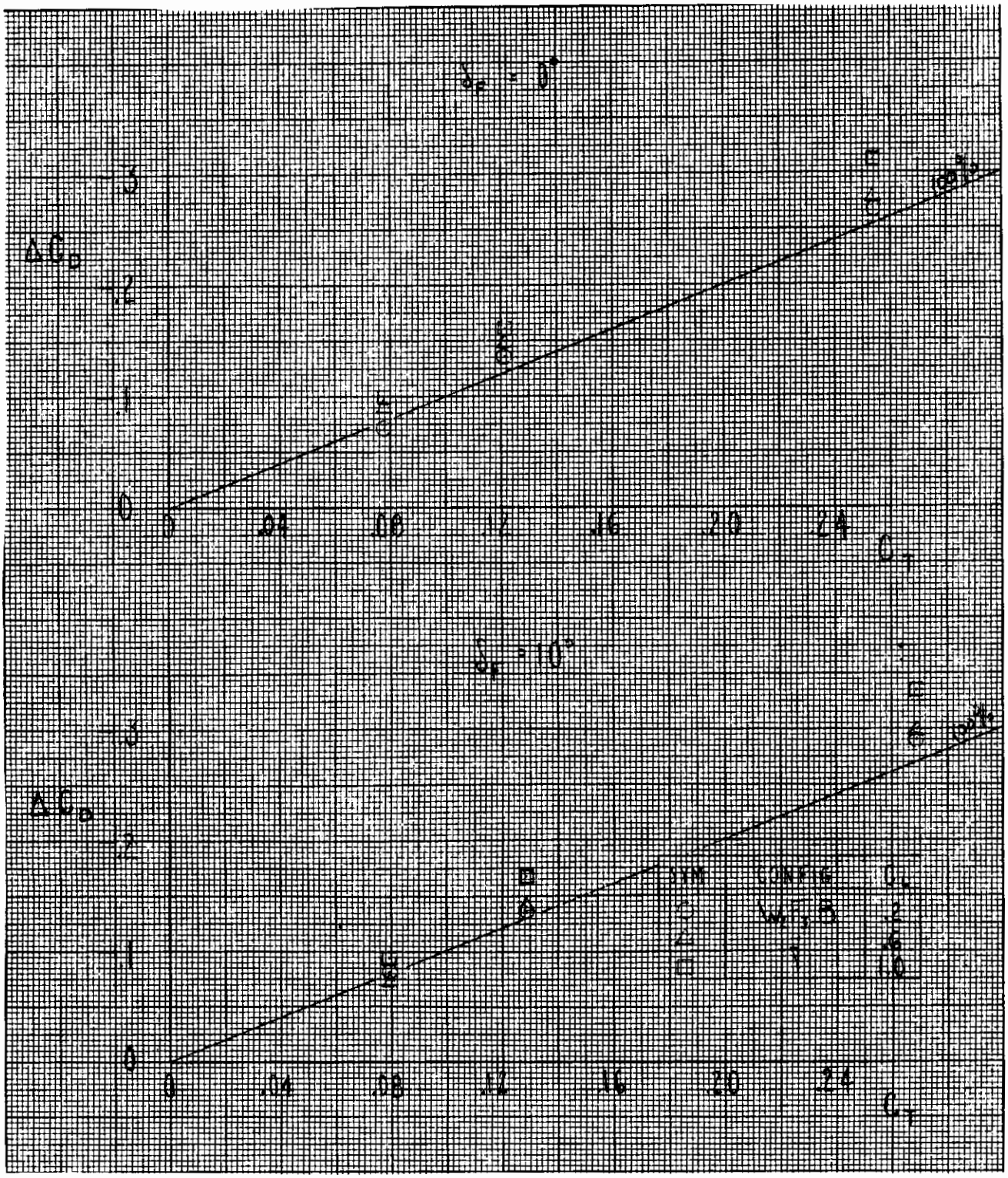

Figure 28. Effective thrust recovery (F_3).

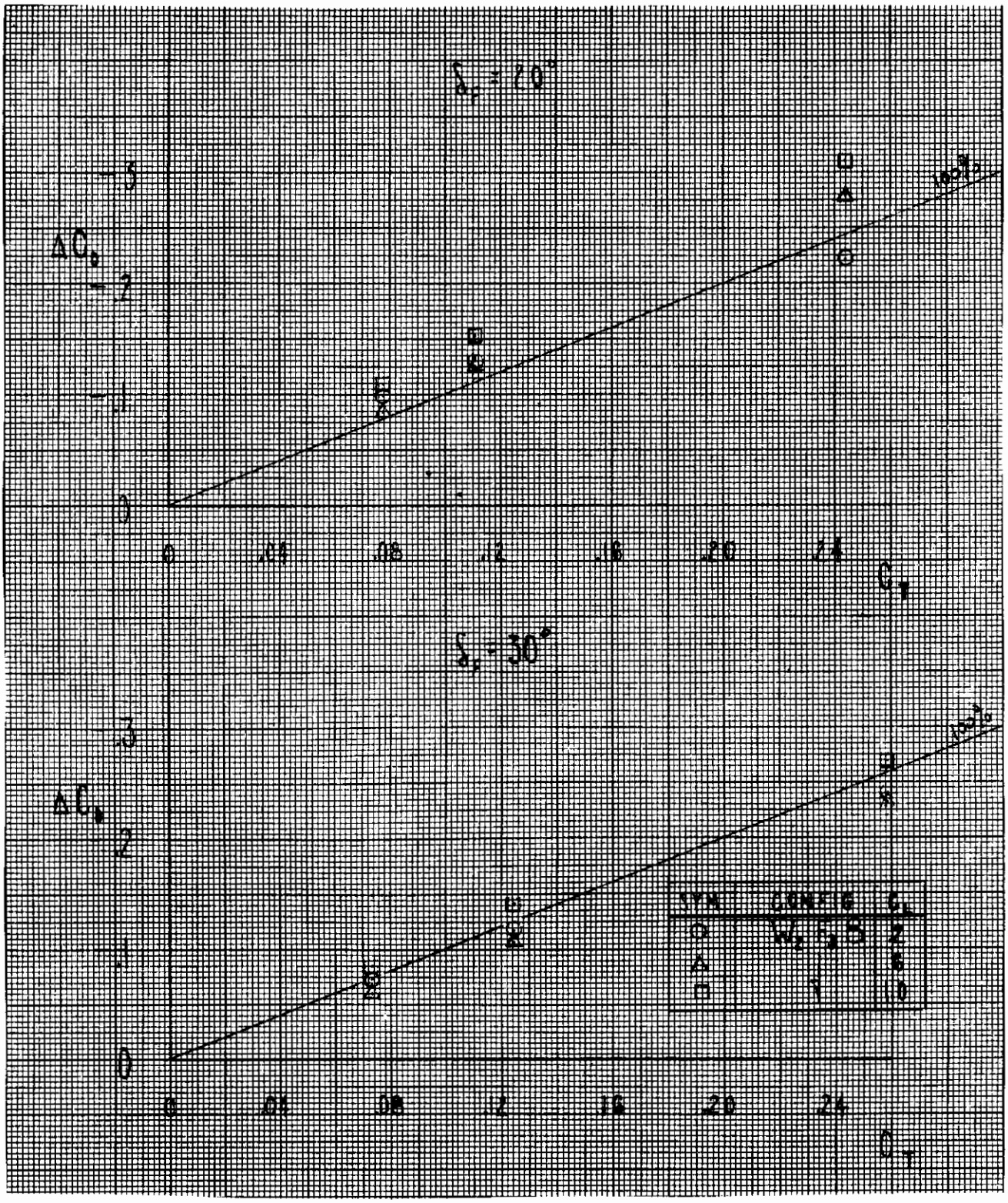

Figure 29. Effective thrust recovery (F_3).

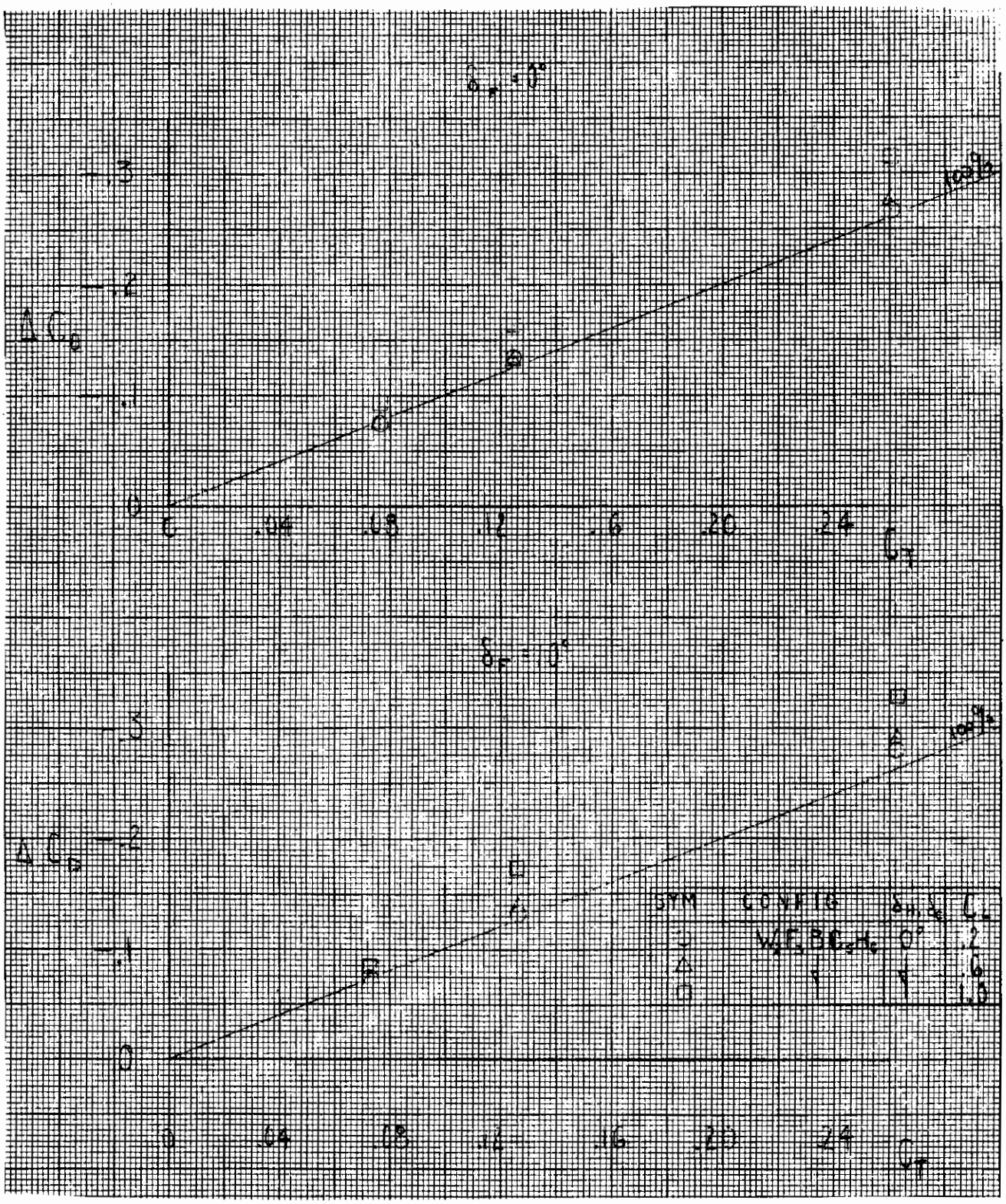

Figure 30. Effective thrust recovery, full configuration.

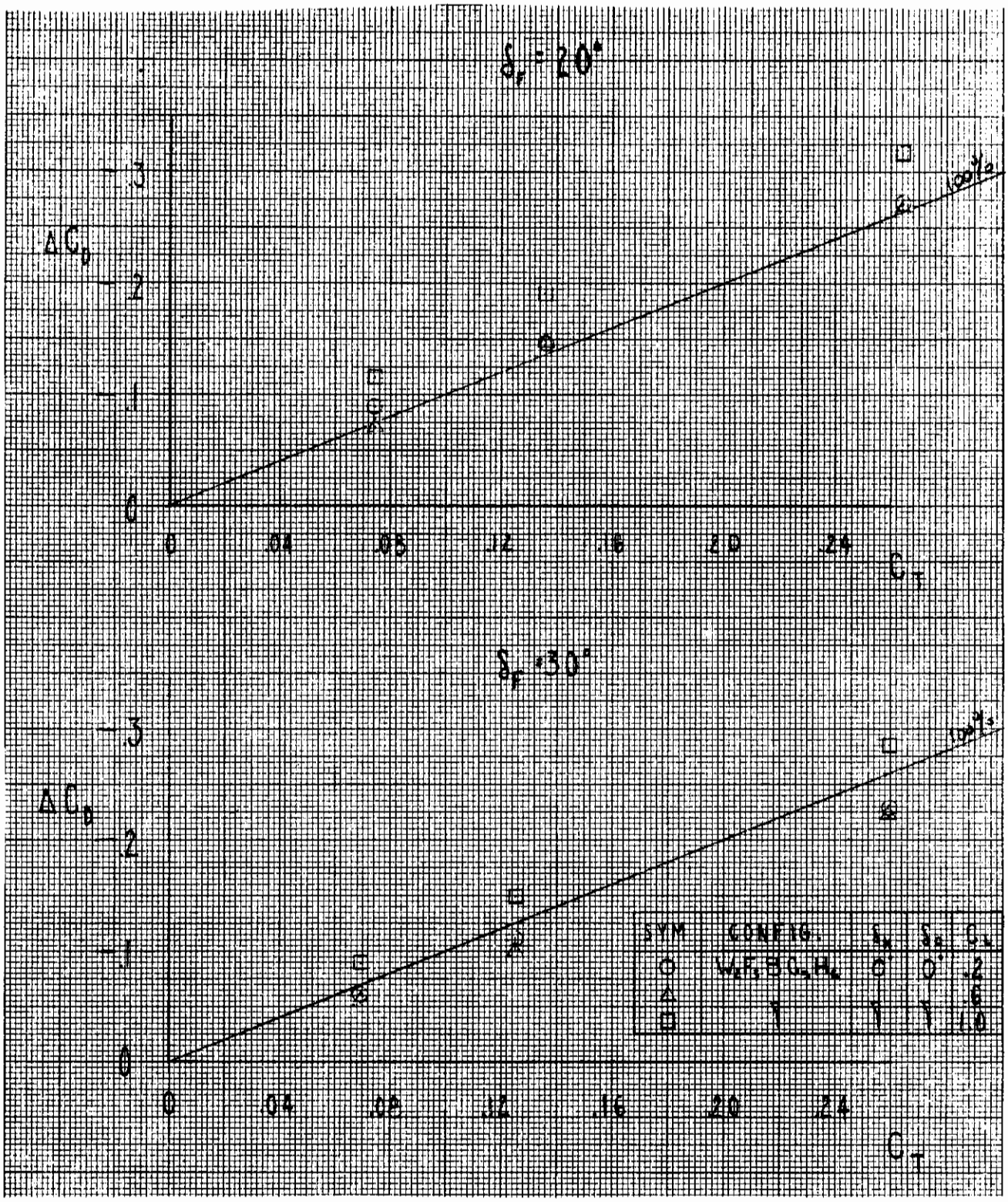

Figure 31. Effective thrust recovery, full configuration.

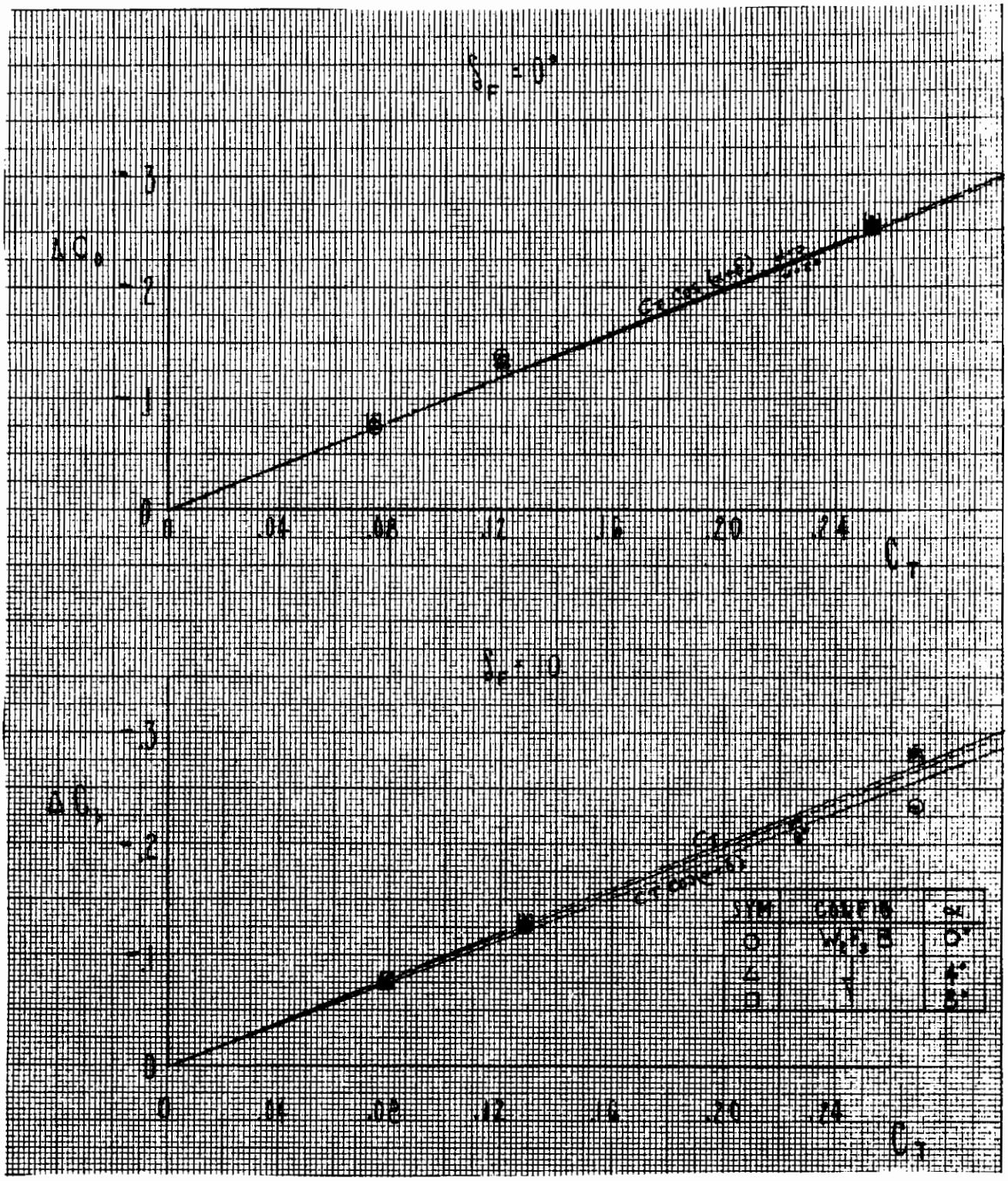

Figure 32. Effective thrust recovery (F_3) constant alpha.

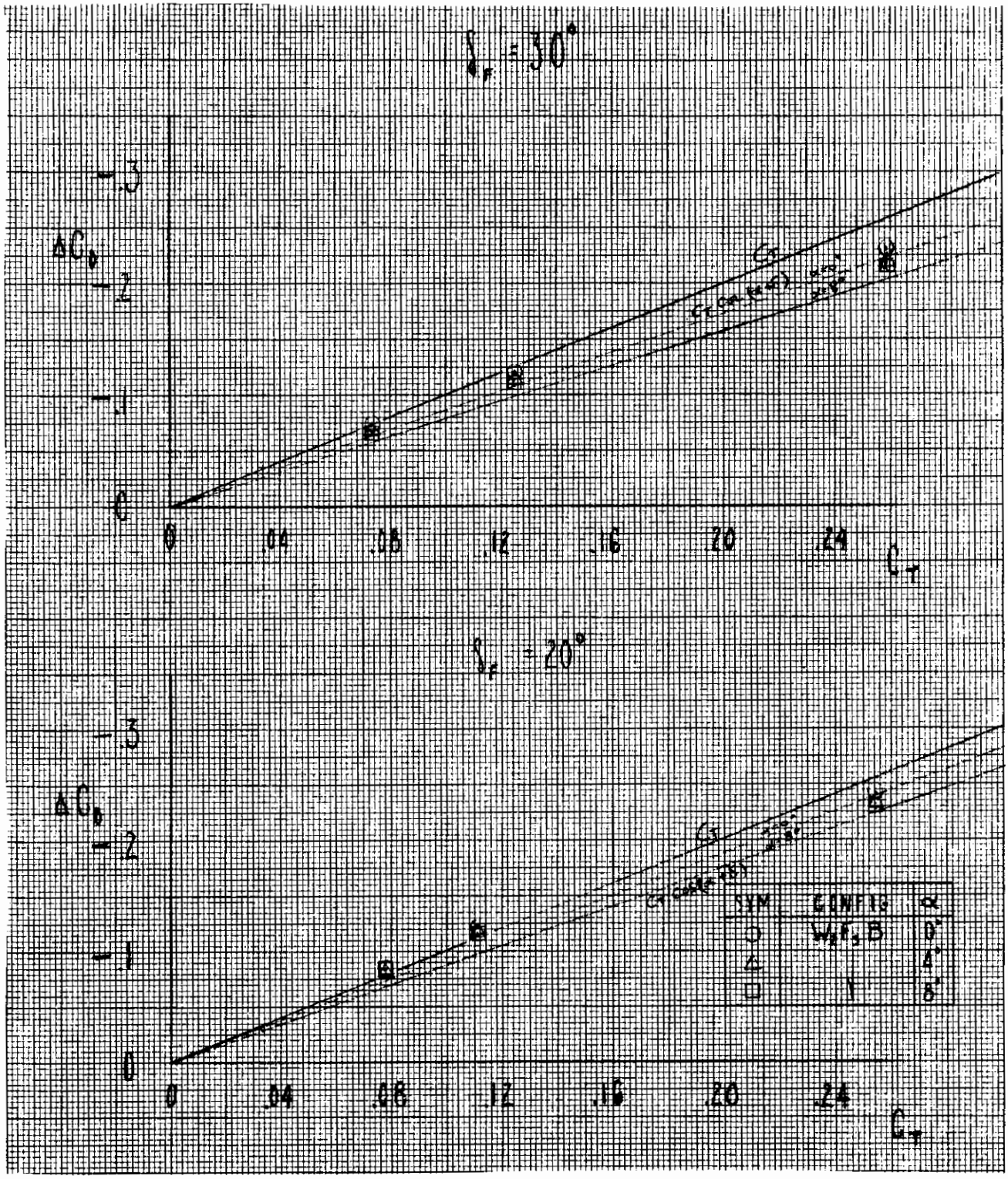

Figure 33. Effective thrust recovery (F_3) constant alpha.

DESIGN EFFECTS

LONGITUDINAL

Model Buildup

A summary of the longitudinal characteristics of all configurations fested is presented in Table 2. The moment slopes and intercepts, as well as the abso absolute values of canard and horizontal tail moment buildup are a function of CG position for the configuration being analyzed. The results from this test used the quarter chord point of the MAC to resolve moments. For analysis of like results, this is very proper, but when these results are identified to a specific air vehicle design tail arms must be recognized and adjustments made. Table 2 slope values are applicable only in the linear slope range. Although the angle of linearity varies, it generally holds until α = 8 degrees for lift slope ($C_{L\alpha}$) and α = 5 degrees for moment slope (dC_M/dC_L). The aerodynamic center is not a function of center of gravity since AC = CG - $\frac{dC_M}{dC_L}$; where CG = 0.25 percent MAC for the wind tunnel model and also is reflective of the linear portion of the stability variation.

Model component buildup plots are presented in Figures 34 through 37 for the base configuration only.

Figure 34 and 35 presents the lift and moment characteristics as each component is added unto the wing body. By obtaining the net difference between component on and off, a comparison can be made with other components, as well as a variation of incremental lift and moment with angle of attack. Maximum life coefficient extends beyond the test range of 28 degrees. The increase in drag coefficient at low angles of attack as tail and canard are added is presented in Figure 36. However, the drag due to lift is lower, with the canard offsetting the increased friction drag and thus producing less total drag above C_L = 0.45. Axial chord force, as shown in Figure 37, displays a marked change when the canard was added. This results from canard interaction with the wing at angles between 10 and 16 degrees, as indicated by reversal of the chord force. This effect is the result of the high canard loading when in the presence of the wing and the sharp leading edge of this part, and further indicates that canard section design will require a large leading edge radius and possibly leading edge camber to delay this effect to higher angles.

Located on Figure 38 is a planform view of the model indicating areas of approximate disturbed flow as interpreted from the tuft runs. Reviewing this figure in conjunction with the C_L/C_M and C_{L_α} plots indicate that the wingtip is lightly loaded, approaching an angle of attack of 4 degrees and is possibly separated above the angle. The outer wing panel appears to separate as the angle of attack increases to 10 degrees, whereby there is

TABLE 2. LONGITUDINAL CHARACTERISTICS SUMMARY

Configuration	C_{L_o}	C_{L_α}	$C_{m_{\alpha=0}}$	d_{C_m}/d_{C_L}	AC	$C_{D_{MIN}}$
WB	0.135	0.0584	-0.060	0	0.25	0.0218
WBC_5	0.12	0.060	-0.175	0.50	-0.25	0.0256
WBC_5H_6	0.12	0.067	-0.16	0.35	-0.10	0.0296
WBH_6	0.12	0.067	-0.062	-0.144	0.394	0.02525
WBC_6	0.12	0.060	-0.137	0.32	-0.07	0.0248
WBC_6H_6	0.115	0.067	-0.08	0.090	0.16	0.0282
WBC_7	0.135	0.060	-0.088	0.29	-0.04	0.0265
WBC_7H_6	0.11	0.0666	-0.10	0.30	-0.05	0.0305
WBC_8H_6	0.11	0.0666	-0.10	0.335	-0.085	0.030
W_2B	0.135	0.0584	-0.06	-0.02	0.27	0.0208
W_2BC_5	0.12	0.060	-0.12	0.576	-0.326	0.0255
$W_2BC_5H_6$	0.12	0.067	-0.12	0.45	-0.20	0.0295
W_6B	0.135	0.0584	-0.060	0	0.25	0.022
W_6BC_5	0.135	0.065	-0.12	0.576	-0.326	0.0270
$W_6BC_5H_6$	0.17	0.067	-0.106	0.476	-0.226	0.030
WBC_1H_1	0.125	0.066	-0.082	0.15	0.10	0.0240

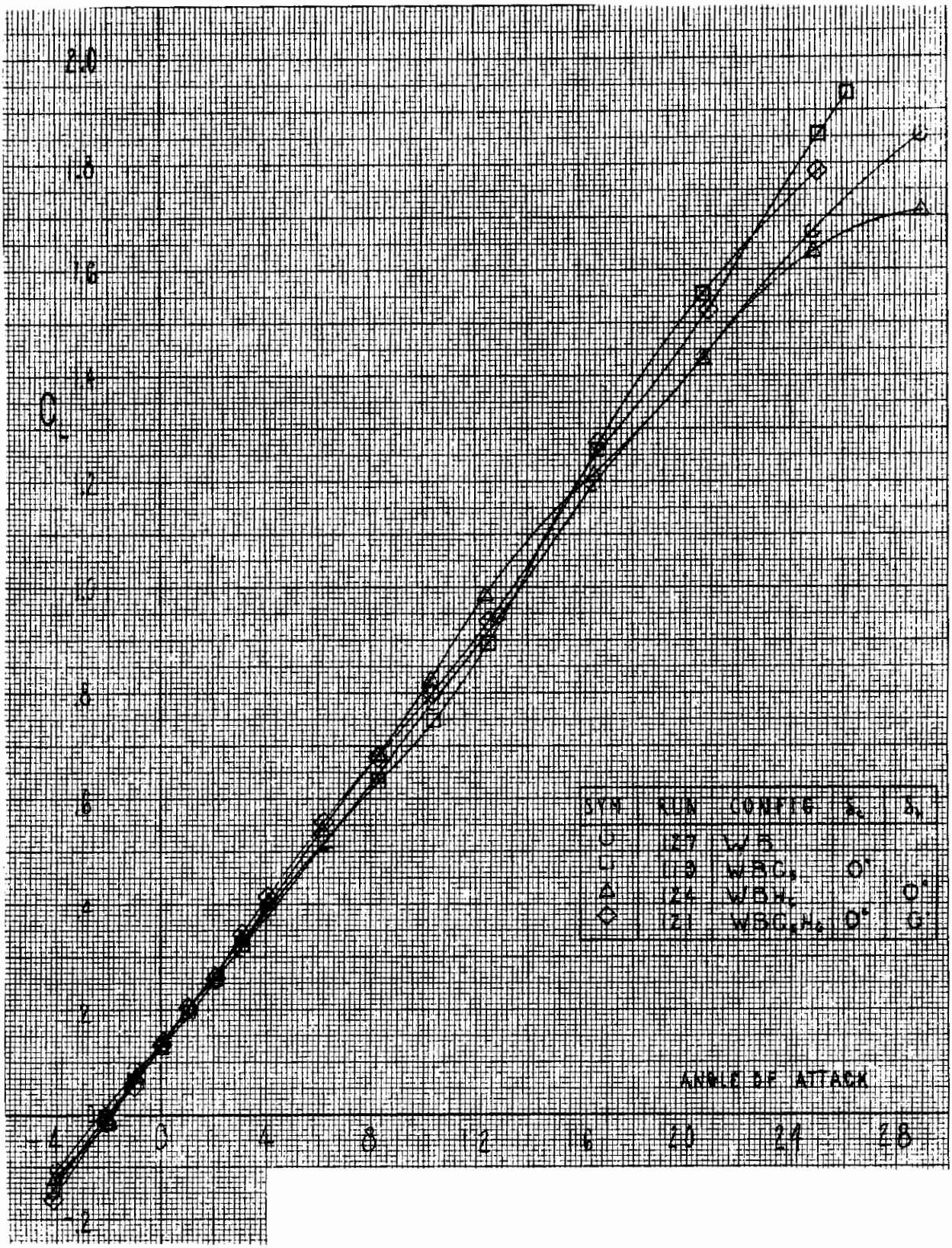

Figure 34. Model buildup in lift coefficient.

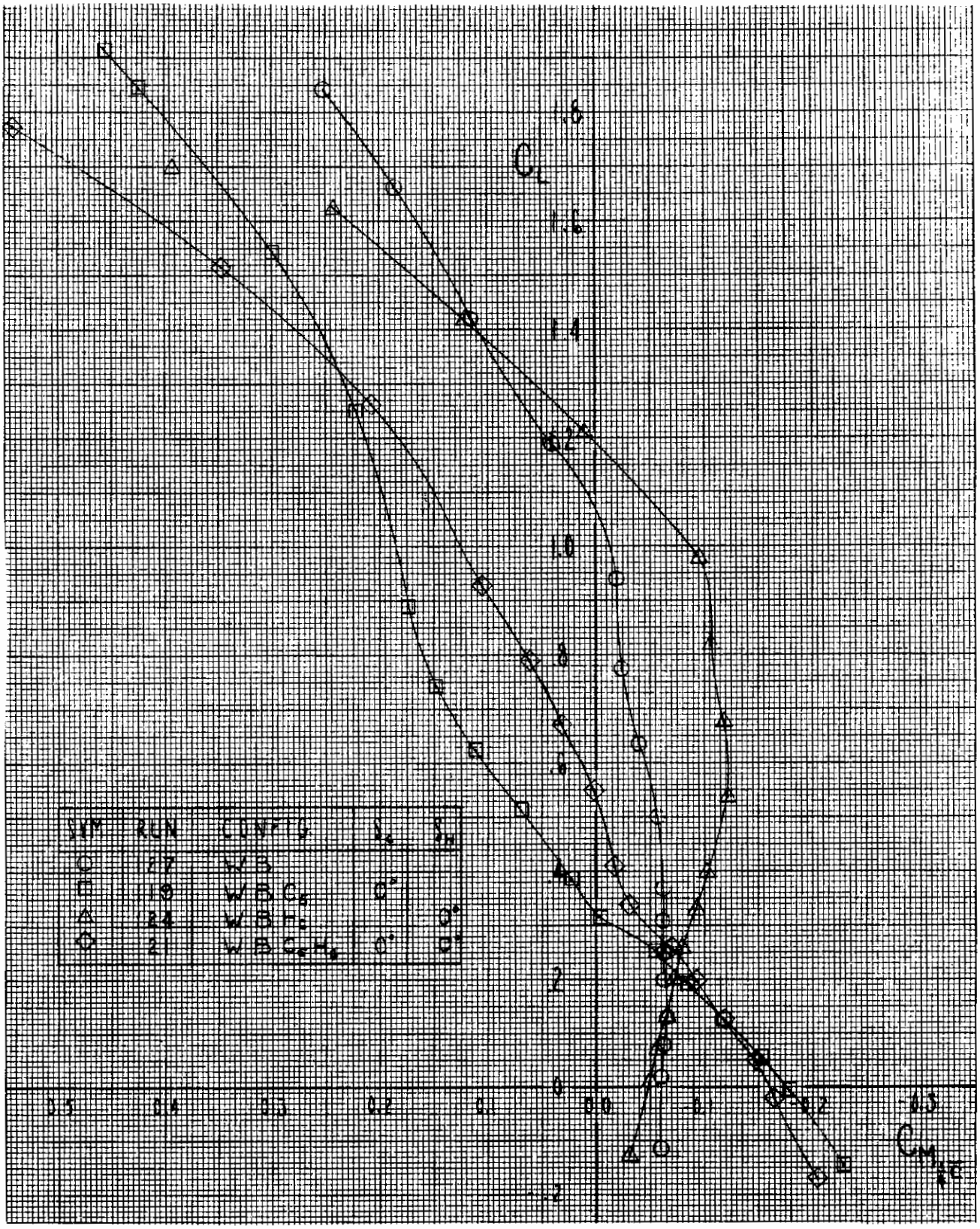

Figure 35. Model buildup in moment coefficient.

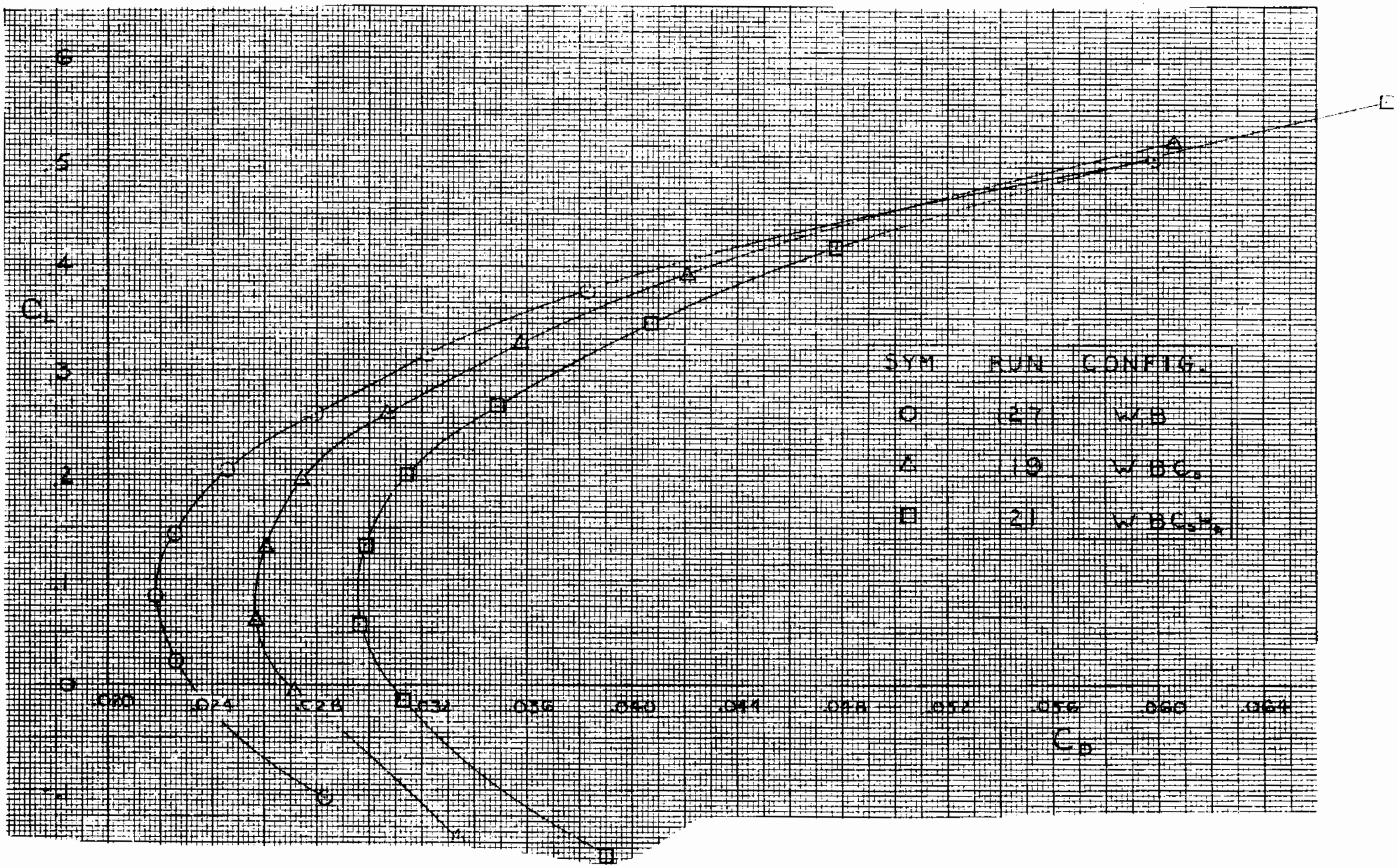

Figure 36. Drag buildup.

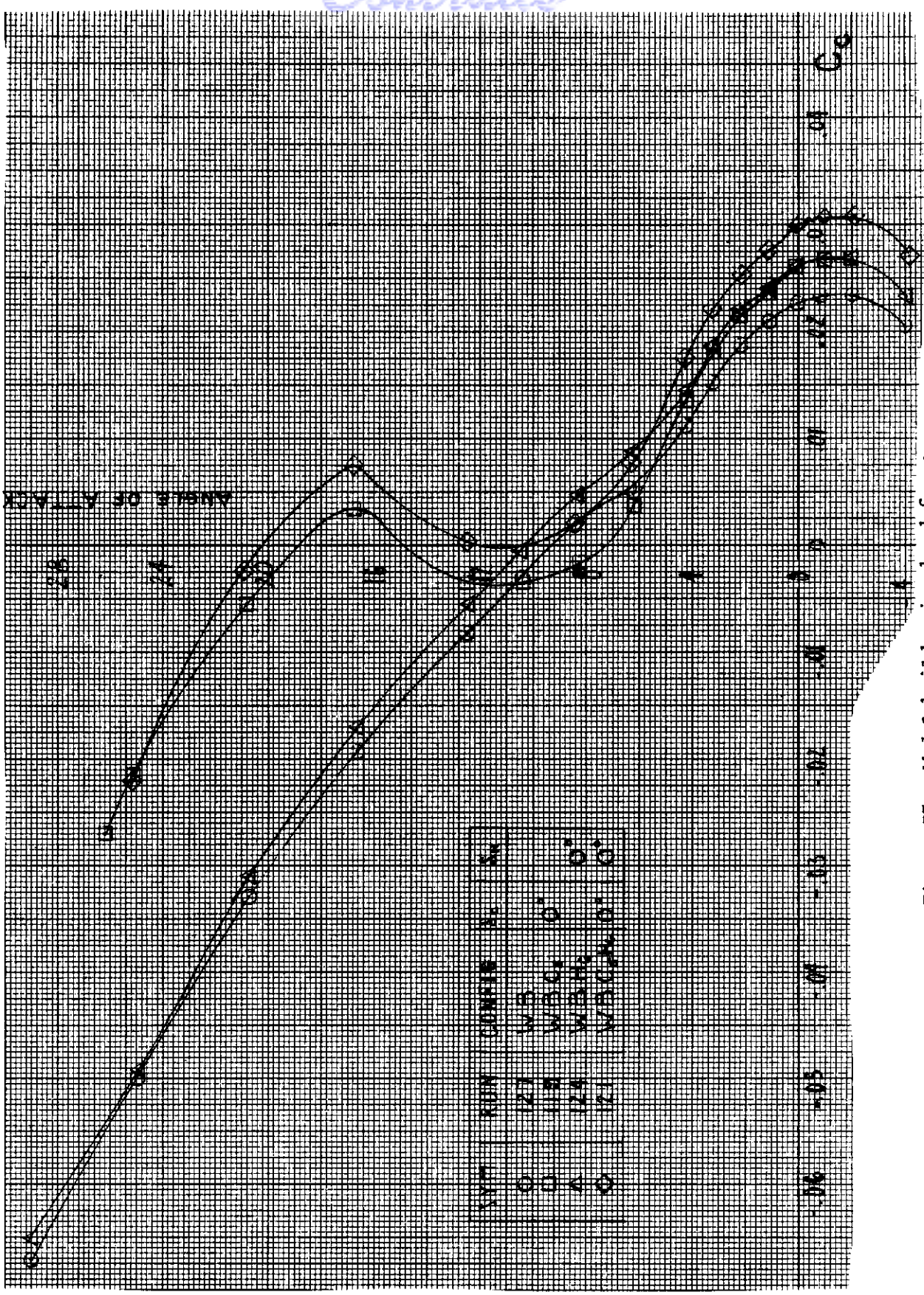
C_c
.04
.02
0
-.02
-.04
-.06
-.08
-.10
ANGLE OF ATTACK
-4°
0°
4°
8°
12°
16°
20°
24°
28°
32°
36°
40°
44°
48°
52°
56°
60°
64°
68°
72°
76°
80°
84°
88°
92°
96°
100°
104°
108°
112°
116°
120°
124°
128°
132°
136°
140°
144°
148°
152°
156°

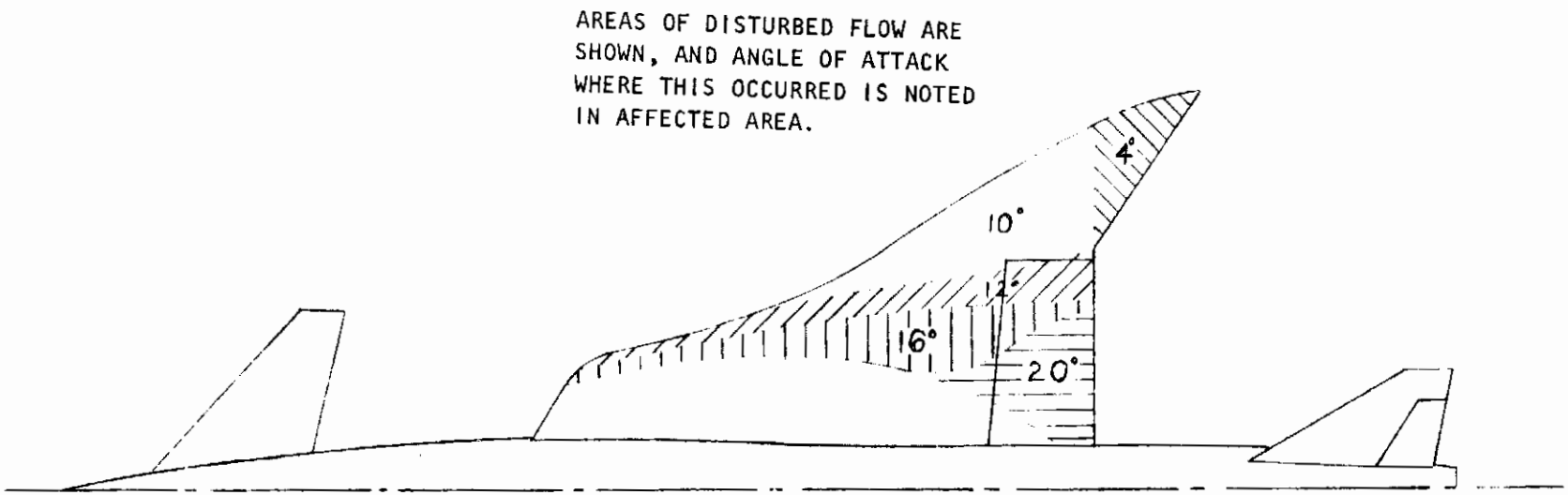

Figure 38. Sketch of tuft reactions.

a loss in stability and in C_{L_α}. At approximately an angle of attack of 12 degrees, the aerodynamic data and the tuft run indicated that a vortex was being generated at the wing leading edge crank causing an increase in C_{L_α}. As the angle of attack increases from 16 degrees to 20 degrees, the vortex lifts off the wing panel yielding a slight loss in C_{L_α} and no change in the stability level. Above an angle of attack of 20 degrees, the C_{L_α} remains approximately a constant with a continuing loss in the stability level due to the center of pressure shifting forward. An analysis of the tuft runs also indicated that, if the jet flap thrust was on or off, there was not an apparent substantial change in the flow characteristics about the model as indicated by this visual flow method.

The lift curve slope and aerodynamic center results for the base configuration are shown in Figure 39 compared to the aero prediction program. This analysis tool uses the unified vortex lattice lifting surface theory to present a linearized potential flow solution of various input configurations. As noted on Figure 39, comparison shows reasonable results. The reason the AC results show a range of values is due to the nonlinearity of the test data permitting a degree of judgment in determining this slope.

Each control surface provides an increment to the overall stability of the aircraft model. By comparing various control surfaces, it becomes possible to adjust them such that the stability requirements can be satisfied. Moment data are presented in increment form and are not a function of data reduction CG.

The stability contribution of the canard surfaces varies with angle of attack beyond $\alpha = 4$ degrees, as shown in Figure 40. Stability increment in the forward canard position is nearly proportional to the canard size as shown in Figure 40(a). Holding the canard area constant and varying the canard fuselage location produces a decrease of stability input with rearward movement of the canard, Figure 40(b). At approximately $\alpha = 12$ degrees, all but one canard had reached maximum moment input. The low wing, closely coupled, high canard configuration, shown in Figure 41(a), however, continues to contribute increasing moment increment up to $\alpha = 17$ degrees. Since the model was inverted, the C_{M_α} curve was adjusted to reflect the change from negative to positive wing camber. Closely coupled canards on the top and bottom of the wing are compared in Figure 41(b). In the linear range ($\alpha \leq 8$ degrees), the low canard provides greater stability input. However, the high canard does have dihedral and a slightly shorter moment arm. The effect of wing hood on the base configuration does not indicate any significant difference (Figure 42). The vertical location of the wing on the fuselage (W_6) produces greater canard stability input for this canard wing relationship. This agrees with previously discussed results which indicate that large vertical separation of canard and wing extends the range of the input moment.

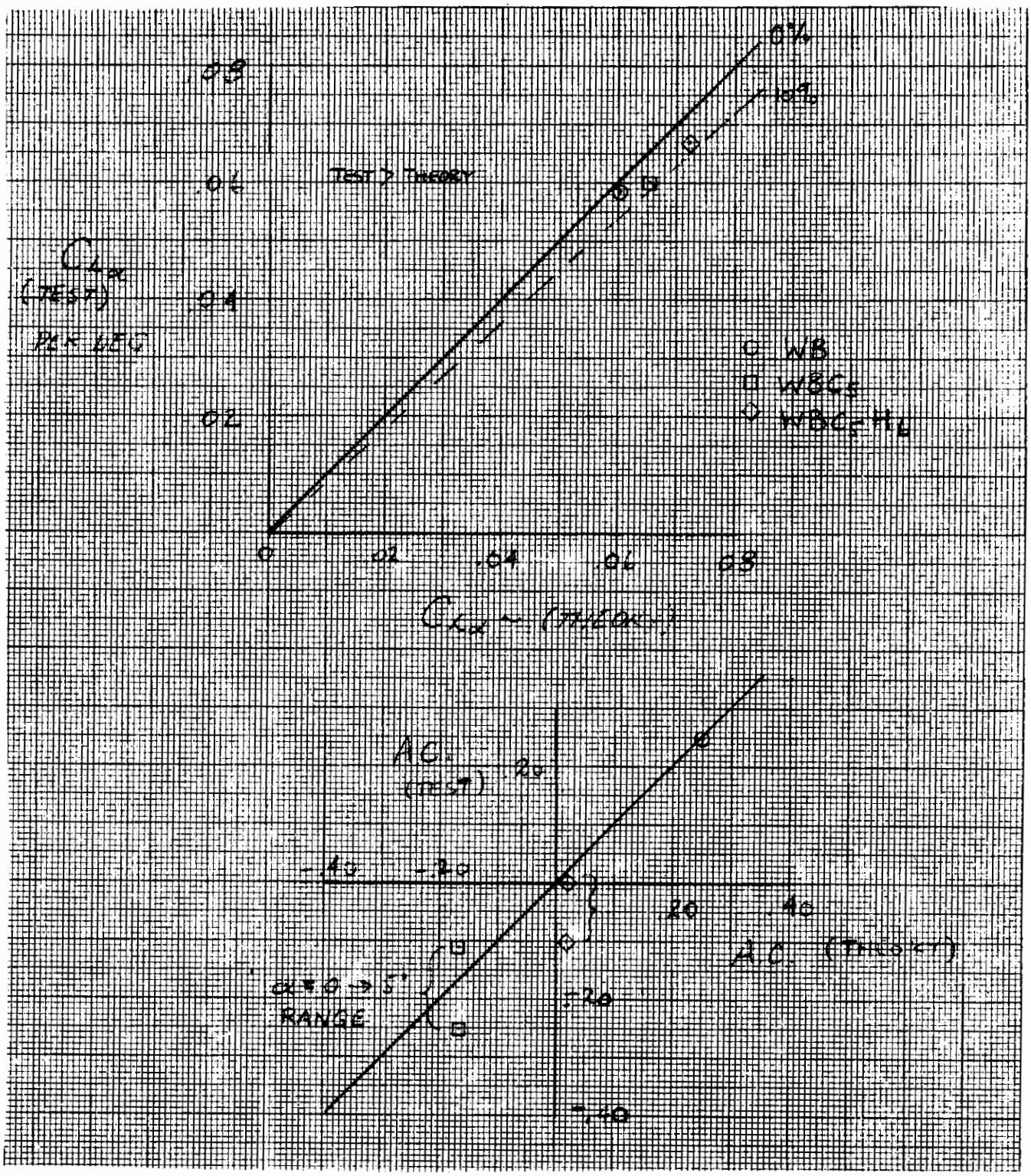

Figure 39. Comparison of prediction program with NAAL 707 test data.

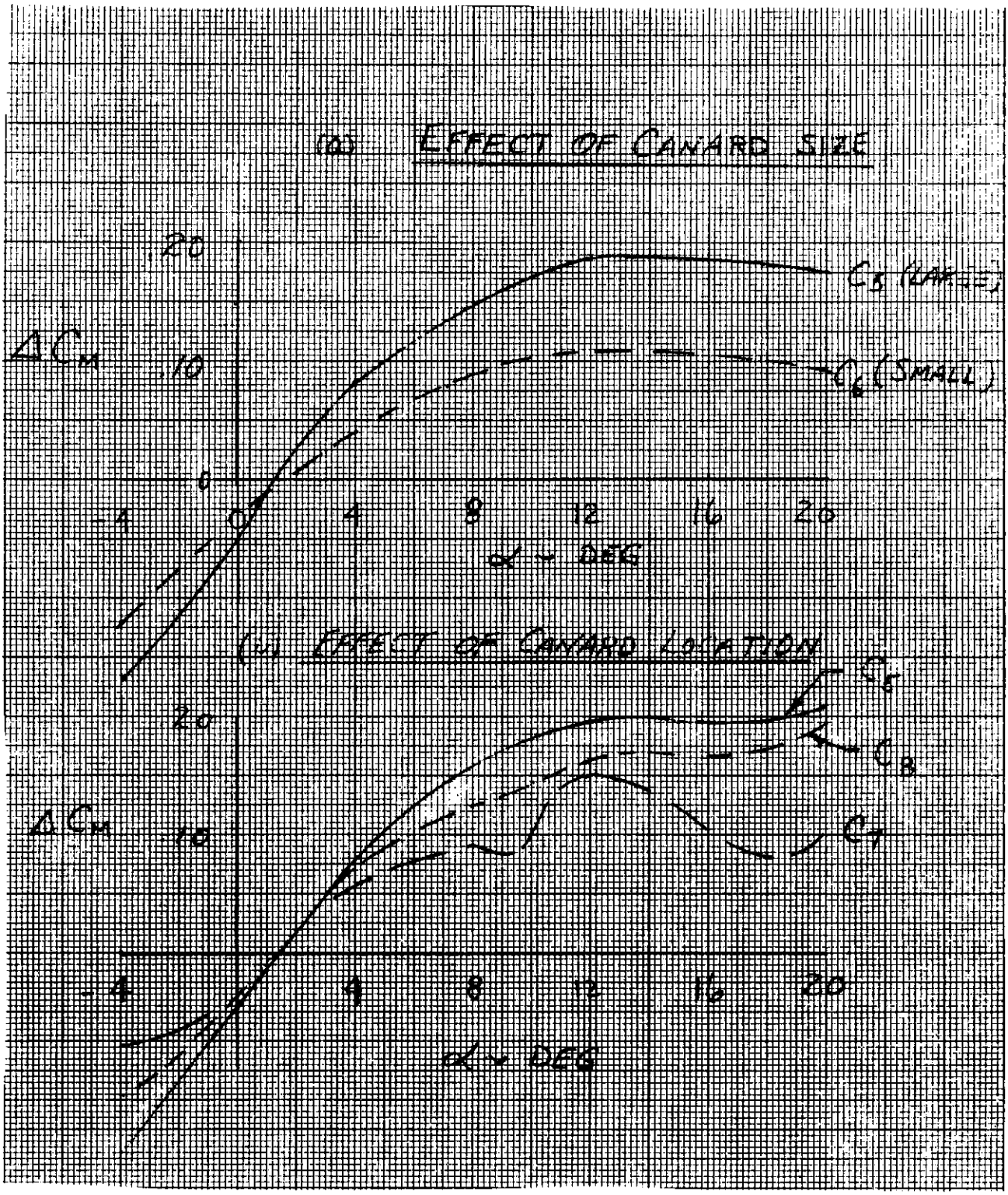

Figure 40. Canard stability input.

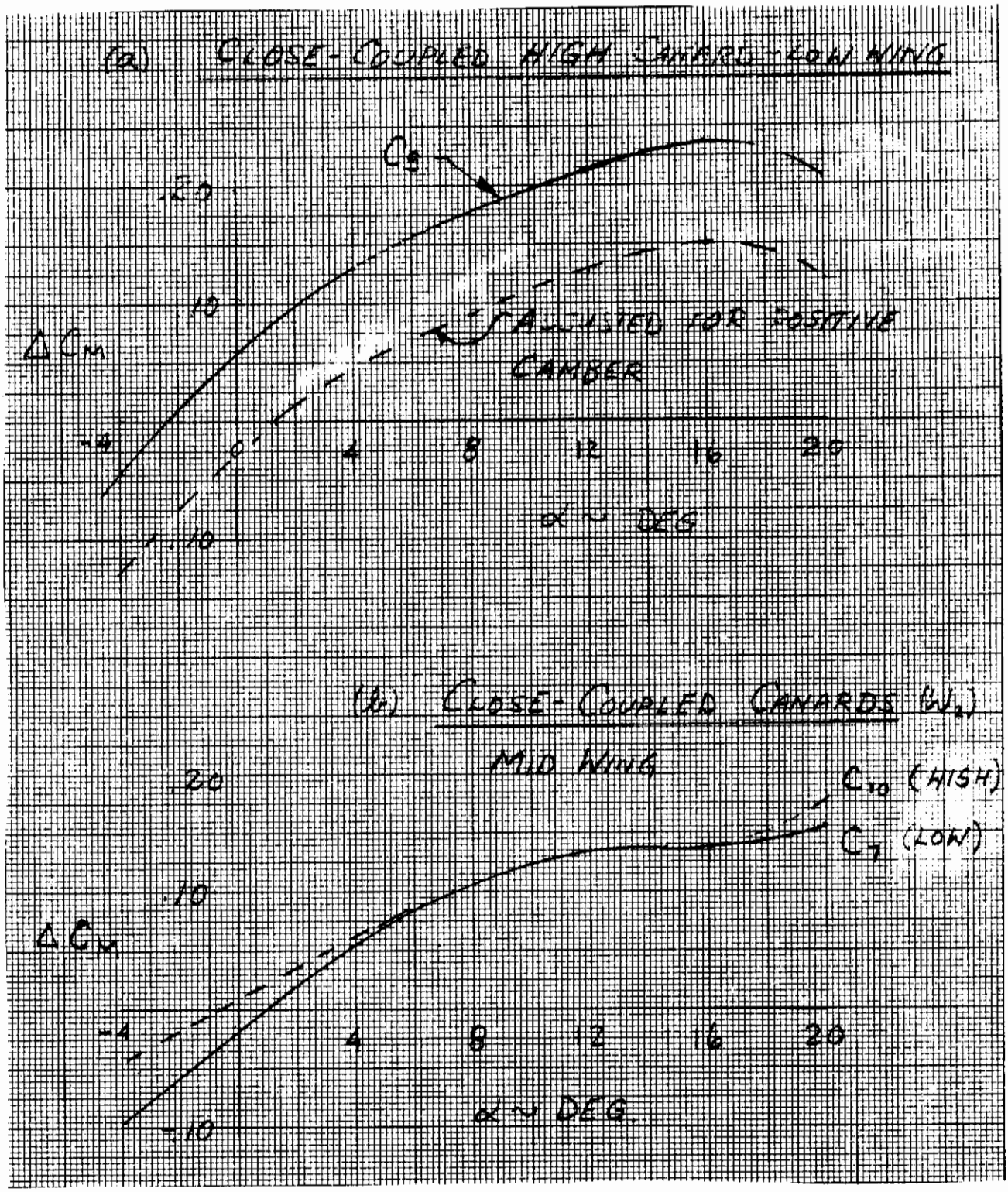

Figure 41. Canard stability input.

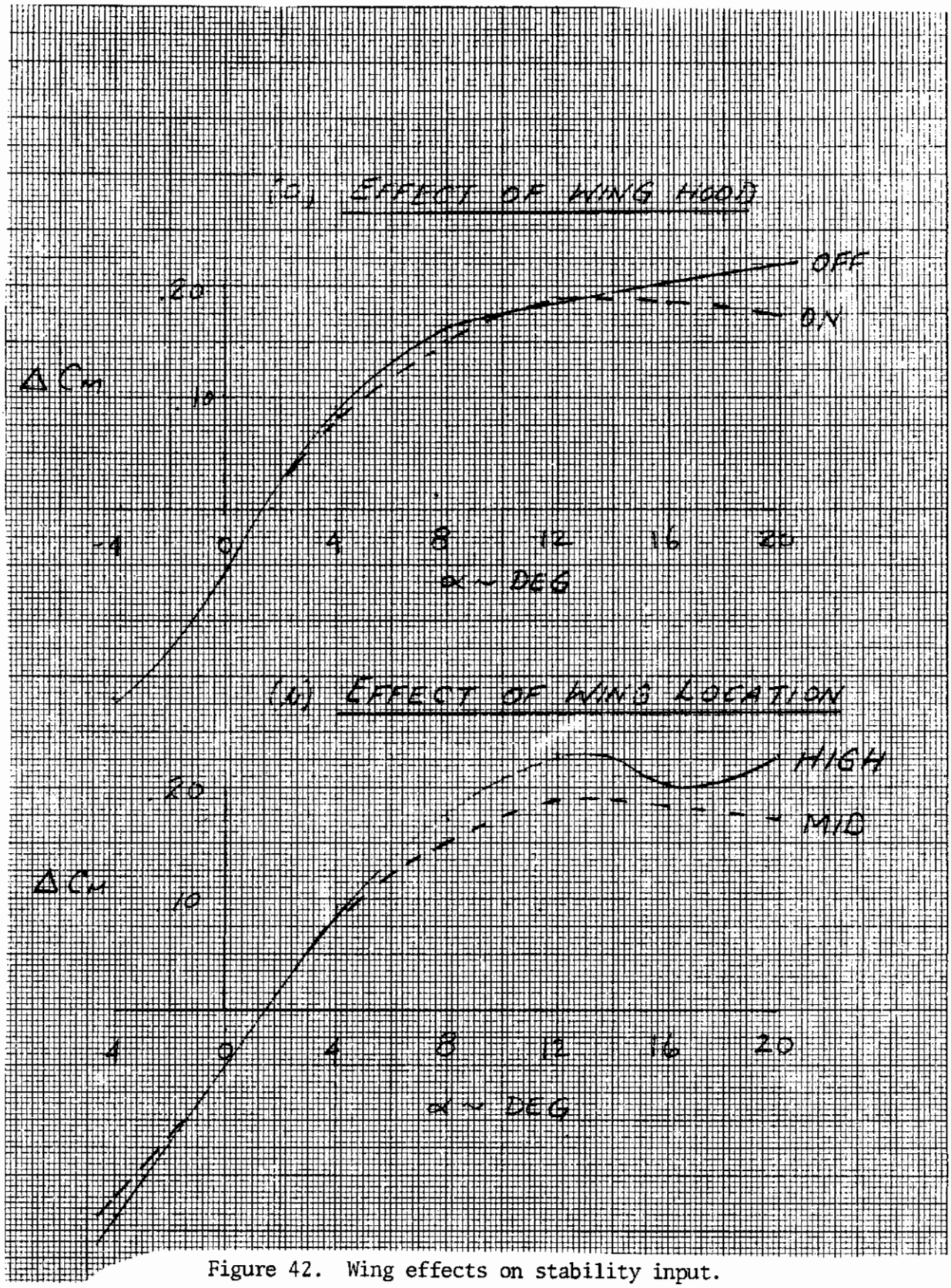

Figure 42. Wing effects on stability input.

Surface Effectiveness

A major objective of the test program was to compare the low-speed effectiveness of all the control surfaces by varying the size, shape, and location of each one. Of primary concern was the effect of the canard in the presence of the wing. Three different canards were tested, with C_5 the larger area, being identified as the base configuration.

Figures 43, 44, and 45 present the lift and moment increments due to surface deflection (effectiveness) of canards C_1, C_5, C_6, respectively. All the canards display a loss of effectiveness with increased angle of attack due to downwash flow onto the wing and flow separation on the canard. Figure 46 clearly demonstrates the greater effectiveness (at $\alpha = 0$) of C_5 for all canard deflections, which is in a large part due to its increased surface area. Beyond an angle of attack of approximately 8 degrees, all three canards begin to produce a negative lift increment. This would indicate that canard size and shape are relatively unimportant in maintaining pitching moment at higher angles of attack. The downwash field behind the canard at high angles creates a loss of net lift and a smaller, but still favorable, coupled pitching moment. However, at angles higher than 12 degrees, the surface begins to stall and the moment increment decreases rapidly. This conclusion also generally holds true when the canard is deflected to high angles. There is a loss of effectiveness due to the increase effective angle between the canard and wing. However, the loss is not directly proportional to this angle, indicating an interaction between canard/wing coupling and loss of lift on the canard. Reducing the distance between the canard and wing (C_8) does not significantly alter the previously discussed loss of effectiveness (Figure 47). However, positioning the canard closely coupled abouve the wing produces a significantly more uniform and constant effectiveness with increasing angles of attack (figure 48). This result agrees with unpublished NASA data for similarly located canards. Test data show that the pitching moment increment due to canard deflection is initially lower for the close-coupled high canard, but remains fairly constant through angle of attack range.

An alternate way of viewing effectiveness is by plotting canard volume versus lift and moment increment due to canard deflection at $\alpha = 0$ (Figure 49). The results indicate that effectiveness is nearly proportional to canard volume.

Raising the wing from a mid to a high fuselage station (W_6) increases the lifting effectiveness, as seen in Figures 50 and 51 for 5 and 10 degrees, respectively. This increase is primarily due to the greater vertical separation between the wing and canard. The pitching moment, on the other hand, exhibits less effectiveness at $\delta_c = 5$ degrees than at 10 degrees, possibly due to a more favorable downwash effect at higher canard deflections.

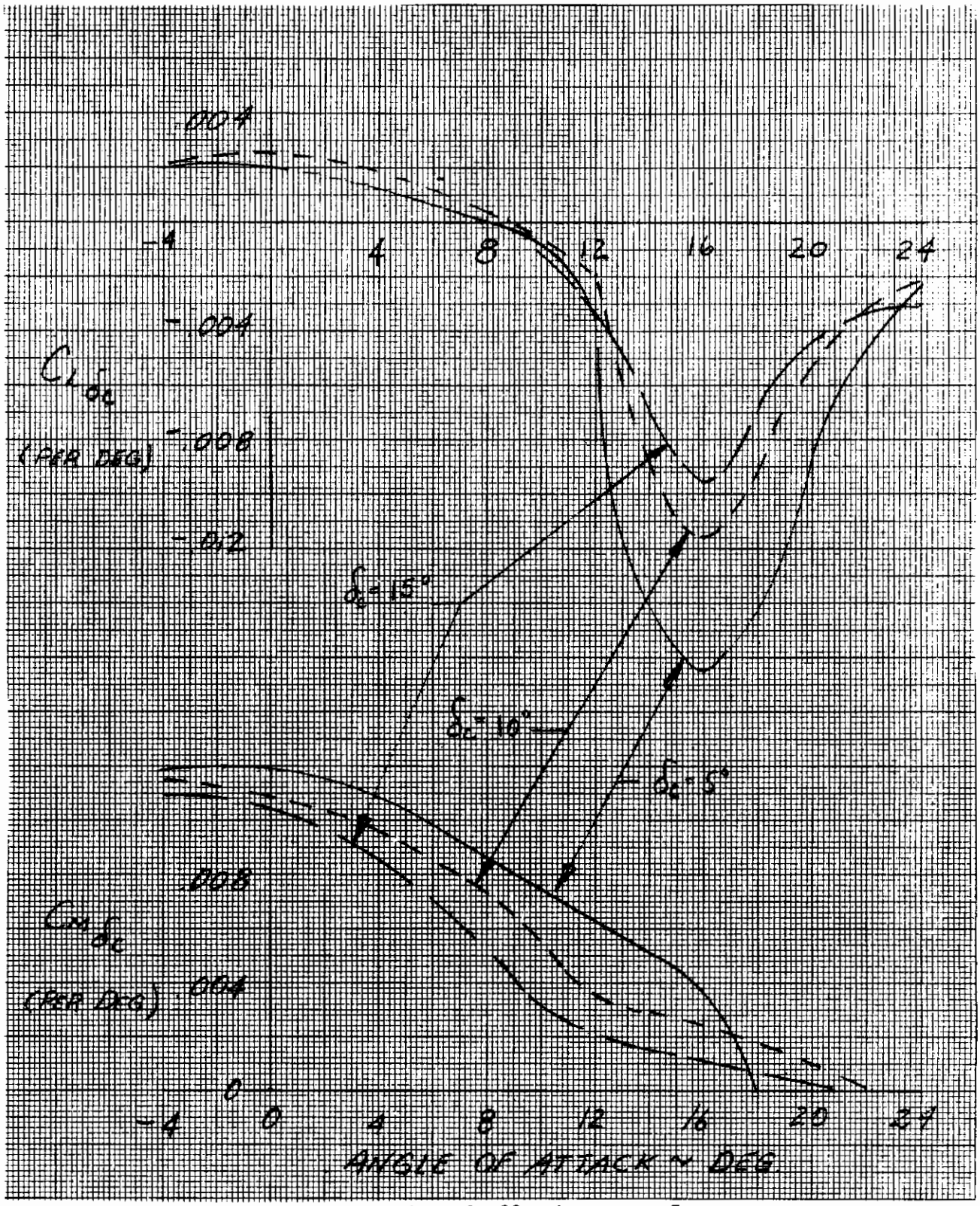

Figure 43. Canard effectiveness - C_l.

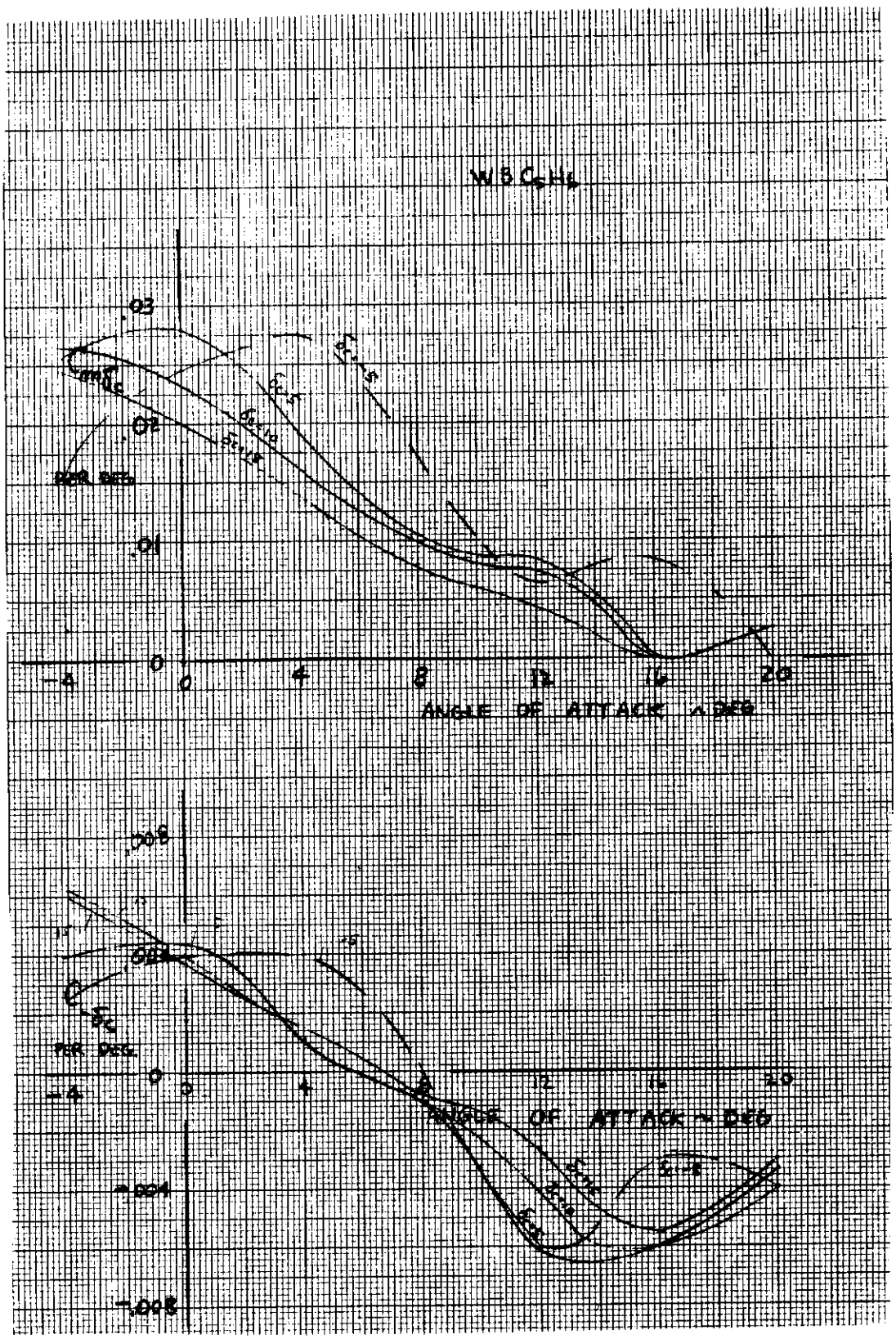

Figure 44. Canard effectiveness - C_5.

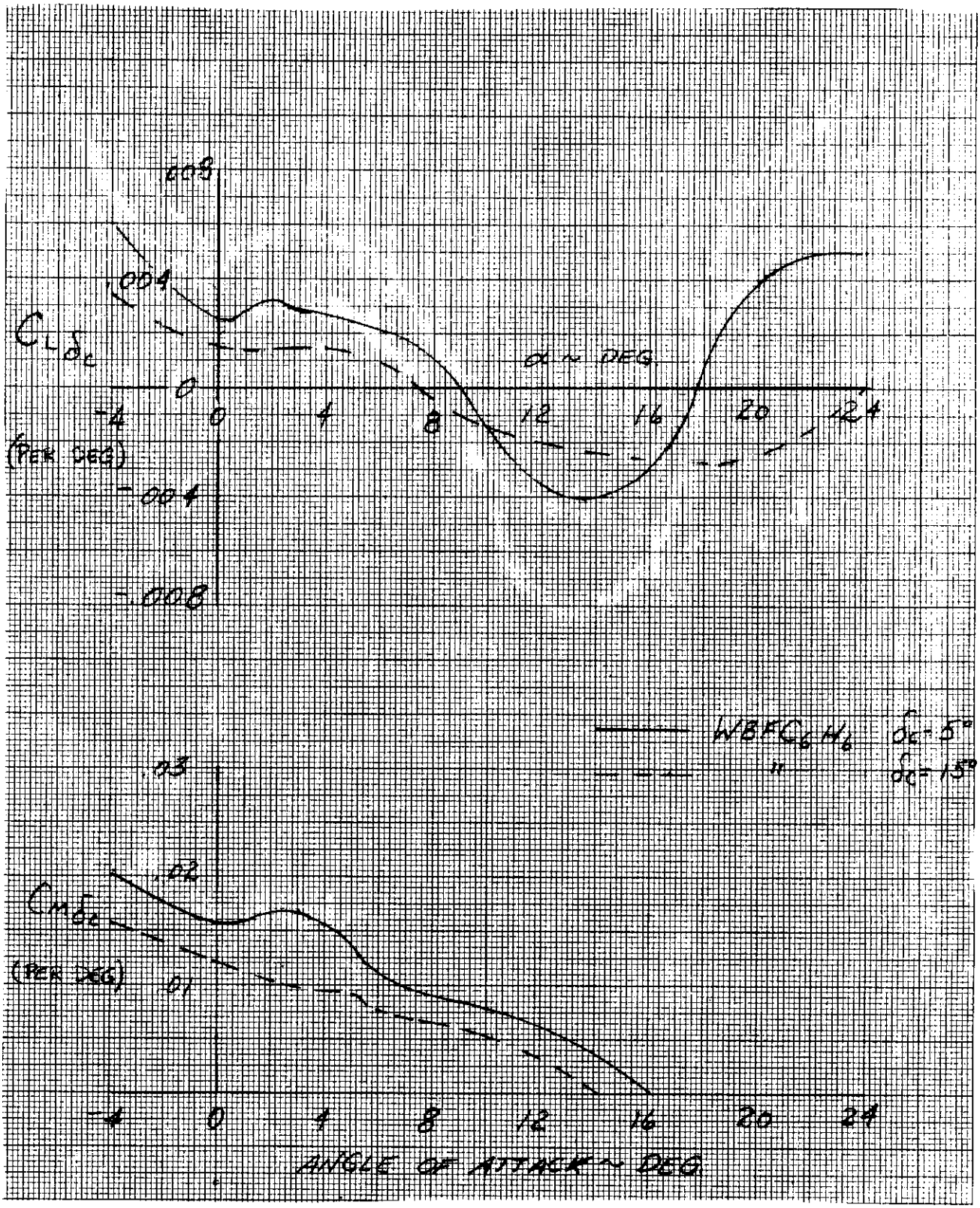

Figure 45. Canard effectiveness - C_6.

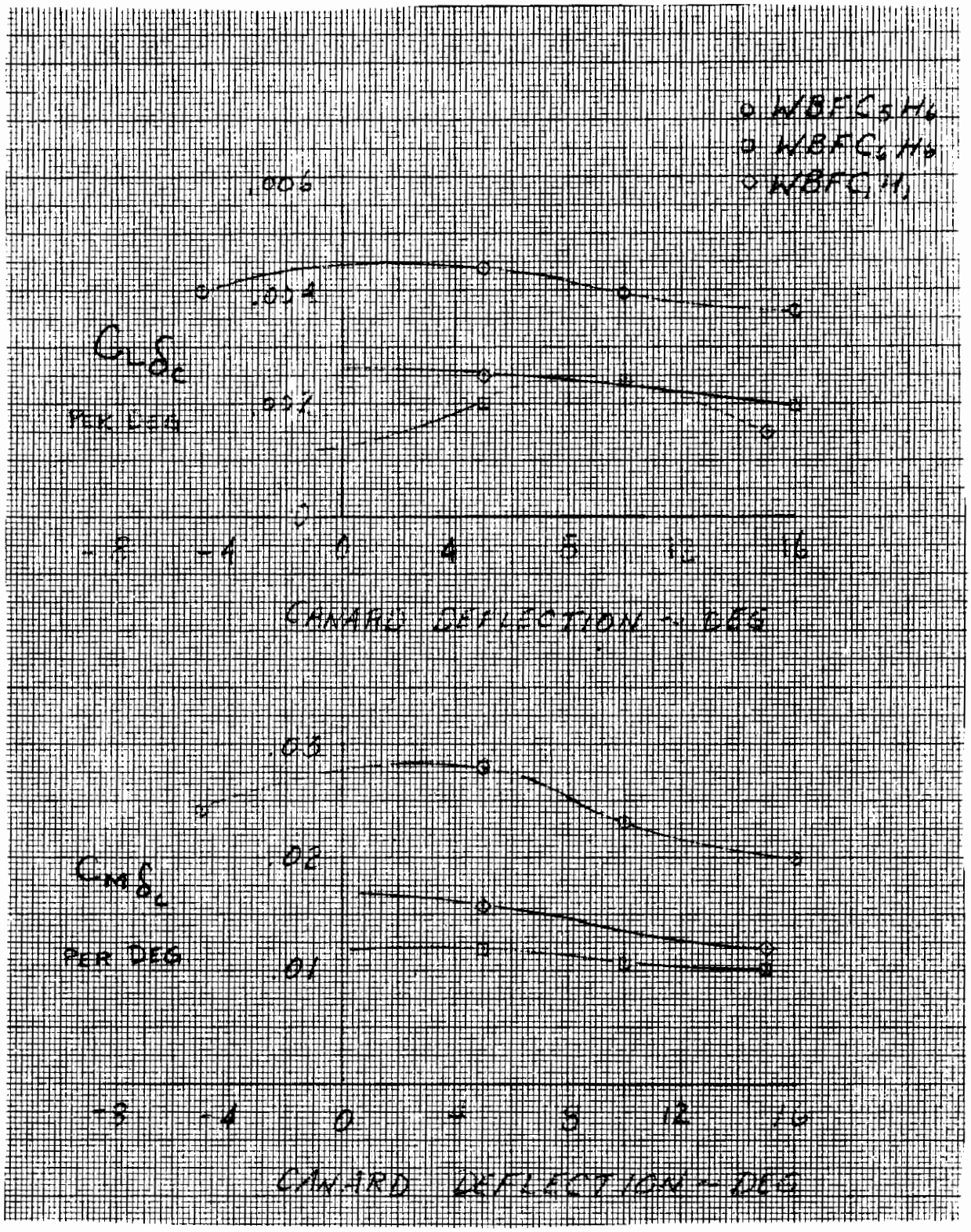

Figure 46. Forward canard effectiveness at $\alpha = 0$.

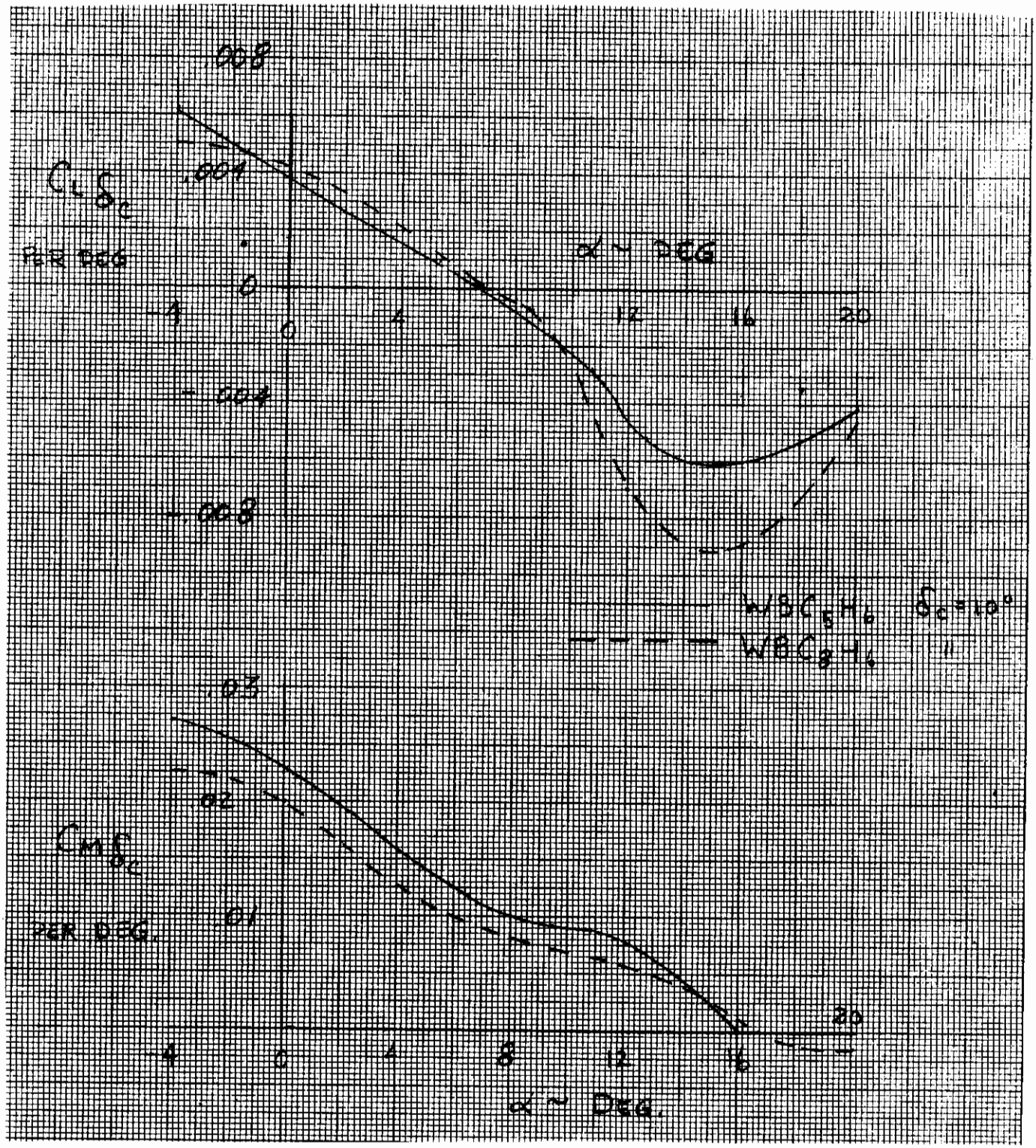

Figure 47. C_8 canard effectiveness.

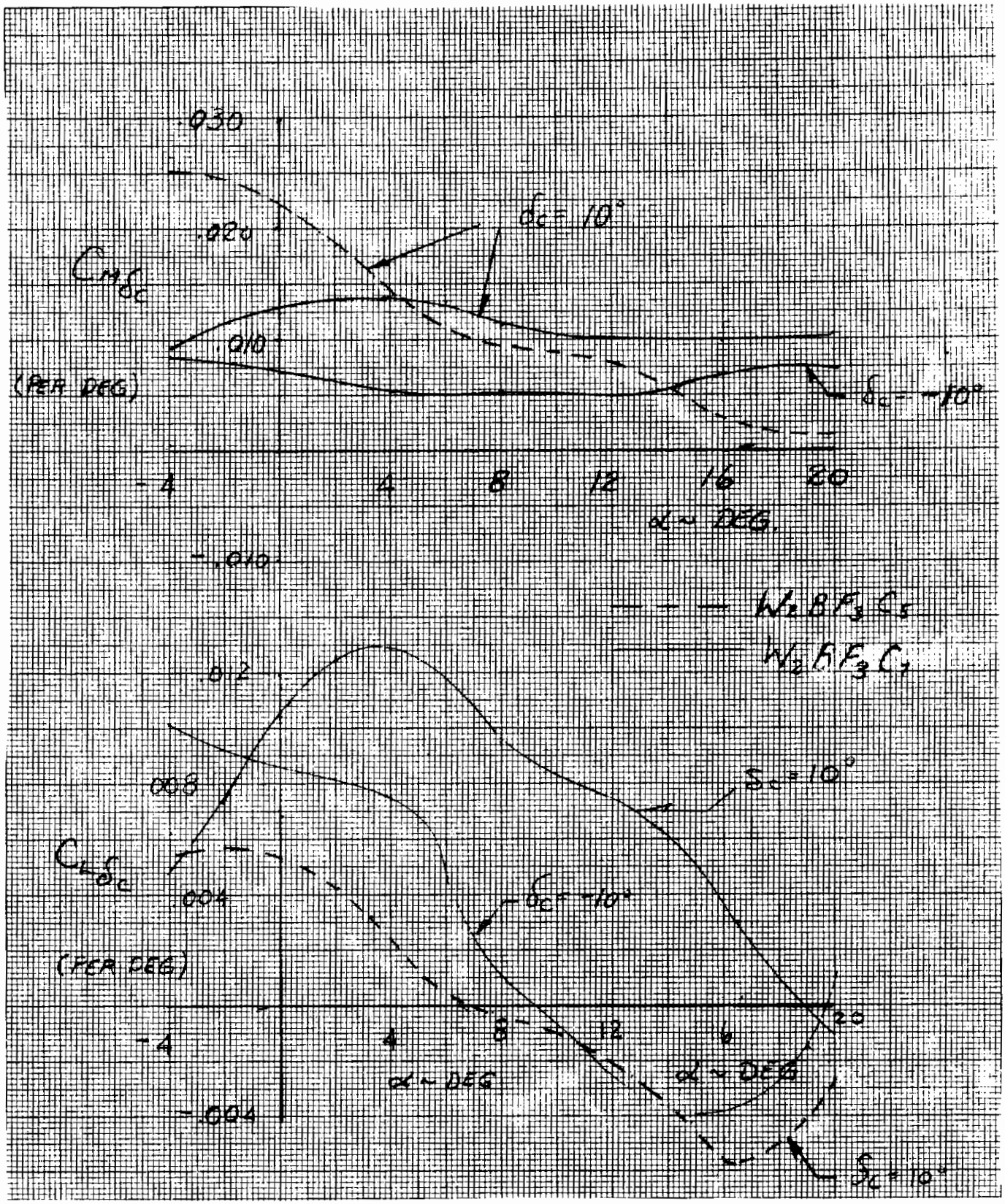

Figure 48. Close-coupled canard effectiveness.

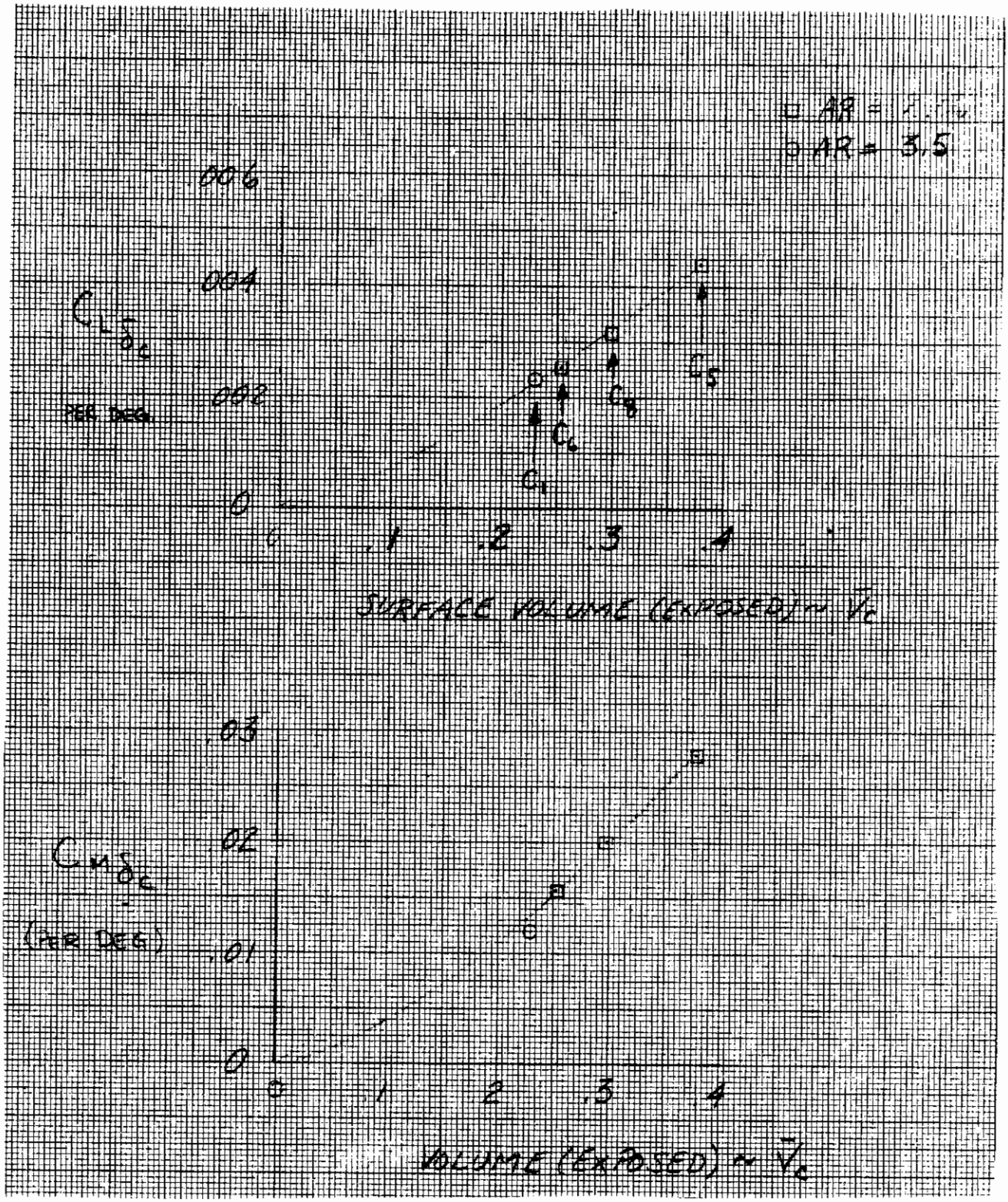

Figure 49. Effect of canard volume on surface effectiveness.

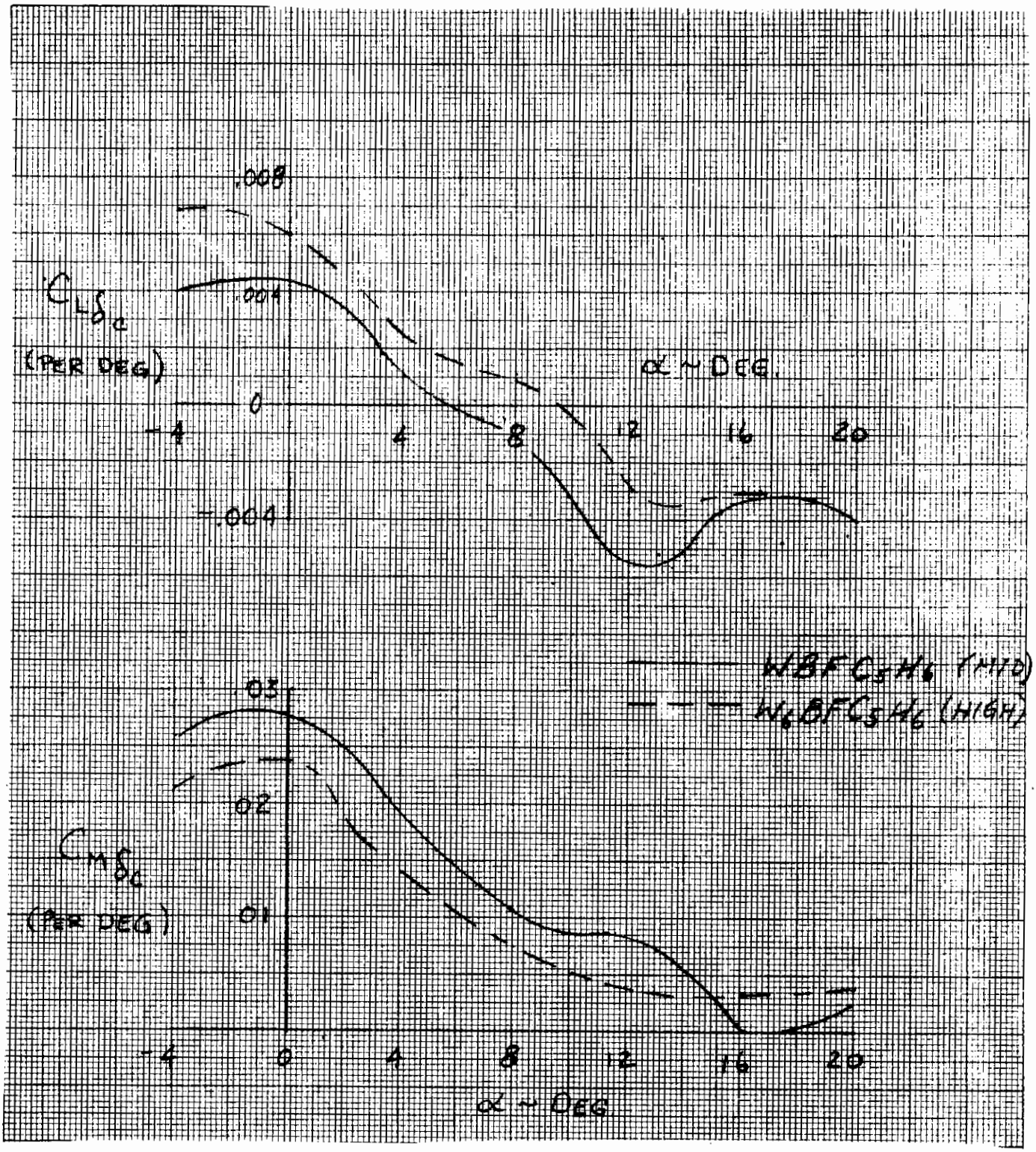

Figure 50. Effect of wing vertical position on canard effectiveness - $\delta_C = 5°$.

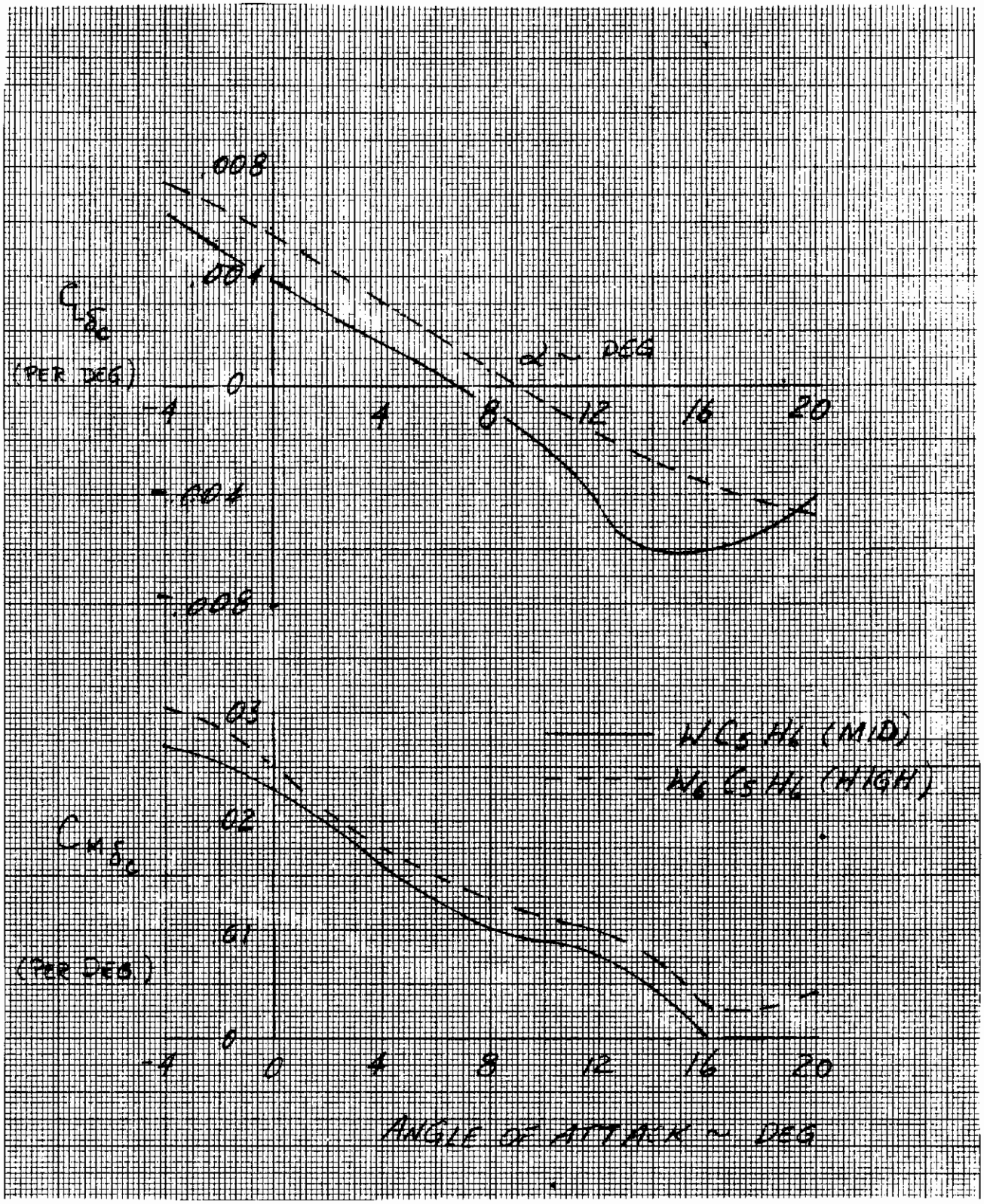

Figure 51. Effect of wing vertical position on canard effectiveness - $\delta_C = 10°$.

The effect of the wing hood on canard effectiveness at δ_C = 5 degrees is presented in Figure 52. The absence of the wing hood geometrically increases the longitudinal separation of wing-canard over the base configuration, but increases the effectiveness only slightly. Varying the deflection angle (Figure 53) produces results similar to the trends shown with wing hood on.

Analytical studies and a review of NASA test data with the canard on a spearate balance show that the canard in the presence of the wing loads to twice the canard above sectional lift. This additional loading causes the canard to stall prematurely, producing the angle-of-attack variations shown. The conclusion drawn from these results is that, for a canard to operate in the wing flow field, it must be designed (cambered) to carry this loading.

The effectiveness of the aft V-tail, as shown in Figure 54, demonstrates that there is not loss of effectiveness with increased angle of attack as was the case with the canards. Effectiveness versus aft tail deflection is presented in Figure 55. The effect of the wing vertical position on the tail effectiveness is presented in Figure 56.

Modifying the body nose shape (Figure 4) to prevent the unporting of the canard at higher surface deflections was investigated throughout the angle-of-attack range. Effectiveness results show little or no change due to sealing the open space between the inboard canard chord and the body for deflections of 10 and 15 degrees.

Also of interest in the surface effectiveness analysis is the influence of jet flap flow. Figures 5 and 58 display the lift and moment surface effectiveness per degree as effected by power for the canard and aft tail surface deflections, respectively. The canard shows an increase in moment effectiveness with jet on (P_T/P_O = 1.5) at 10-degree flap deflection. The moment increase is maintained to angles beyond 20 degrees despite the large net loss in lift increment at high angles of attack. It may thus be concluded that greater negative lift is experienced on the wing, which in turn, produces greater coupling moments. However, the diminishing moment increment trend, due to canard stalling, is still present. The aft tail, on the other hand, exhibits some loss of effectiveness with jet thrust, but remains fairly constant with increasing angle of attack. This is most likely due to a stronger downwash field created by the jet.

Flap effectiveness is examined for two flap areas as shown in Figure 59. Results indicate that F_3 (twice the surface area of F_1) is twice as effective. With no jet flap blowing, the flap (F_3) loses effectiveness beyond δ_F = 20 degrees due to stall. Adding the canard and horizontal tail (Figure 60) reveals that the influence of the canard on the flow over the wing reduces flap effectiveness with increasing angle of attack.

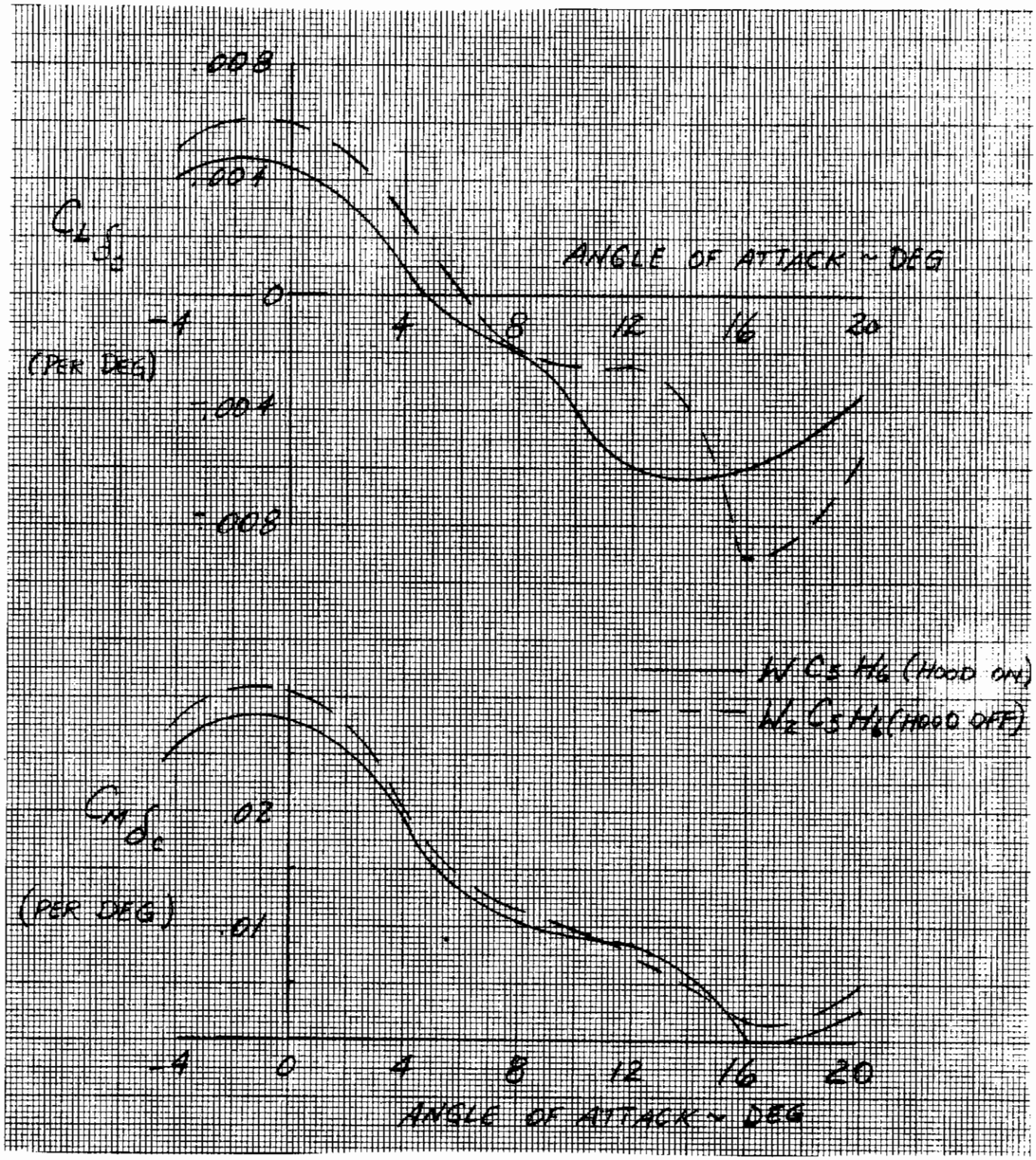

Figure 52. Effect of wing hood on canard effectiveness - δ_C = 5°.

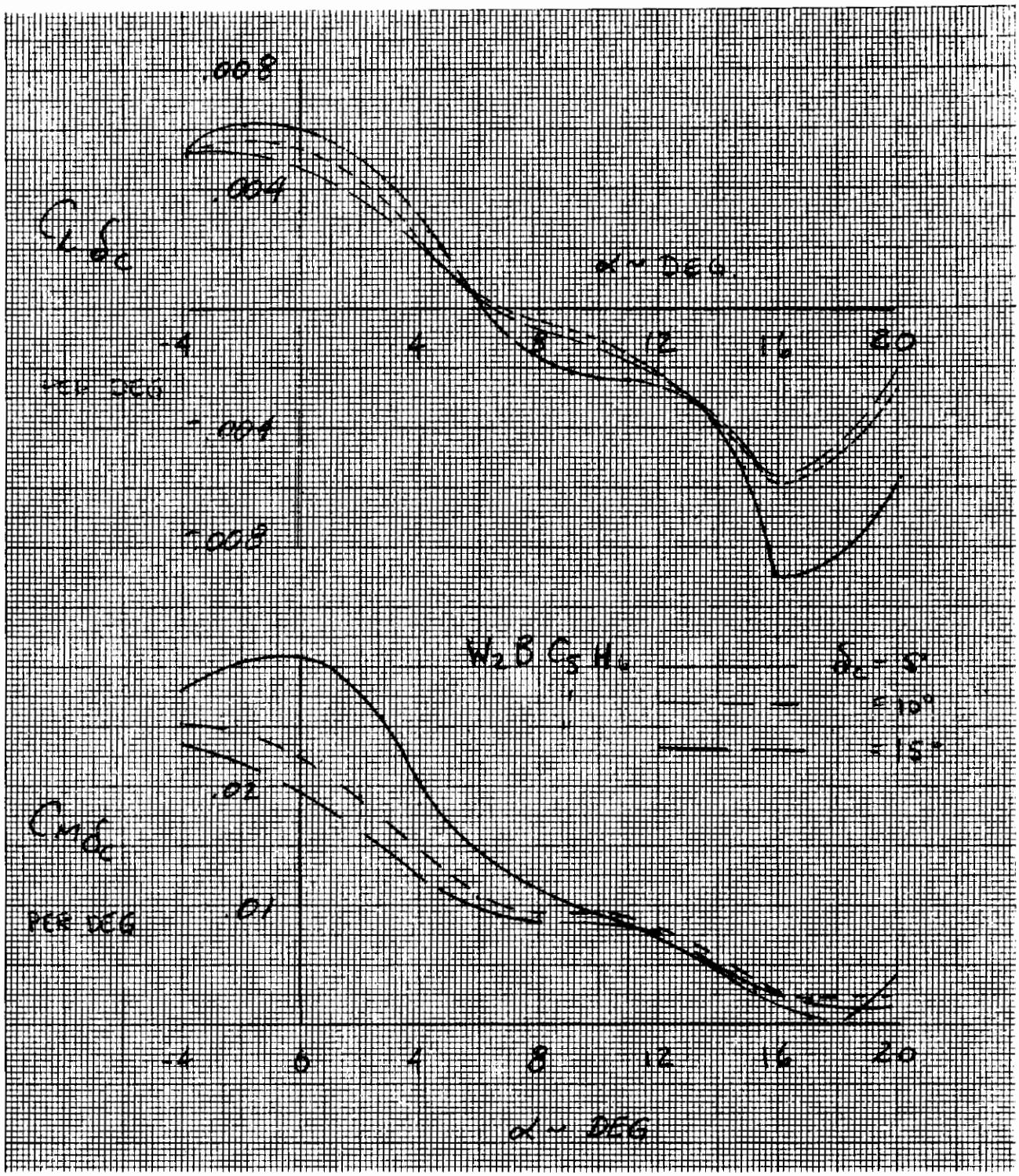

Figure 53. Canard effectiveness - W_2 Wing.

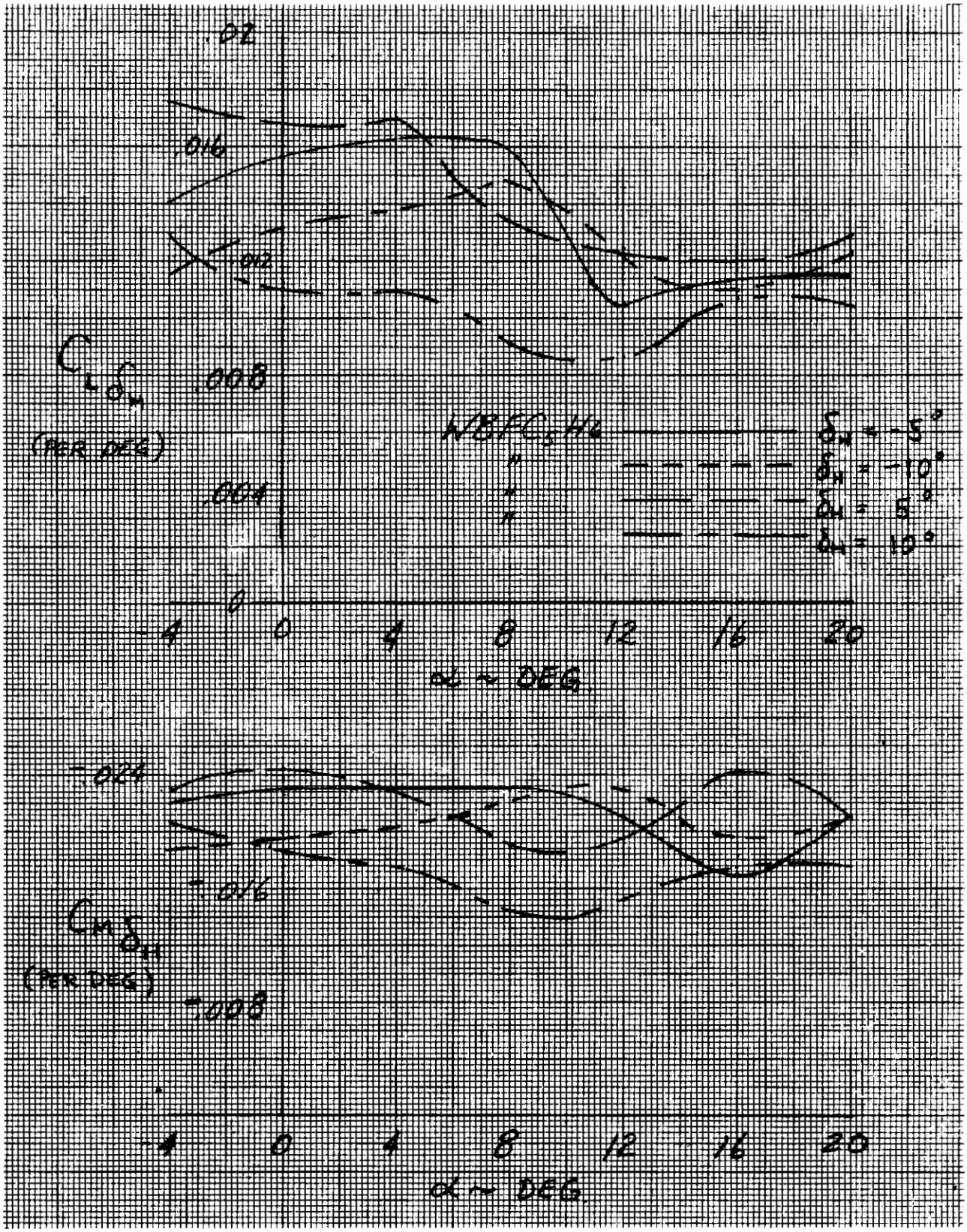

Figure 54. Aft V-tail effectiveness - H_6.

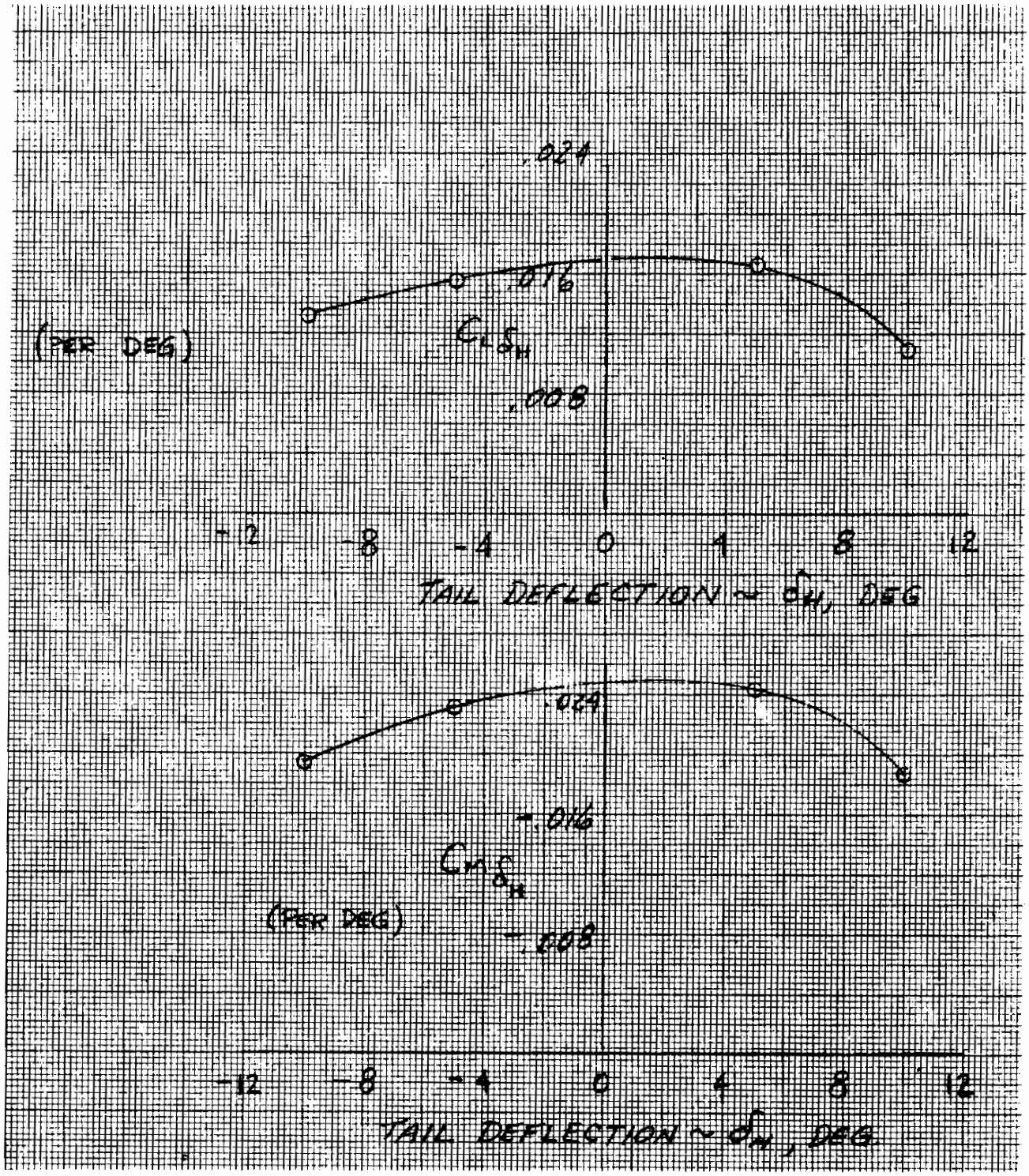

Figure 55. Aft tail effectiveness - H_6 α = 0.

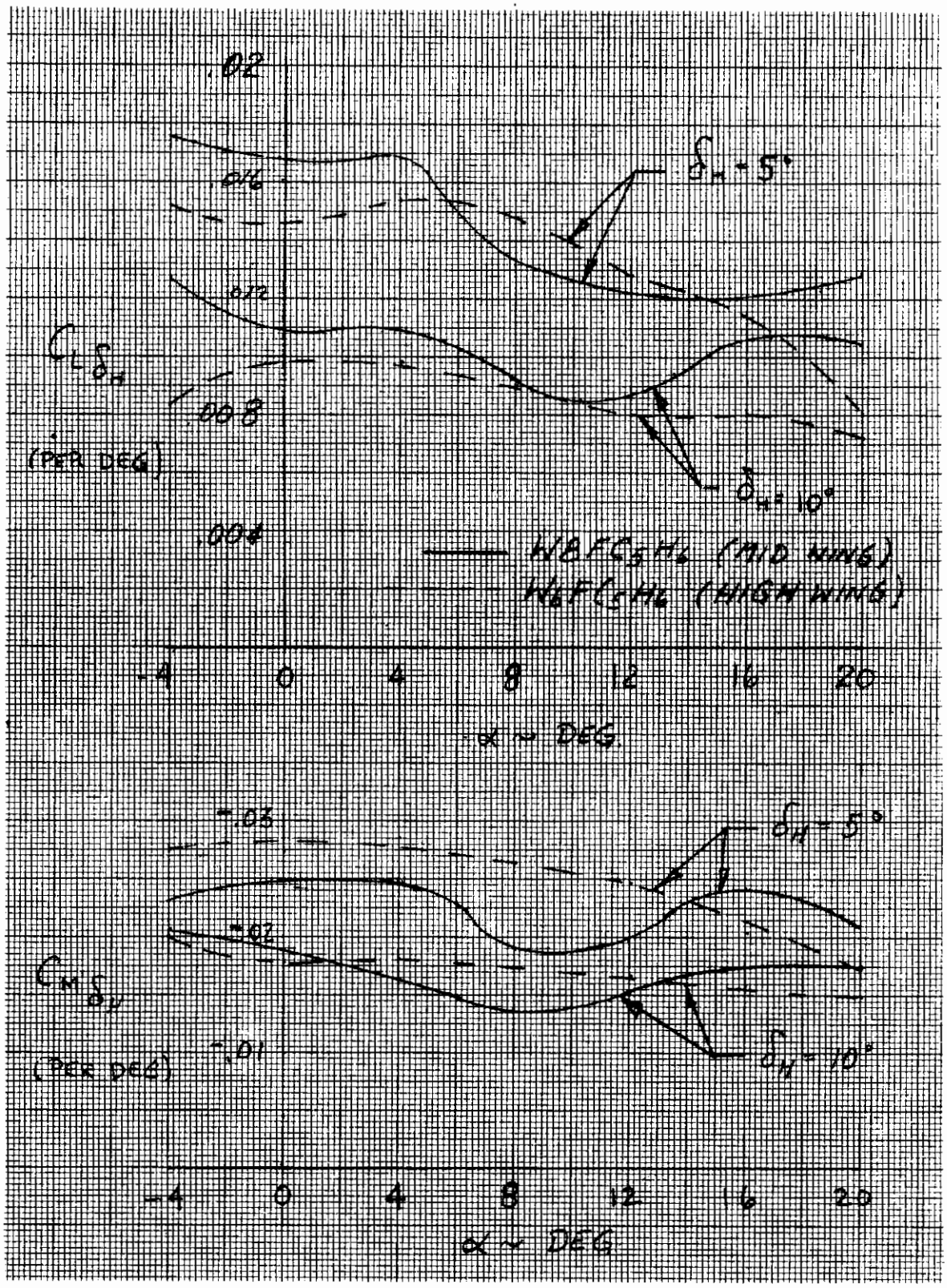

Figure 56. Effect of wing vertical position on rail effectiveness - H_6.

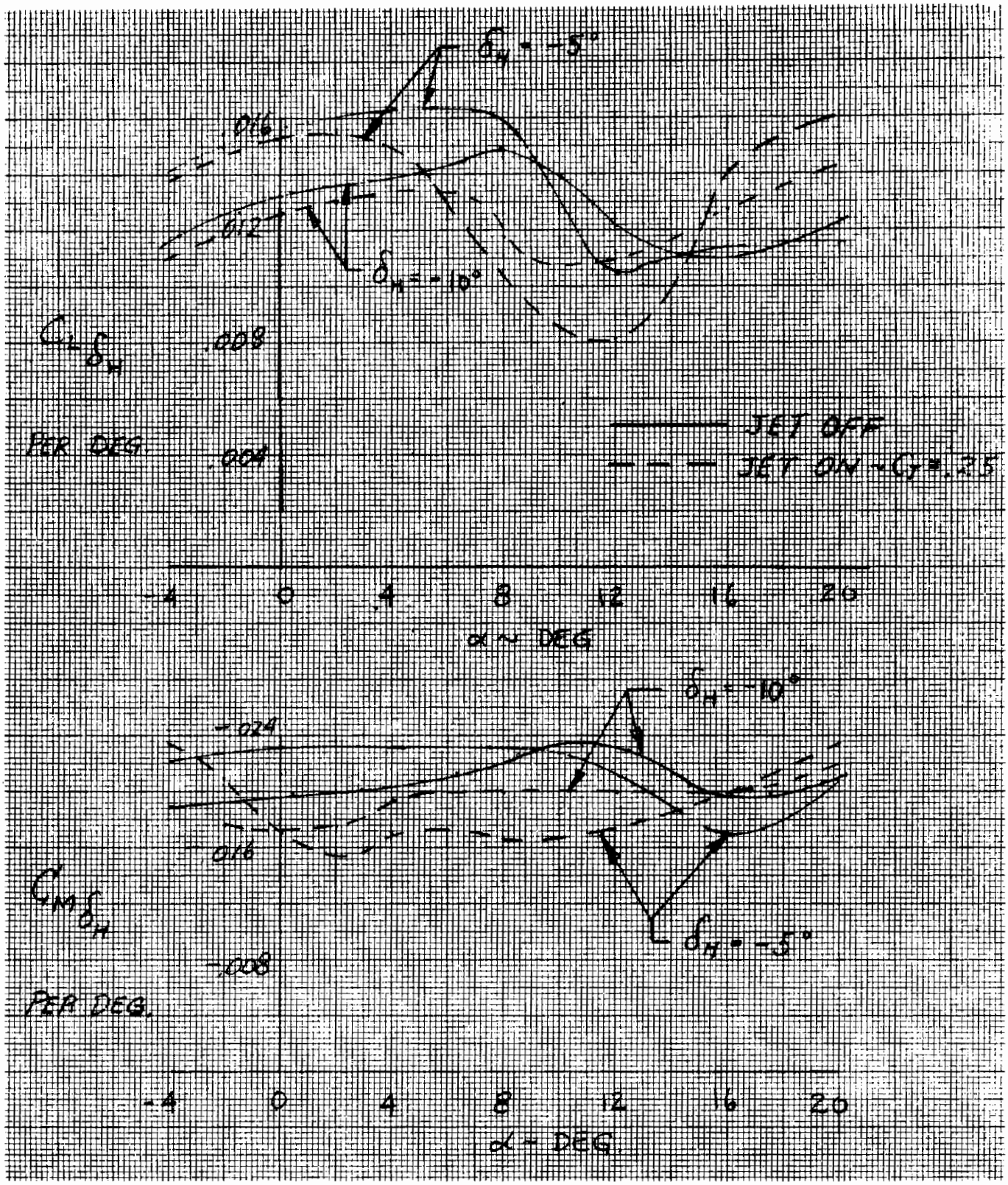

Figure 57. Aft tail effectiveness with jet flap on - C_T = 0.25.

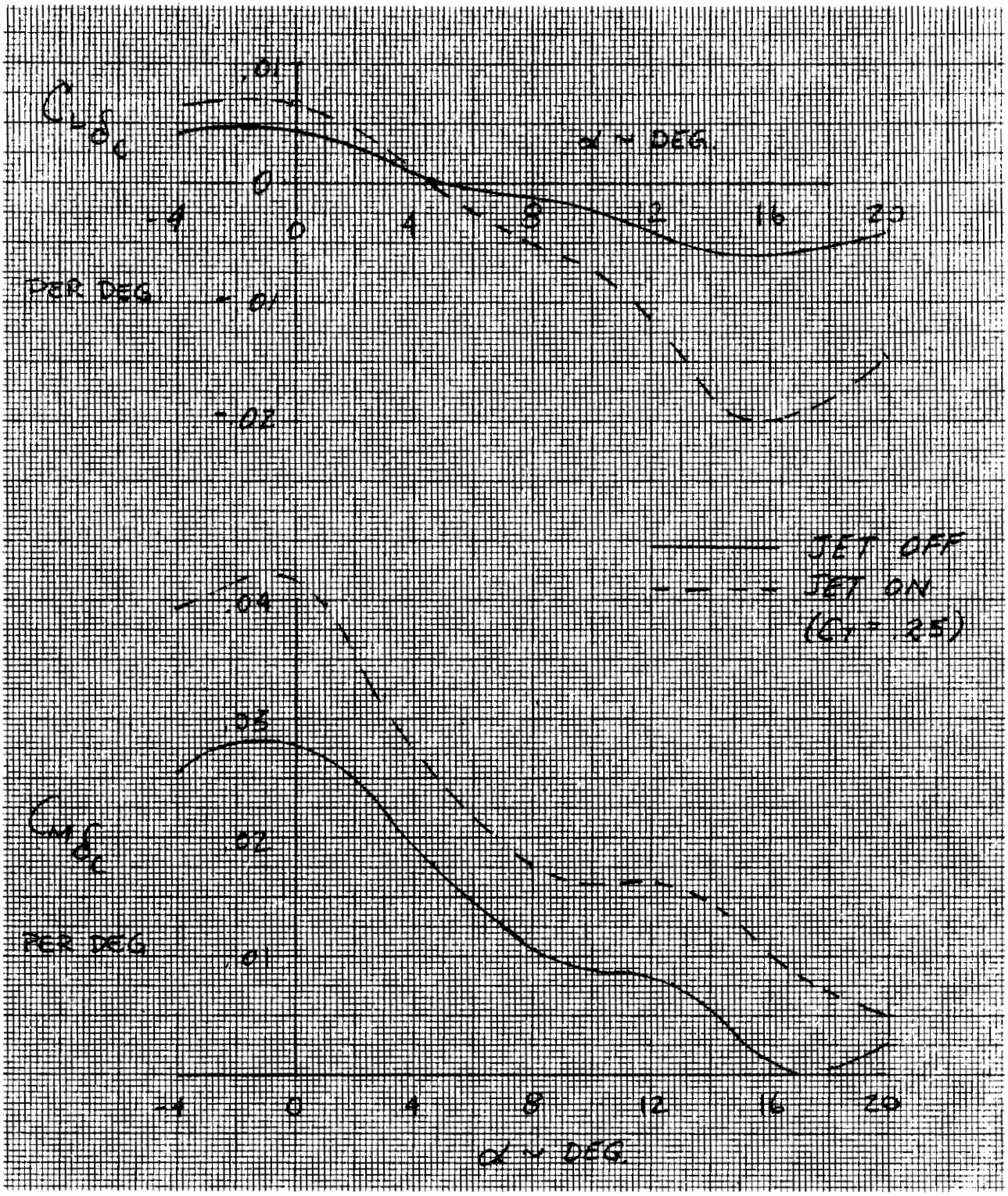

Figure 58. Canard effectiveness with jet flap on - C_T = 0.25.

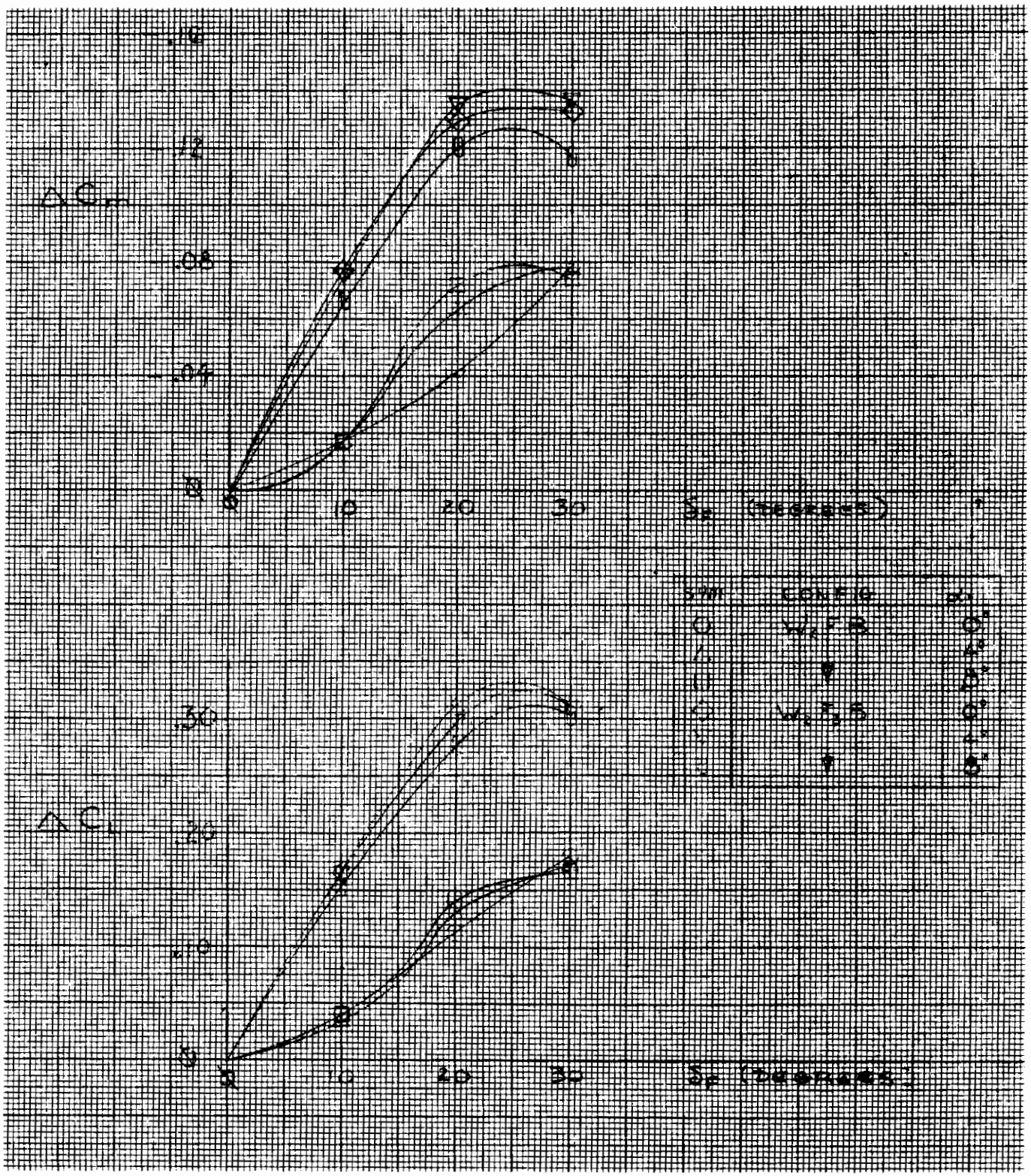

Figure 59. Effects of flap deflection thrust off.

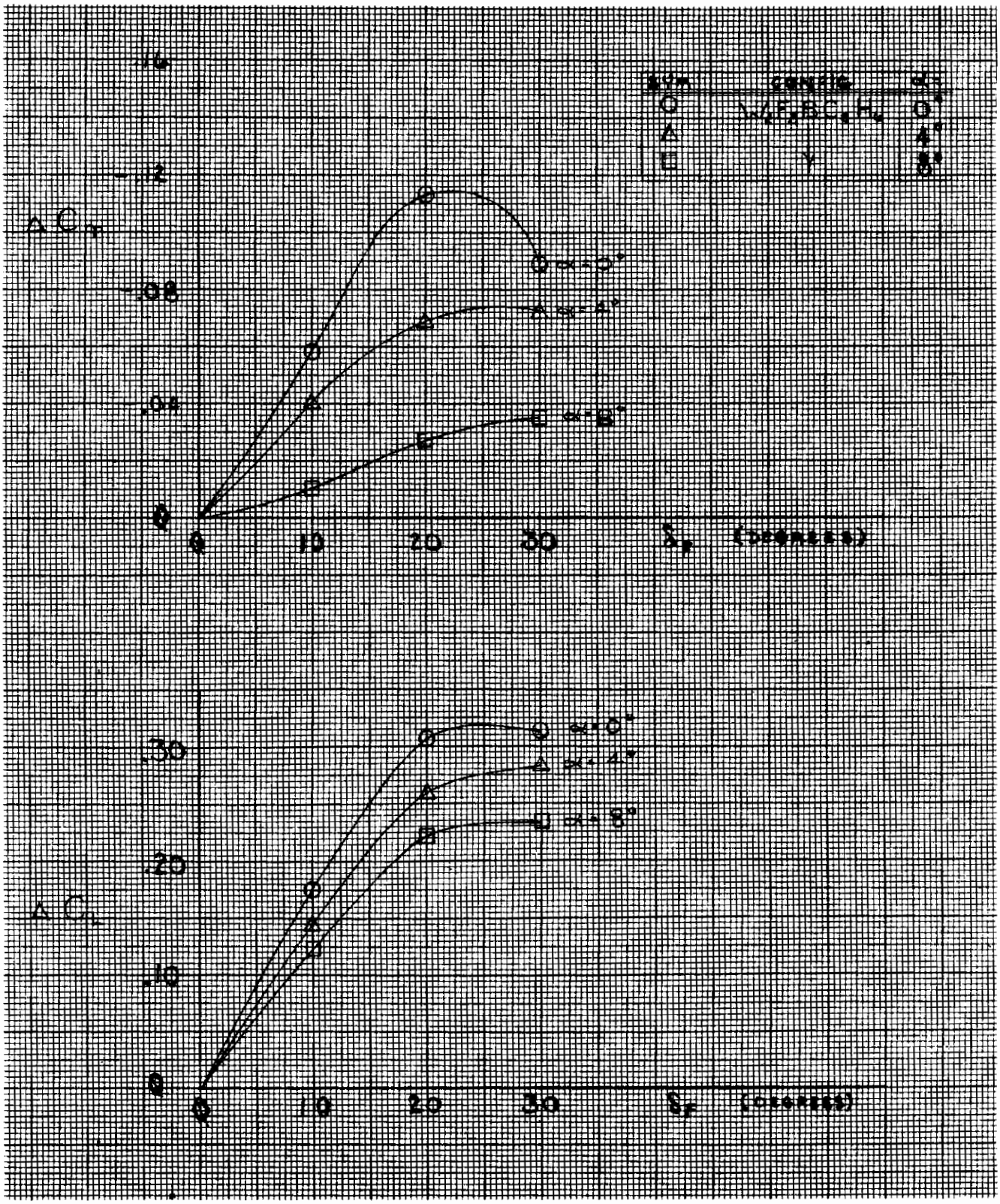

Figure 60. Effects of flap deflection thrust off.

Both the canards and aft tail surfaces were differentially deflected to determine side force, yawing, and rolling moment coefficients per degree of total differential deflection. Since there is positive diheral in the tail and negative in the canard, similar differential deflections produce side forces in the opposite directions. As presented in Figure 61, the tail is deflected in opposite direction of the canard to facilitate a side force comparison. The canard experiences a loss of effectiveness with increased angle of attack similar to longitudinal axis results. Deflecting both canard and tail simultaneously to produce combined side force shows that that stability increments are additive for individual deflections. This data are presented in plotted form in Reference 4.

LATERAL-DIRECTIONAL

The model static lateral-directional stability was determined by adding various component parts of the aircraft and deriving the incremental stability contribution of each component and the total configuration. Stability coefficients (per degree of sideslip) for the buildup of the base configuration are presented in Figure 62 versus angle of attack. Force data were measured versus angle of attack at zero and 3 degrees sideslip and versus sideslip angle at constant pitch angle for select configurations to determine the extent of the linear range. The results versus angle of attack are from the pitch variations at fixed sideslip angle and are in the stability axis system. The CG location for yawing moment data is resolved about the quarter chord point of the wing mean aerodynamic chord. As noted previously, the model CG location was a matter of convenience, and the longitudinal stability data and airplane configuration CG location indicate a more forward CG (to the wing leading edge, in most cases) which would increase the directional stability parameter by the expression

$$\Delta C_{n_\beta} = \Delta CG(MAC/b_w) \; C_{y_\beta}$$

where ΔCG is expressed in percent MAC. This correction is significant and must be accounted for when applying these data to air vehicle design.

Model buildup data are shown for the several airplane configurations tested in Figures 63 and 64. In the base configuration (WBC_5H_6) of Figure 65, the inputs of the canard and the total configuration versus angle of attack are of note. Canard input is destabilizing at low angles of attack, as expected for a forward surface with dihedral, but becomes stabilizing above 12 degrees to the extent of causing the WBC_5 configuration to be stable above 18 degrees. This effect is compared with other wing-body-canard relationships in Figure 66, and is important to the extent that is results in a full configuration directional stability (C_{n_β}) variation

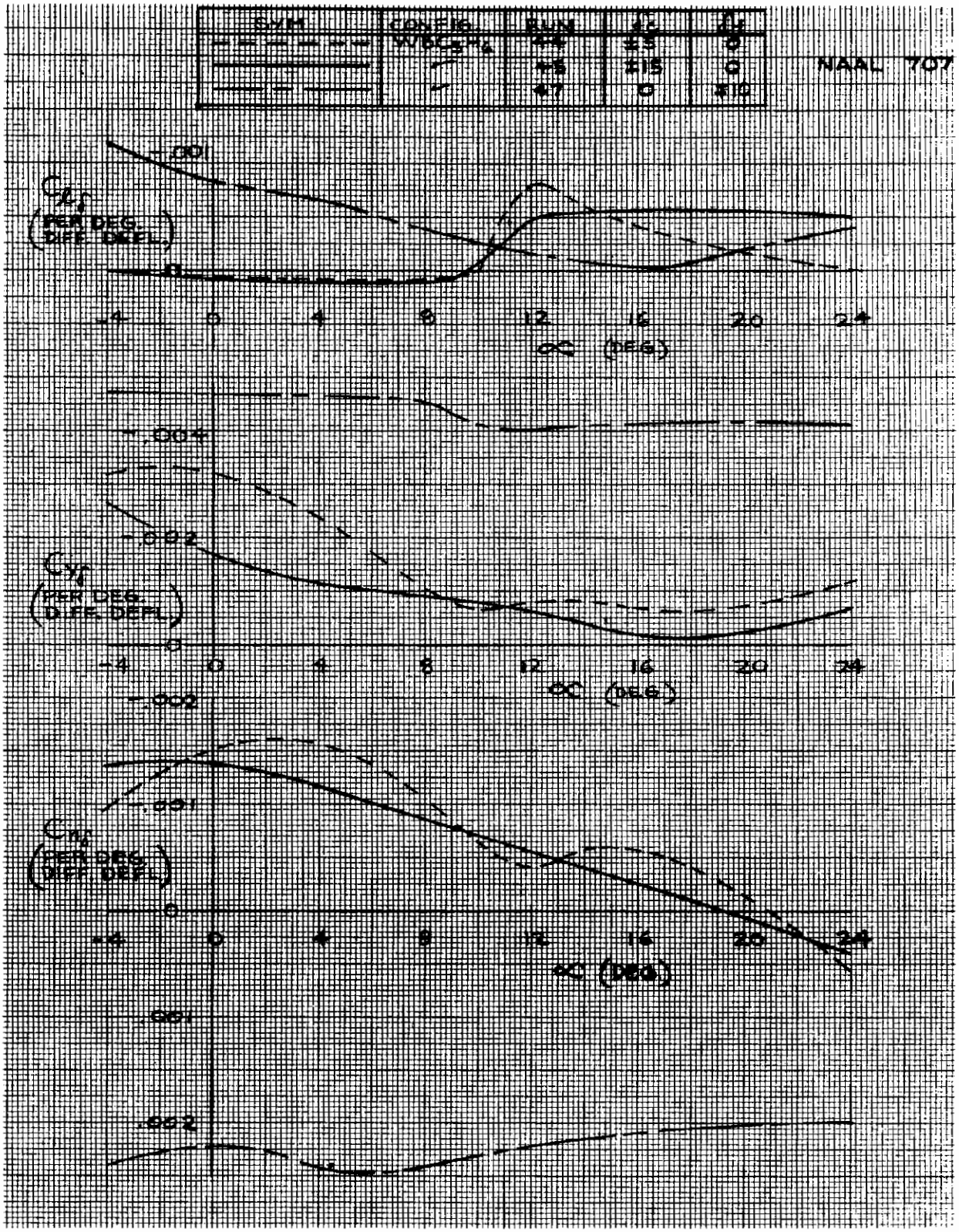

Figure 61. Differential deflection effectiveness.

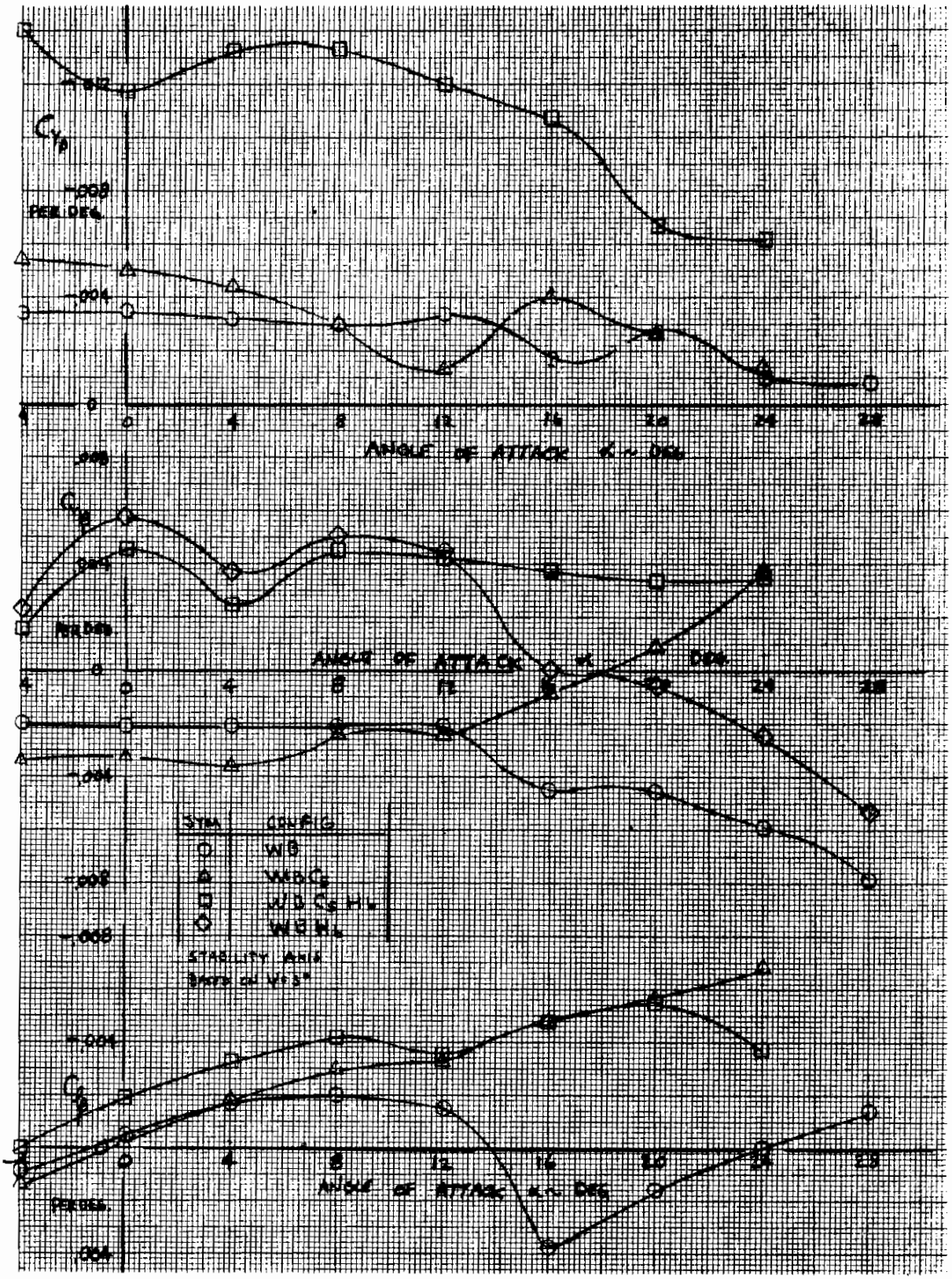

Figure 62. Effect of model buildup.

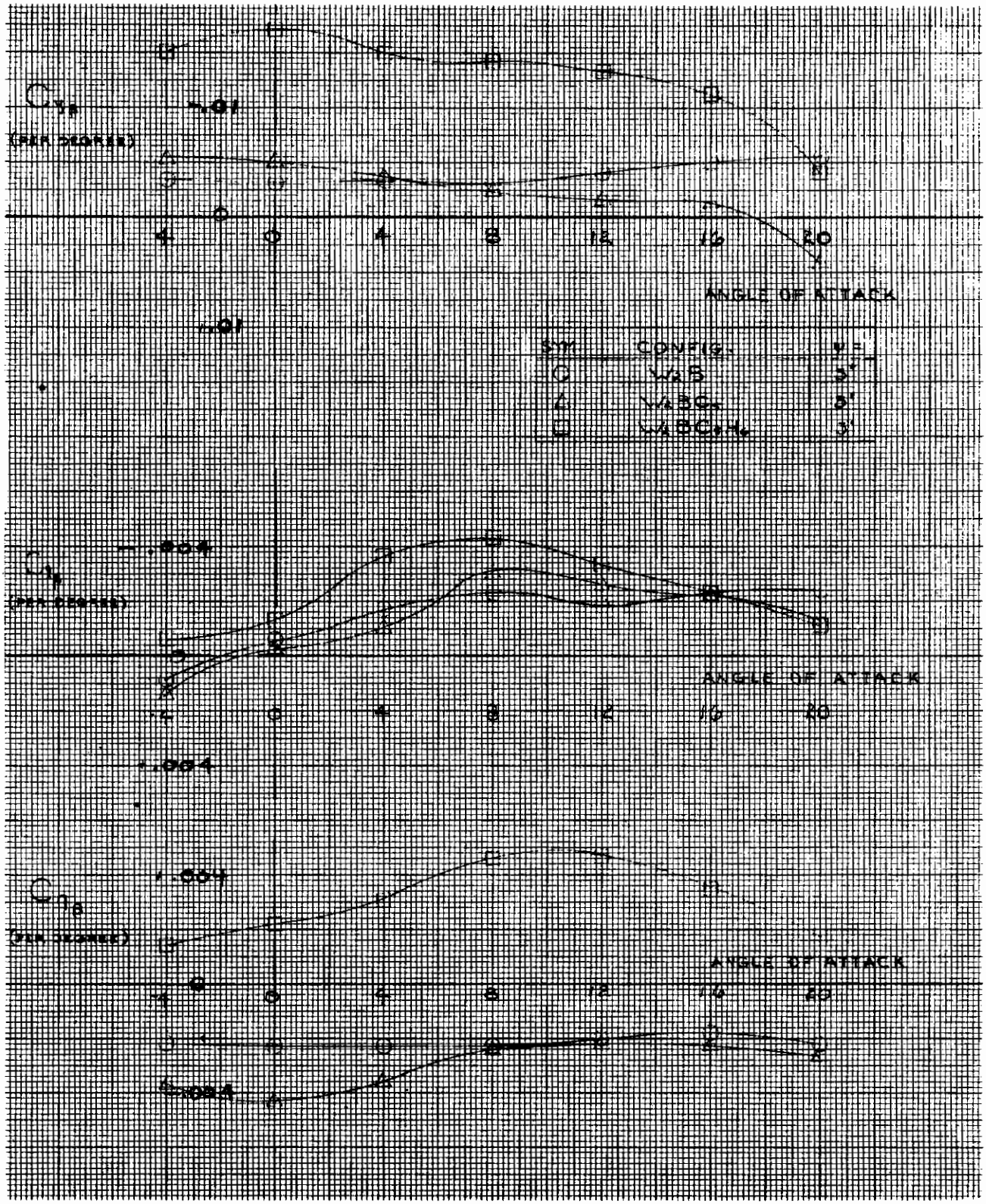

Figure 63. Stability Derivatives W_2B buildup.

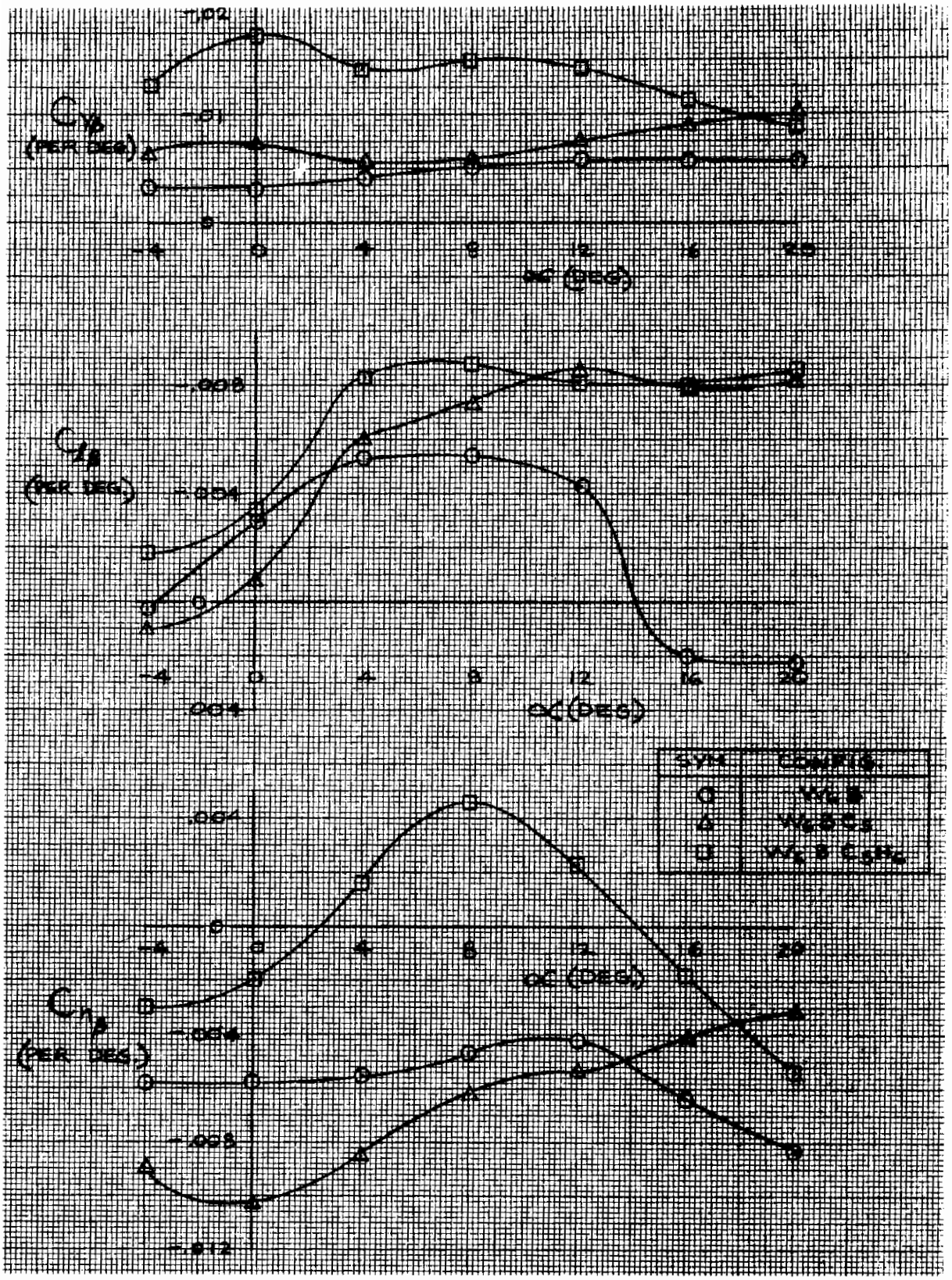

Figure 64. Stability derivative buildup, W_6.

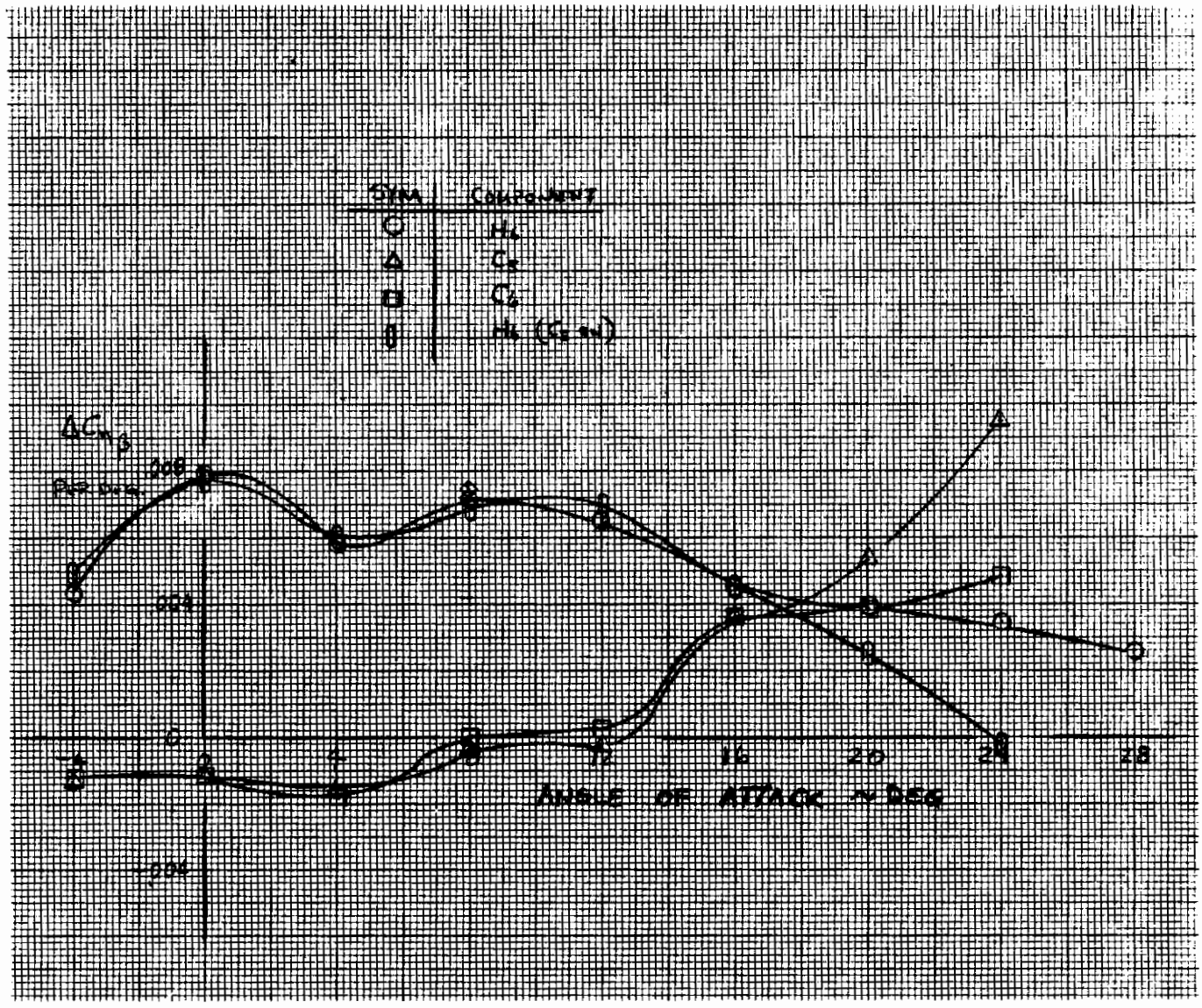

Figure 65. Directional stability inputs.

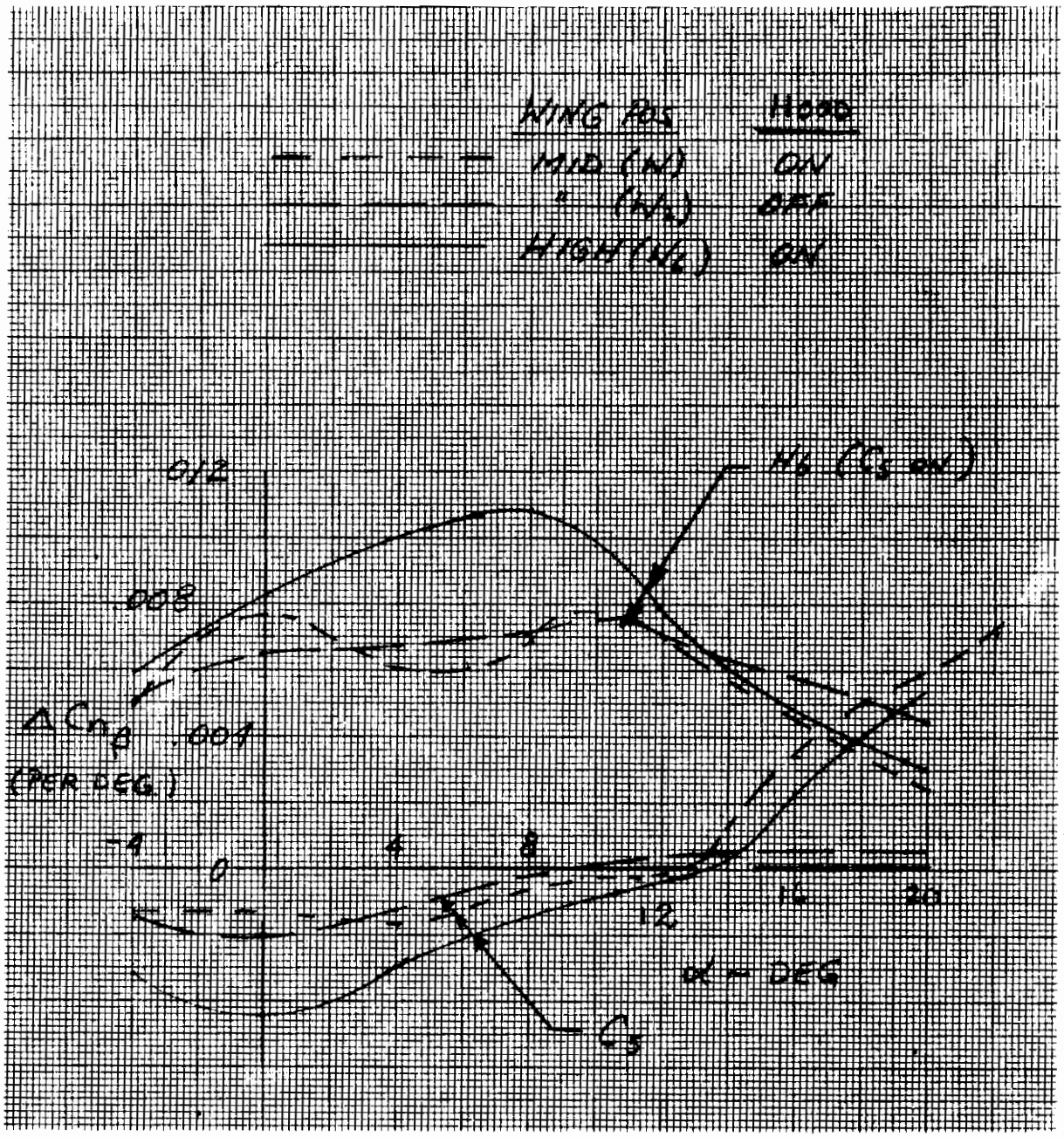

Figure 66. Effect of wing position and hood on stability input.

with pitch that remains stable through 28 degrees angle of attack. The reason for this effect being assigned to the WBC_5 relationship is the variation of the aft tail which has the characteristic variation with angle of attack, i.e., becoming unstable above 16 degrees. Variations of dihedral effect indicate a stable configuration at all angles of attack for the complete configuration. Also of interest is loss of stabilizing yawing moment at high angles of attack when the wing hood is removed, reaffirming the canard's strong influence on the total configuration stability. A comparison of two canard sizes on the input to the WBC directional stability is shown in Figure 67. Since the canard dihedral is 20 degrees, the component projected side area is increased by only one-third of the true area. Thus, the 33-percent larger true area of C_5 only amounts to 11 percent more projected side area and thus results in only small directional stability differences between the two.

Moving the canard rearward to the close-coupled position (C_7) and taking out the dihedral does change the directional stability trend. Figure 68 shows that yawing moment (C_{n_β}) for the wing-body-canard configuration does not contribute the large increasing stabilizing yawing moment at higher angles of attack that is characteristic of the forward canards. Thus, at high angles of attack ($\alpha \geq 20$ degrees), the total WBC_7H_6 configuration becomes directionally unstable.

FLOW SURVEY

The flow inclination and velocity ratio were obtain by separately running static pressure, total pressure, and goniometer probes over identical series of runs. The probe positions are shown in Figure 6. Figures 69 through 76 were obtained by cross-plotting variations of induced angle of attack and velocity ratio versus angles of attack at constant water plane. The yaw results are not developed here because they only add an indication of the velocity of the flow which is also represented by q/q_o but are shown in the plotted data report (Reference 4).

The rake location comparisons show how the fuselage and canard affect the flow approaching the wing. On the upper surface of the wing, downwash (ε) generally increases from the inboard stations to the outboard stations, except for some small negative increases at the higher angles of attack. Downwash increases from forward to aft positions at the outboard locations as expected, but the opposite occurs at the inboard locations. This reversal is most likely the result of interference and separation effects of the body (Figures 69 through 71). The body effects also show up on the lower surface (WP = -1.5) where less peaking and drop off occurs in the induced angle of attack and velocity ratios at inboard stations over their comparable outboard stations. This outboard-inboard comparison is also visible on Figure 75 and 76 on which configuration effects are compared.

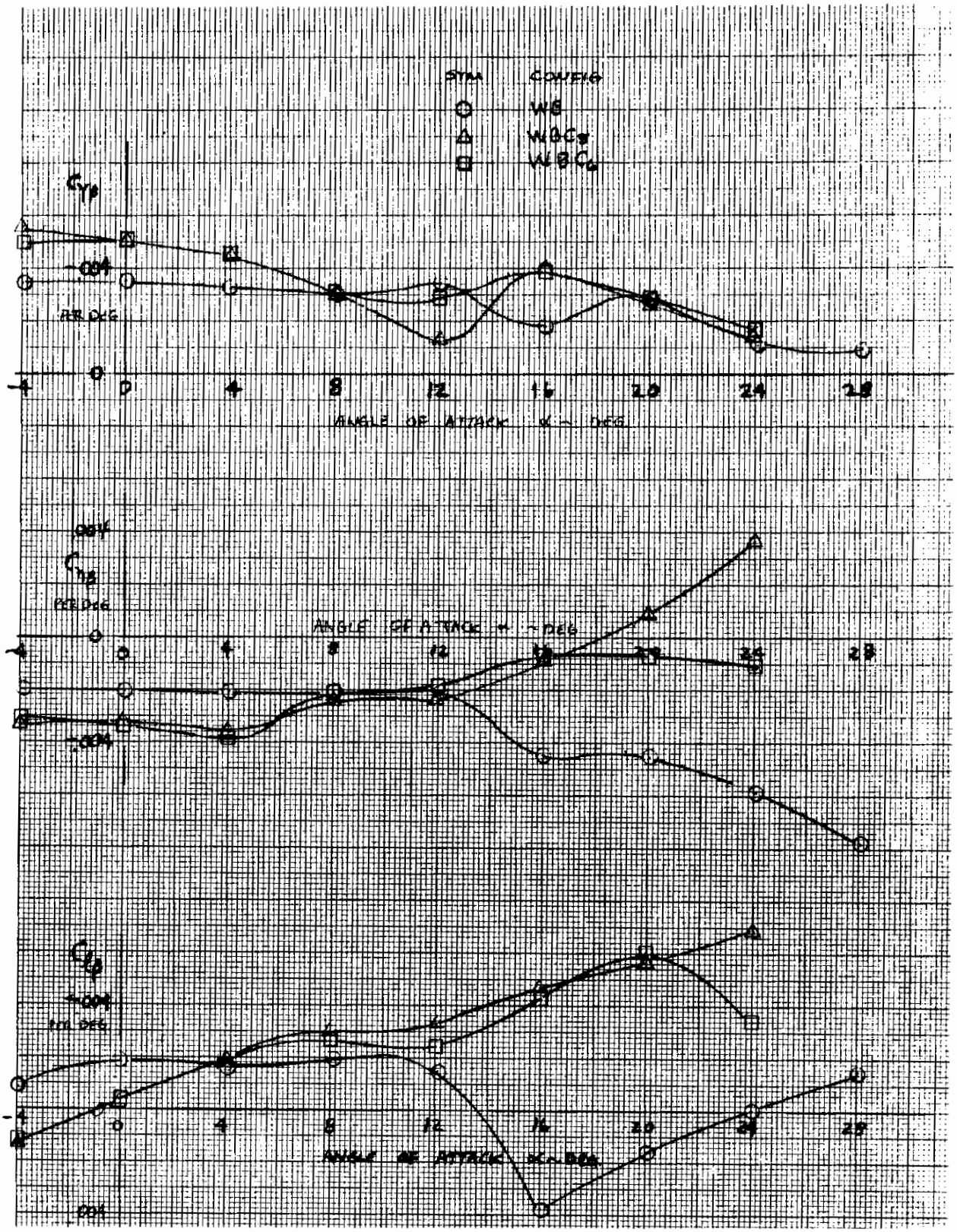

Figure 67. Effect of canard size.

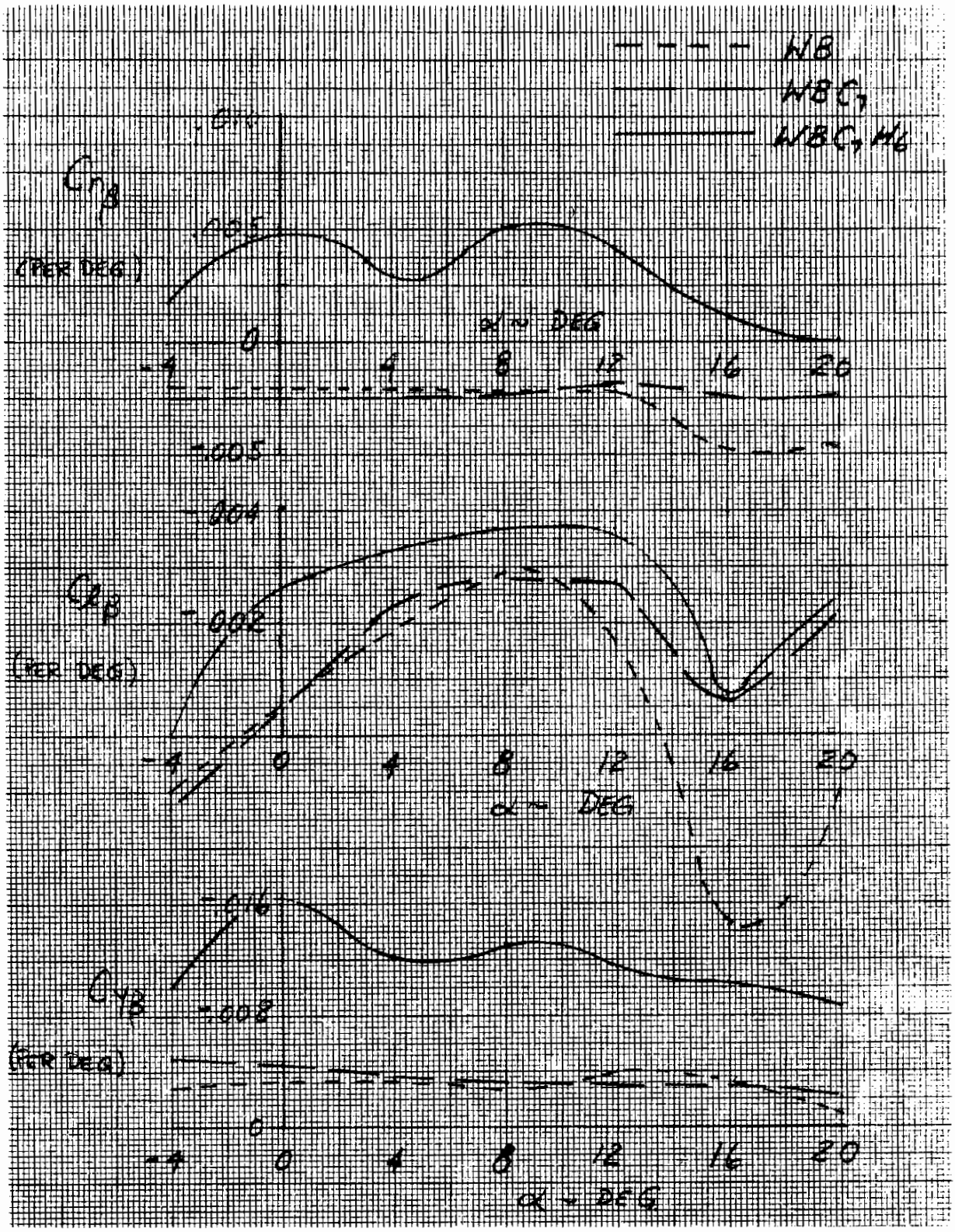

Figure 68. Canard lateral-directional buildup - C_7.

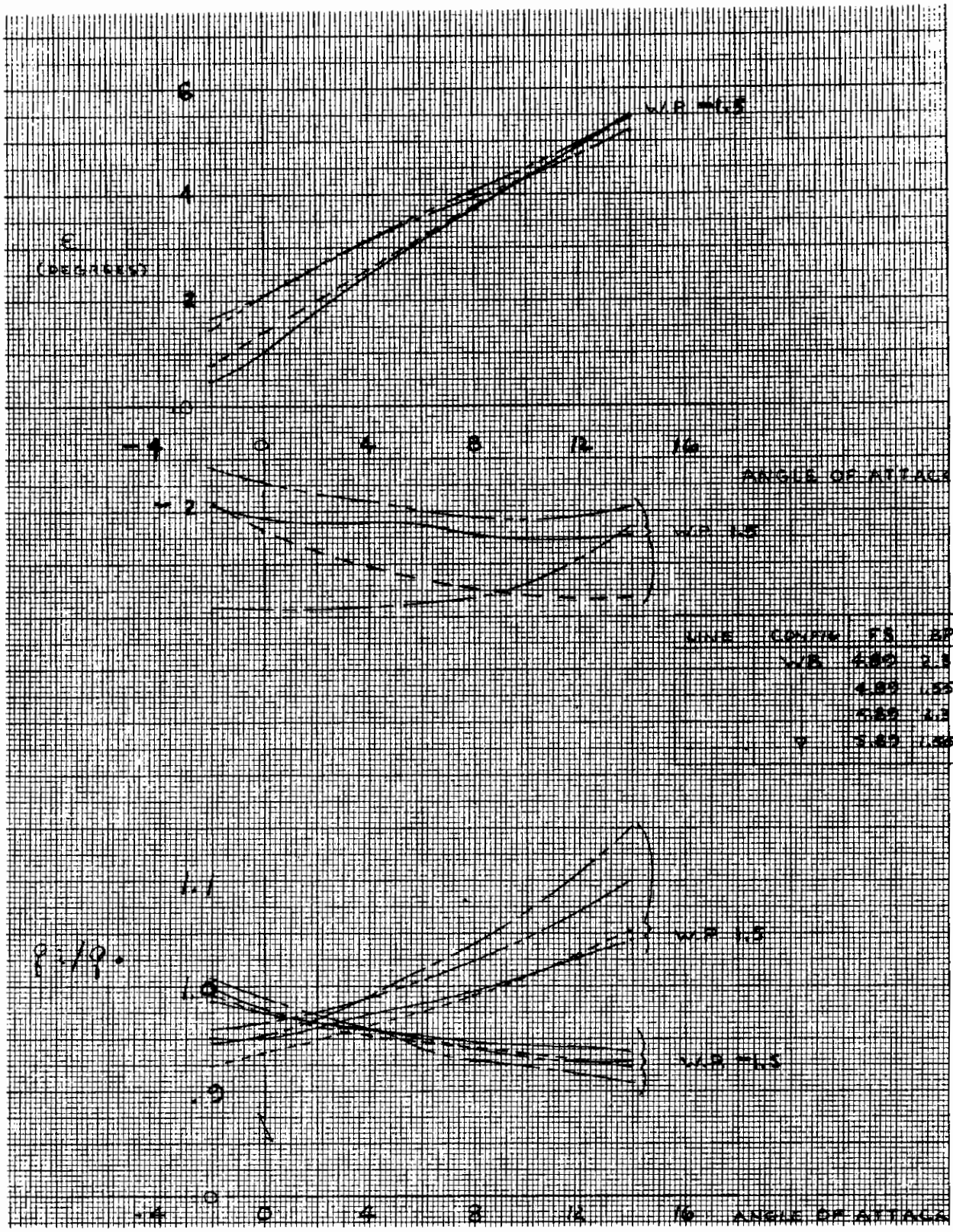

Figure 69. q ratio and flow inclination - effect of rake location.

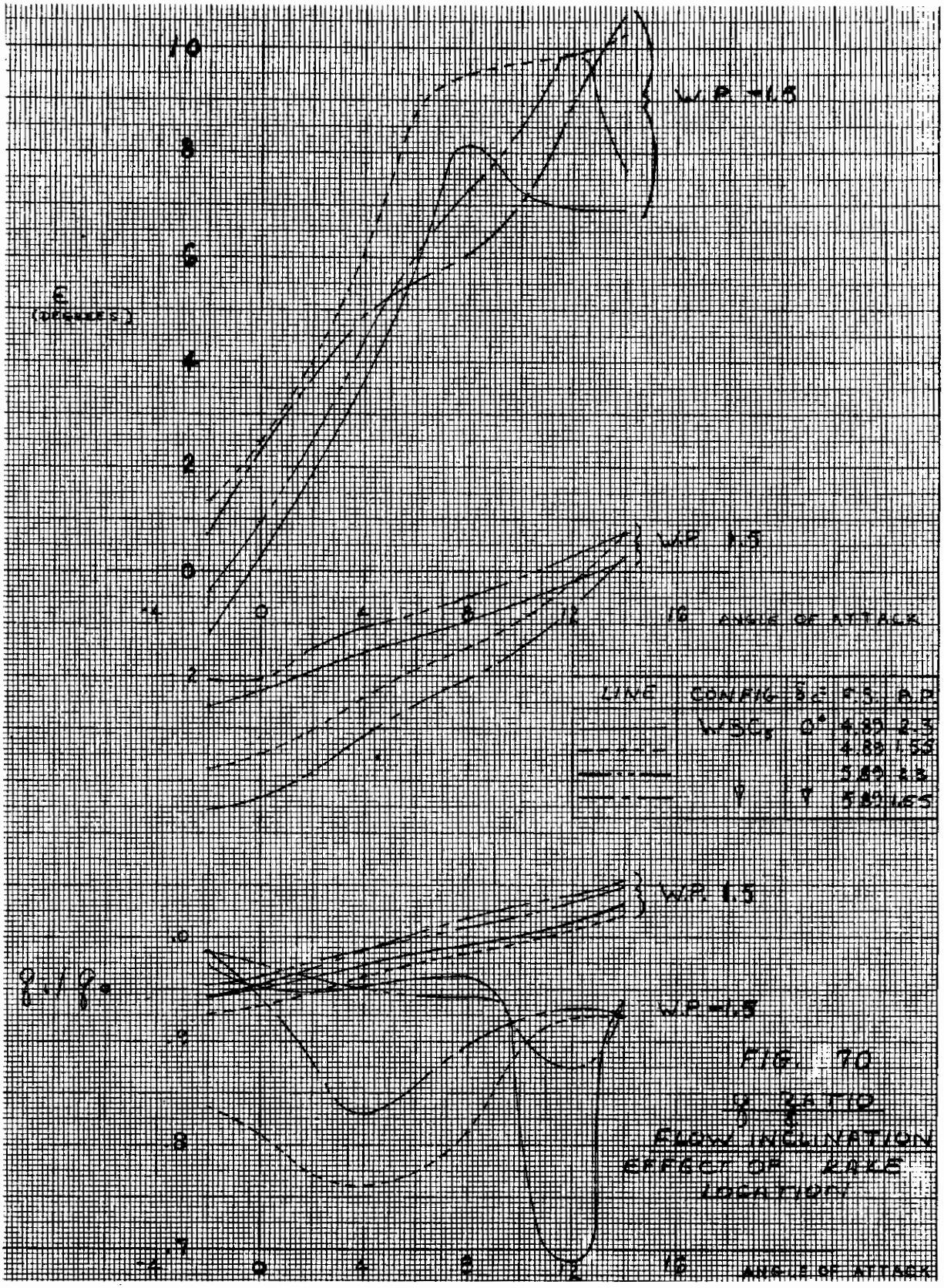

Figure 70. q ratio and flow inclination - effect of rake location.

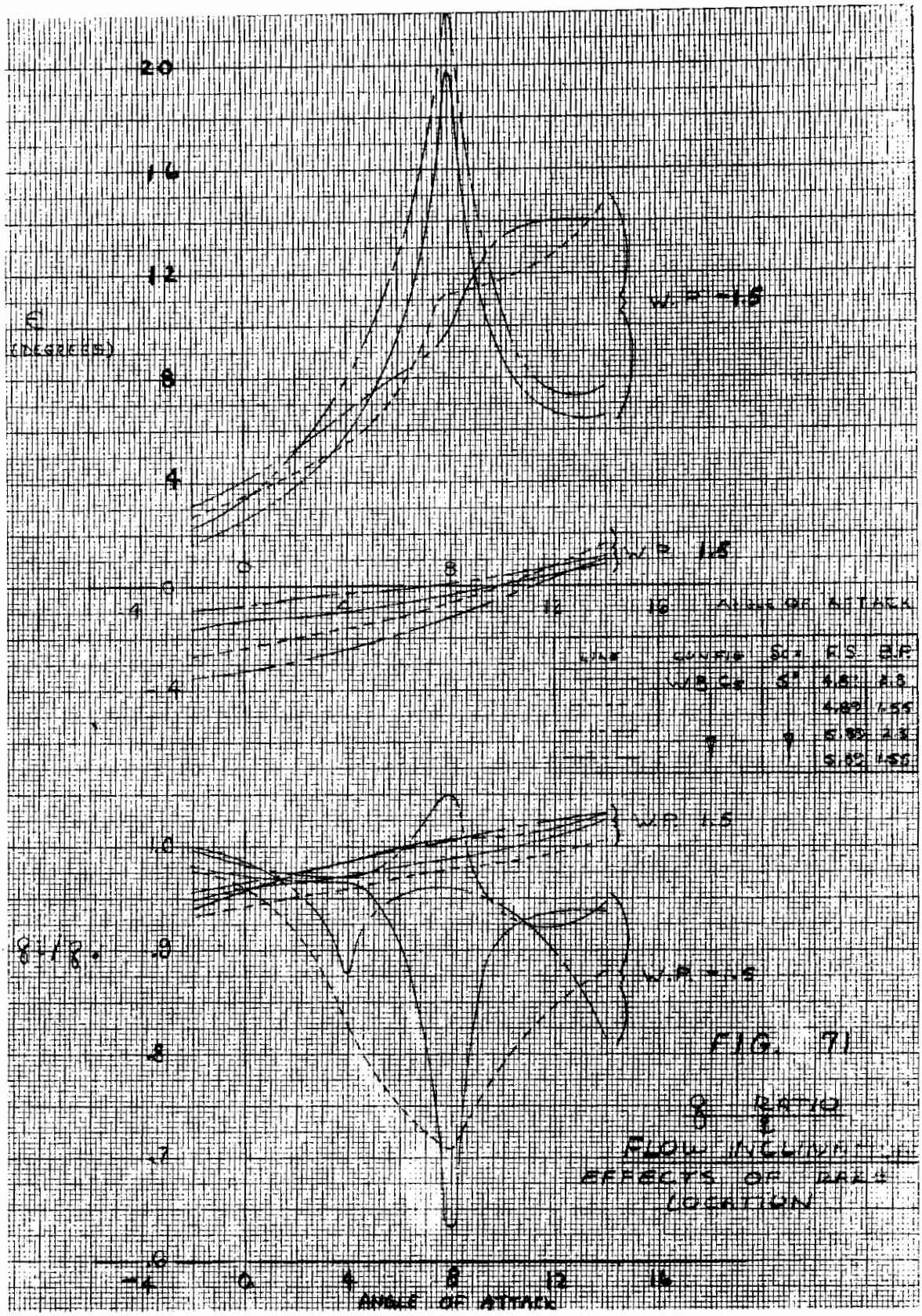

Figure 71. q ratio and flow inclination - effects of rake location.

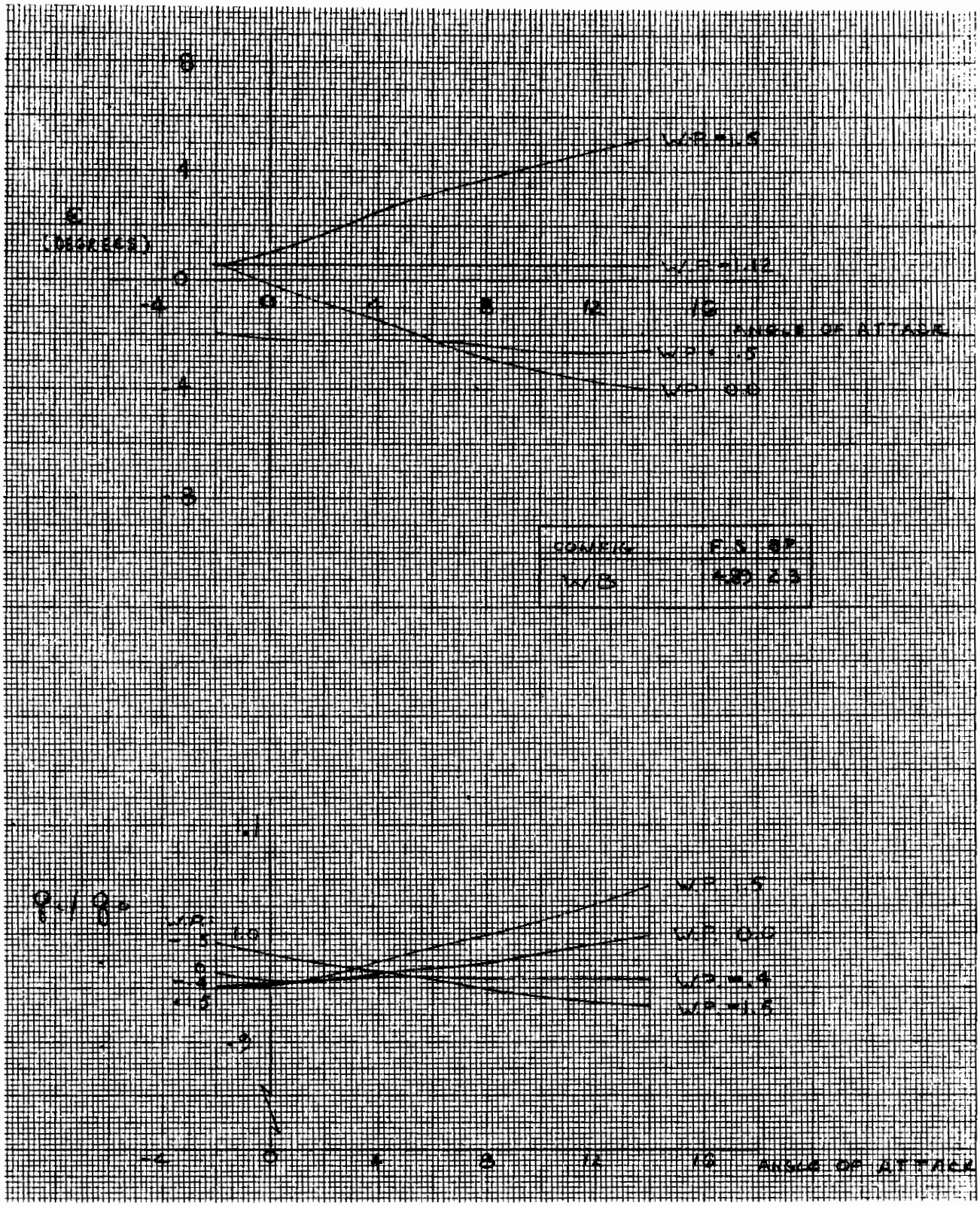

Figure 72. q ratio and flow inclination - effect of water plane location.

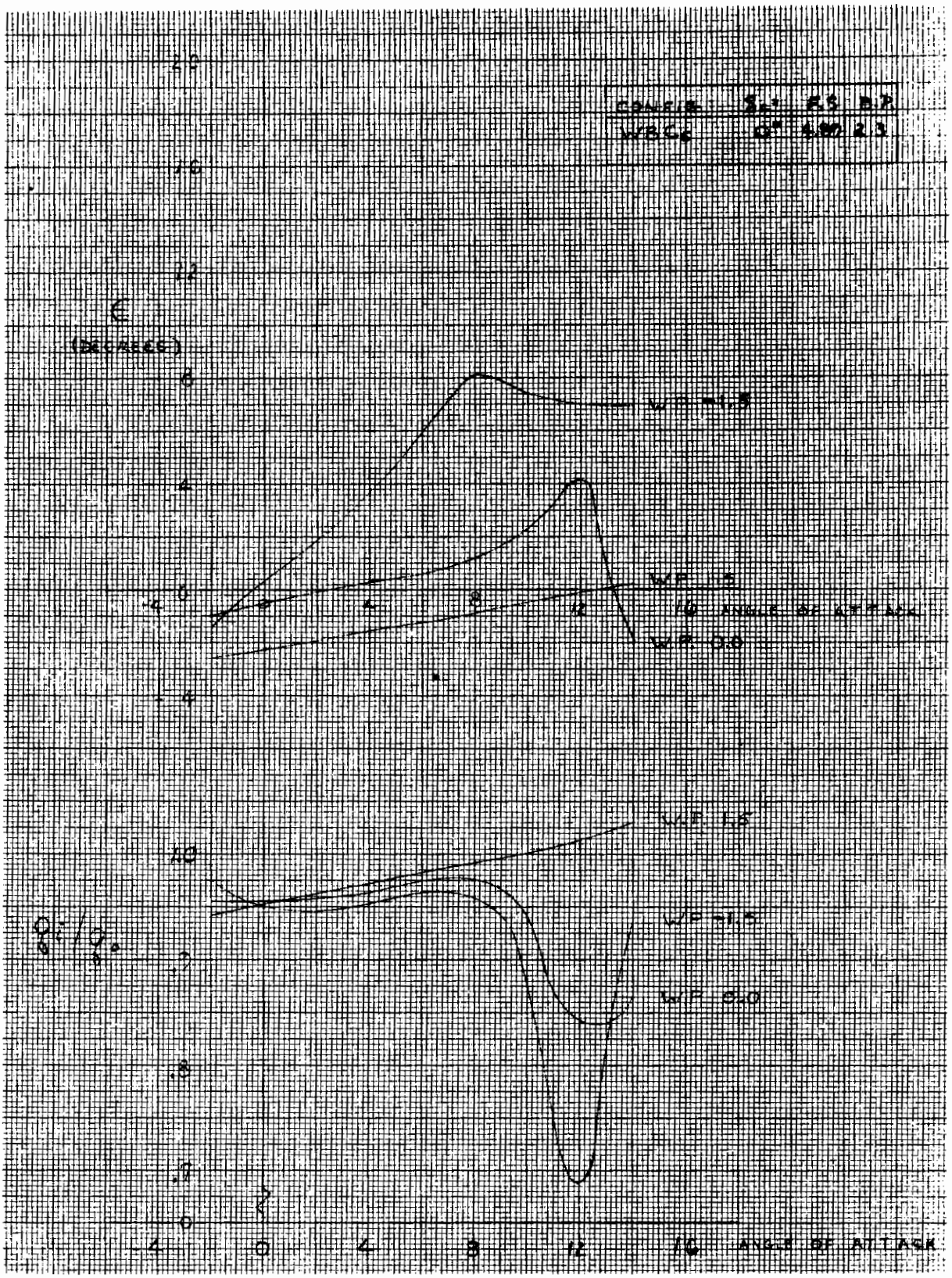

Figure 73. q ratio and flow inclination - effect of water plane location.

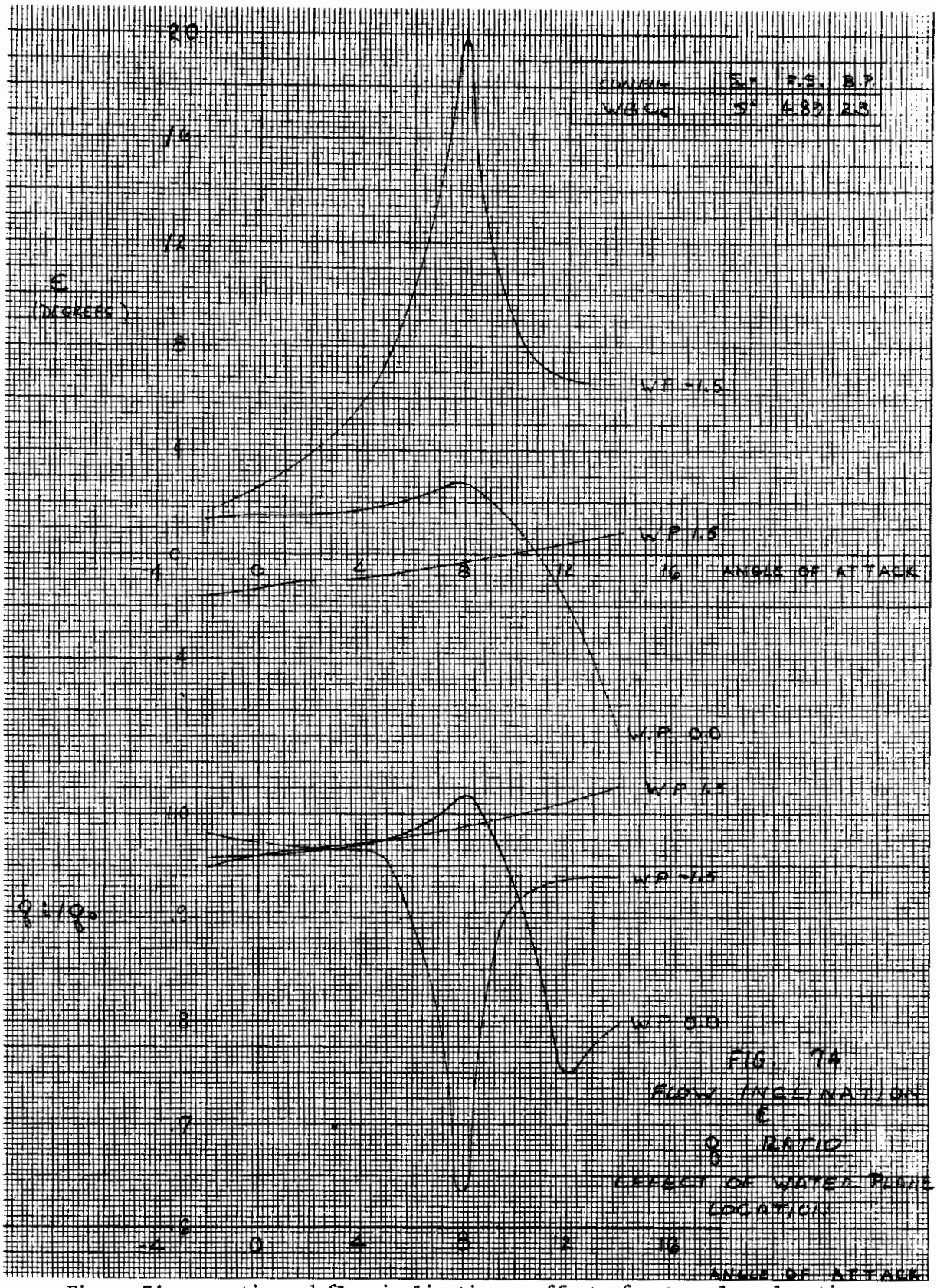

Figure 74. q ratio and flow inclination - effect of water plane location.

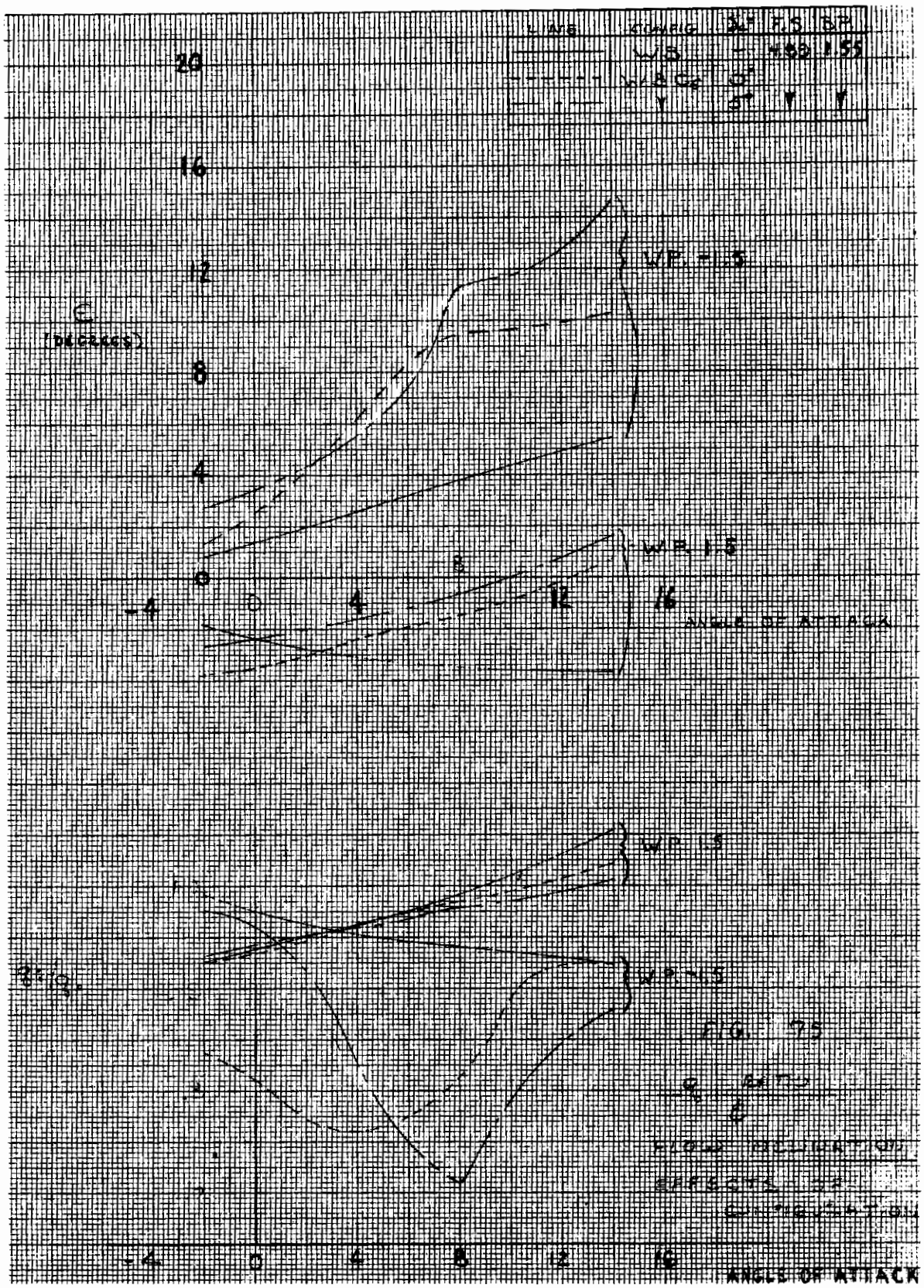

Figure 75. q ratio and flow inclination - effects of configuration.

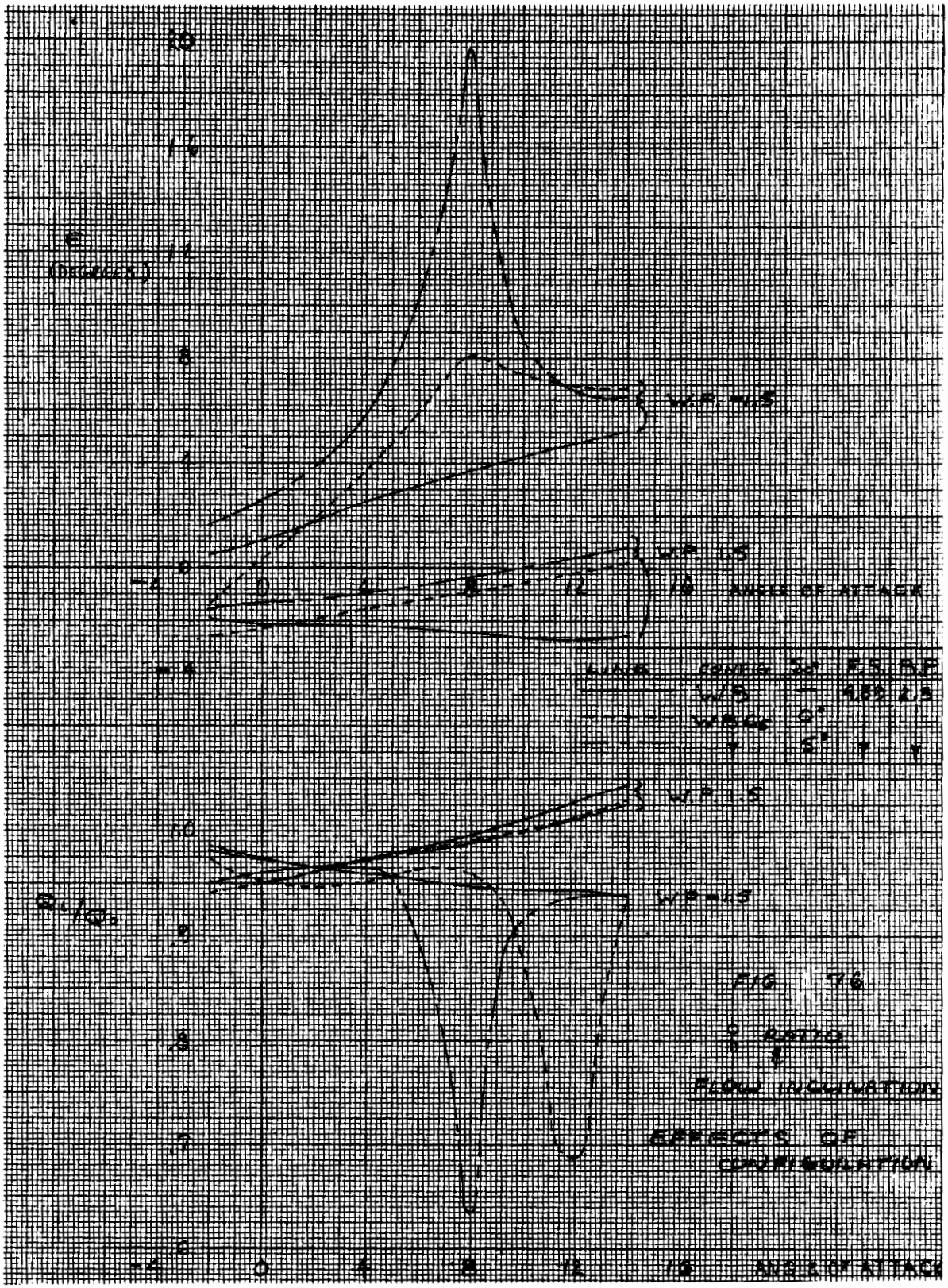

Figure 76. q ratio and flow inclination - effects of configuration.

The wing-body configuration shows an almost linear variation of ε and q_i/q_o with angle of attack (Figure 69). The addition of the canard and its subsequent deflection sharply increases $d\varepsilon/d\alpha$, for $\alpha < 8$ degrees, and the nonlinearity of the curves of ε and q_i/q_o versus angle of attack. At angles of attack of about 8 degrees, the separating vortices from the canard begin affecting the flow field beneath the wing plane causing abrupt drops or peaking in the induced angle of attack. The height of the peak rises sharply with the addition of the canard and to an even greater height when it is deflected 5 degrees. Vortex separation from the canard shows up on the velocity ratio as low as 4 degrees, and at 5 degrees canard deflection showing up as a sharp trough in the q_i/q_o curves (Figure 71). The presence of a lifting surface, such as the canard, produces a downwash proportional to the surface lift which, for the low-canard location, is expected to pass below the wing as indicated. A significant result from this test is that the areas above the wing do not greatly reflect the presence of the canard downwash or loss in dynamic pressure.

The upper surface of the wing shows smooth and almost linear variation of ε and q ratio with angle of attack. Downwash increases with the addition of the canard to the wing-body, but canard deflection does not change $d\varepsilon/d\alpha$ significantly over the canard-on value. The q ratio does not show any signs of vortex separation from the canard, indicating that all the wake from the canard is being trapped under the wing. It would be advantageous, therefore, to locate engine inlets above the wing if a near wing location is desired.

Another method of presenting this information is by a configuration buildup at discrete angles of attack. These presentations are found in the plotted data report (Reference 4) and are typical in their variations. Of particular interest here is the velocity ratio and its strong consistency on the upper surface of the wing with configuration buildup, supporting the analysis that all the canard wake passes under the wing not over.

SECTION V

CONCLUSIONS

The following conclusions are based on the results and analysis of the NAAL 707 test:

1. The longitudinal characteristics exhibit a continuing lift increase to high angles of attack and a somewhat nonlinear pitching moment variation with the large canard.

2. Correlation of aero prediction methods with test results indicate good agreement.

3. Due to wing flow field influences, canard effectiveness in the low forward position is increased over the isolated canard at low angle of attack, but is decreased at high angles of attack due to premature canard stall.

4. Altering low position canard geometry and canard to wing location produced expected changes in effectiveness level, but did not materially alter the unfavorable angle-of-attack variation. One canard position that provided a flat effectiveness with angle of attack was the closely coupled high canard to wing arrangement. However, this was accompanied by a reduction in effectiveness below four degrees alpha.

5. Flap effectiveness increases in direct relationship to surface area. The larger span (43-percent exposed) indicated stall above 20 degrees deflection. Adding the aft tails increased the angle-of-attack variations due to increased downwash.

6. Lateral directional characteristics are stable through 28 degrees angle of attack, primarily due to the large stabilizing input of the low forward canard above 12 degrees. This effect is slightly dimished by decreasing canard volume and the high wing location. The removal of the wing hood (W_2) greatly reduces this favorable canard input, but indicates that a strake in that area may be helpful if future configuration does not reflect this geometry.

7. Flow surveys indicate the wake of the canard passes under the wing through the maximum angle of attack of 15 degrees tested. This wake produces high downwash and velocity gradients. In contrast, the flow above the wing plane indicates moderate flow angles and is a potential inlet location.

8. The effects of exiting secondary air via the trailing edge flap arrangement produce an increase in lift, a negative moment input, and a reduction in drag proportional to thrust levels.

9. Increasing jet flap from 19- to 43 percent exposed span produces an increase in lift and moment which is fair agreement with the expected results.

10. The jet flap test technique employed for this test, with a bellows arrangement in line with the axial force flexure of a balance, results in reasonable lift data; however, it requires large calibration corrections to the drag data. The magnitude of the chord correction directs special attention to the obtainment of an accurate calibration with the secondary air system operational. An alternate system of redundant bellows arrangements with their axis out of the chord direction is suggested for future test.

REFERENCES

1. Corson, B. W., Capone, F. J., and Putnam, L. E., "Lift Induced on a Swept Wing by a Two-Dimensional Partial Span Deflected Jet at Mach Numbers From 0.20 to 1.30," NASA TM X-2309, NASA Langley Research Center, 1971

2. Lachmann, G. V., Boundary Layer Flow and Control, Vol I, Pergamon Press, 1961

3. Cohen, M. H., "Tabulated Data From Tests of an 0.07075 Scale Jet Flap Fighter Model in NAAL (707)," TFD-73-1101, Rockwell International, 10 August 1973

4. Divan III, P. E., "Plotted Data From NAAL 707 - Jet Flap Development Model," TFD-73-1096, Rockwell International, 10 August 1973

5. Panageas, G., "An Experimental Investigation of the Aerodynamic Characteristics of a Jet Flap at Mach Numbers 0.7 and 0.9," NA-72-667, Rockwell International, 5 September 1972

6. Panageas, G., and Sharon, A., "An Experimental Investigation of the Aerodynamic Characteristics of a Jet Flap Development Model at Transonic Mach Numbers," NA-73-55, Rockwell International, 1 February 1973

7. Stone, G., "Test Plan/Procedures for Test of a 0.07075 Scale FTD Force Model in the Rockwell NAAL Low Speed Wind Tunnel," NA-73-407, Rockwell International, 21 May 1973

LIST OF SYMBOLS

GENERAL SYMBOLS

AR	Aspect ratio, b^2/s
b	Wing span, ft
c	Surface chord, ft
s	Surface area, sq ft
$\bar{c}$, MAC	Mean aerodynamic chord, ft
l	Tail arm ($0.25\bar{c}_w$ to $0.25\bar{c}_H$), ft
CG	Center of gravity
q, Q	Dynamic pressure, psf
AC	Aerodynamic center ($CG - \frac{dC_m}{dC_L}$)
$\frac{dC_m}{dC_L}$	Static longitudinal stability
C_{L_o}	Lift coefficient at zero angle of attack
C_{L_α}	Lift curve slope, $\frac{dC_L}{d\alpha}$, per deg
C_{m_o}	Pitching moment at zero lift coefficient
S	Leading edge suction, percent
C_{D_o}	Drag at zero lift coefficient
RN	Reynolds number, per ft
α	Angle of attack, deg
δ	Surface deflection, deg

Λ	Leading edge sweep angle, deg
θ, δ	Jet deflection angle
ϵ	Downwash angle, deg
β	Sideslip angle, deg
ψ	Yaw angle ($-\beta$), deg
Γ	Dihedral angle, deg
λ	Taper ratio
FS	Fuselage station, in.
WS	Wing station, in.
BP	Buttock plane, in.
WP	Water plane, in.

COEFFICIENTS

C_L	Lift coefficient, $\frac{\text{Lift}}{q\ S_w}$
C_D	Drag coefficient, $\frac{\text{Drag}}{q\ S_w}$
C_m	Pitching moment coefficient, $\frac{\text{Pitching moment}}{q\ S_w\ \bar{c}_w}$
C_Y	Side force coefficient, $\frac{\text{Side force}}{q\ S_w}$
C_n	Yawing moment coefficient, $\frac{\text{Yawing moment}}{q\ S_w\ b_w}$
C_ℓ	Rolling moment coefficient, $\frac{\text{Rolling moment}}{q\ S_w\ b_w}$

C_N	Normal force coefficient, $\frac{\text{Normal force}}{q\ S_w}$
C_c	Chord force coefficient, $\frac{\text{Chord force}}{q\ S_w}$

SUBSCRIPTS

A	Airplane
c/4	Quarter-chord of any local chord
$C_L = 0$	At zero lift
MAX	Maximum
LE	Leading edge
TE	Trailing edge
S	Stability axes
B	Body axes
TOT	Total
$0,\infty$	Free-stream condition
$\alpha = 0°$	At zero angle of attack
H	Horizontal tail
V	Vertical tail
F	Flap
c	Canard
T	Thrust
W	Wing

ADDITIONAL TERMS

P_{T_e}/P_∞ = Ratio of jet exit total pressure to free-stream

F_g = Gross trust

$$= A^* \; P_{T_e} \left\{ \frac{2\gamma^2}{\gamma-1} \left(\frac{2}{\gamma+1} \right)^{\frac{\gamma+1}{\gamma-1}} \left[1 - \left(\frac{P_o}{P_{T_e}} \right)^{\frac{\gamma-1}{\gamma}} \right] \right\} 1/$$

C_T = Gross thrust coefficient

$$= \frac{F_g}{q S_{REF}}$$

A^* = Discharge area: $K^* A_{EXIT}$

C_{L_Γ} = Jet induced lift

$$= C_{L_\Gamma} = \left[\Delta C_L - C_T \sin(\alpha + \delta) \right] \quad \begin{matrix} \delta_F = K \\ \alpha = K \end{matrix}$$

G = Gain factor

$$= \frac{C_T \sin \delta + C_{L_\Gamma}}{C_T \sin \delta}$$

C_{m_Γ} = Jet induced moment

$$C_{m_\Gamma} = = \left[\Delta C_m - C_T \left(\frac{d}{\bar{c}_w} \right) \right] \quad \begin{matrix} \delta_F = K \\ \alpha = K \end{matrix}$$

$\bar{V}_H$ = Horizontal surface volume = $\frac{S_H}{S_{REF}} \frac{\ell_t}{\bar{c}_w}$

$\bar{V}_V$ = Vertical surface volume = $\frac{S_V}{S_{REF}} \frac{\ell_c}{\bar{b}_w}$

S_H = Plan area (cos Γ)

S_V = Plan area (sin Γ)

$\Delta C_L = \left(C_{L_{C_T = x}} - C_{L_{C_T = 0}} \right)_{\substack{\delta = K \\ \delta_F = K}}$ Total lift increment

$\Delta C_m = \left(C_{m_{C_T = x}} - C_{m_{C_T = 0}} \right)_{\substack{\delta = K \\ \delta_F = K}}$ Total moment increment

$\Delta C_D = \left(C_{D_{C_T = x}} - C_{D_{C_T = 0}} \right)_{\substack{\delta_F = K \\ C_L = K}}$ Total drag increment

$\eta = \frac{\Delta C_{D_{NET}}}{-C_T} = \frac{\left(C_{D_{C_T = K}} - C_{D_{C_T = 0}} \right)_{C_L = K}}{-C_T}$ Thrust recovery

☆U.S.Government Printing Office: 1974 — 758-434/545